Titre: Title:	Continuous In-line De-agglomeration and Coating of Nanoparticles
Auteur: Author:	Hamed Nasri Lari
Date:	2020
Type:	Mémoire ou thèse / Dissertation or Thesis
Référence: Citation:	Nasri Lari, H. (2020). Continuous In-line De-agglomeration and Coating of Nanoparticles [Thèse de doctorat, Polytechnique Montréal]. PolyPublie. https://publications.polymtl.ca/5223/

Document en libre accès dans PolyPublie
Open Access document in PolyPublie

URL de PolyPublie: PolyPublie URL:	https://publications.polymtl.ca/5223/
Directeurs de recherche: Advisors:	Jamal Chaouki, & Jason Robert Tavares
Programme: Program:	Génie chimique

POLYTECHNIQUE MONTRÉAL

affiliée à l'Université de Montréal

Continuous In-line De-agglomeration and Coating of Nanoparticles

HAMED NASRI LARI

Département de génie chimique

Thèse pésentée en vue de l'obtention du diplôme de *Philosophiae Doctor*

Génie chimique

Février 2020

POLYTECHNIQUE MONTRÉAL

affiliée à l'Université de Montréal

Cette thèse intitulée :

Continuous In-line De-agglomeration and Coating of Nanoparticles

présentée par **Hamed NASRI LARI**

en vue de l'obtention du diplôme de *Philosophiae Doctor*

a été dûment acceptée par le jury d'examen constitué de :

Olivier HENRY, président
Jason Robert TAVARES, membre et directeur de recherche
Jamal CHAOUKI, membre et codirecteur de recherche
Ludvik MARTINU, membre
Sylvain COULOMBE, membre externe

DEDICATION

to my beloved family

ACKNOWLEDGEMENTS

RÉSUMÉ

Les nanoparticules (NPs) sont maintenant produites commercialement et utilisées à de multiples fins, dans des applications industrielles telles que les catalyseurs pour l'administration de médicaments anticancéreux jusqu'à des crème solaire dans les cosmétiques. Toutefois, leur production, leur stockage et leur traitement présentent encore un défi majeur : l'agglomération. Lorsque les NPs forment des agglomérats, ceux-ci perdent leurs propriétés de surface extraordinaires qu'ils avaient en tant que NP individuelles. Pour profiter de leurs "nanopropriétés", il est nécessaire de briser les agglomérats et de réduire leur énergie de surface élevée, ou de les "passiver", avant utilisation. La capacité de produire des quantités en vrac de NPs très dispersées est une limitation importante de la nanotechnologie.

Traditionnellement, la désagglomération et la stabilisation des NPs se font en phase liquide, car de nombreuses réactions et synthèses se produisent dans cette phase. L'ultrasonication combinée à des surfactants est une technique typique pour disperser et stabiliser les NPs en phase liquide. Bien que les techniques à base de solvants soient généralement efficaces pour disperser les NPs à petite échelle, elles augmentent le risque de ré-agglomération dû à la présence d'une forte force de pont-liquide et des opérations de post-traitement (p. ex. filtration et séchage). En outre, les surfactants sont confrontés à plusieurs limitations, dont leur faible stabilité thermique qui limite leur application dans les procédés à haute température tels que les nanofluides, les nanocomposites et les polymères thermodurcis. Les méthodes en phase gazeuse présentent plusieurs avantages par rapport à celles en phase liquide, comme l'absence de déchets de solvants, la simplification de la séparation en aval, la faisabilité du traitement en continu et la polyvalence en ce qui concerne le matériau, la taille et la structure des particules. Par conséquent, la combinaison d'une méthode de désagglomération en phase gazeuse avec une technique de revêtement en phase gazeuse peut ouvrir la voie à la production de NPs stables.

Au cours des deux dernières décennies, plusieurs techniques de désagglomération et de revêtement des NPs en phase gazeuse ont été mises au point. Parmi elles, les lits fluidisés combinés à des techniques de revêtement telles que le dépôt de couches atomiques (ALD) et le dépôt chimique en phase vapeur (CVD) ont reçu plus d'attention. Malgré leur efficacité dans la désagglomération pendant le revêtement des NPs, éventuellement la désagglomération n'est pas contrôlable et celles-

ci finissent par enrober des agglomérats de NPs en raison de l'agglomération dynamique et du fait que les NPs sont fluidisées que sous forme d'agglomérat. Afin de briser les agglomérats d'une manière contrôlable et faisable à l'échelle commerciale, il est nécessaire de poursuivre les recherches, notamment sur les forces interparticulaires et l'obtention de l'énergie de désagglomération requise dans une configuration en lit fluidisé.

Ainsi, ce travail vise à mettre au point une nouvelle technique pour désagglomérer d'abord les NPs, puis les revêtir d'une manière contrôlable et extensible, en produisant des NPs dispersibles stables. Pour ce faire, nous décomposons le projet en trois étapes :

1) Concevoir et construire une technique contrôlable en continu pour désagglomérer les agglomérats de NP dans un lit fluidisé, en utilisant une configuration d'impacteur à jet ;
2) Établir un lien entre la distribution de la phase solide dans le lit fluidisé de l'impacteur à jet et l'énergie cinétique de l'impaction pour obtenir une fenêtre d'opération;
3) Mettre au point une technique de revêtement en continu à combiner avec un procédé de désagglomération et étudier les propriétés physico-chimiques des particules traitées.

Dans la première section, nous avons mis au point un procédé contrôlable en continu pour désagglomérer les NPs de silice fournie par l'industrie en utilisant un lit fluidisé assisté par impacteur à jet (JIAFB). La distribution granulométrique des NPs a été étudiée à différentes vitesses de jet et l'énergie de désagglomération a été approximativement calculée en utilisant une simulation CFD monophasée. Dans la deuxième section, afin de définir une fenêtre d'opération permettant de maximiser la probabilité de rupture de l'agglomérat, nous avons étudié la concentration et la vitesse des particules à proximité de l'impacteur à jet en utilisant respectivement la technique de densitométrie à rayons gamma et la simulation CFD à deux phases. La multiplication de ces profils illustre où se produit le moment d'impaction maximale. Ces résultats ont ensuite été confirmés en mesurant les forces appliquées de l'écoulement du jet jusqu'à l'impacteur à l'aide d'un capteur de force. Dans une perspective plus large, cette partie était également importante pour comprendre en profondeur comment l'ajout d'un jet de gaz secondaire modifie l'hydrodynamique du lit fluidisé de nanopoudre. Dans la dernière partie de cette thèse, une nouvelle technique de revêtement en continu basée sur le dépôt chimique en phase vapeur photo-initié (PICVD) a été combinée avec le JIAFB pour revêtir les NPs désagglomérées. Le revêtement carboné, à base de polyméthacrylate de méthyle (PMMA), passivait la surface des NPs et réduisait

les forces interparticulaires pour éviter une ré-agglomération. De plus, l'efficacité du revêtement a été étudiée en comparant le comportement de dispersion des particules nues et enrobées dans des solvants polaires et non polaires. La polyvalence de cette technique en continue, combinée au fait qu'elle fonctionne à la température et à la pression ambiantes, ne contient pas de solvants et a une grande capacité d'absorption fait d'elle une méthode prometteuse en tant qu'opération unitaire à intégrer dans les procédés de synthèse en continu de nanopoudres aérosols.

ABSTRACT

Nanoparticles (NPs) are now produced commercially and being used for myriad of purposes from industrial applications such as catalysts to cancer-drug delivery to sunblock in cosmetics. However, there is still a main challenge in their production, storage and process: agglomeration. When NPs form agglomerates, those lose their extraordinary surface-driven properties they had as individual NPs. In order to take advantage of their "nanoproperties", it is necessary to break up the agglomerates and reduce their high surface energy, or "passivate" them, before use. The ability to produce bulk quantities of highly dispersed NPs is a significant limitation of nanotechnology.

Traditionally, de-agglomeration and stabilization of NPs are performed in the liquid phase, since many synthesis reactions and processes occur in liquids. Ultrasonication combined with surfactants is a typical technique for dispersing and stabilizing NPs in the liquid phase. While solvent-based techniques are generally effective at dispersing NPs at a small scale, they increase the chance of re-agglomeration due to the presence of strong liquid-bridge force and post-treatments operations (e.g. filtering and drying). Further, surfactants face several limitations, not the least of which is their poor thermal stability which limits their application in high temperature processes such as nanofluids, nanocomposites and thermoset polymers. Gas phase methods have several advantages over liquid-phase approaches, such as the absence of solvent waste, the simplification of downstream separation, the feasibility of continuous processing, and versatility with respect to particle material and size and structure. Hence, combining a de-agglomeration gas phase method with a gas phase coating technique can open up an opportunity toward producing stable NPs.

In the past two decades, several gas phase techniques for de-agglomerating and coating of NPs have been developed. Among them fluidized beds combined with coating techniques such as atomic layer deposition (ALD) and chemical vapor deposition (CVD) techniques have received more attention. Despite their efficiency in de-agglomeration during coating of NPs, eventually the de-agglomeration is not controllable and those end up coating agglomerates of NPs. Because of dynamic agglomeration and the fact that NPs are fluidized only in agglomerate form. In order to break the agglomerates in a controllable and scalable manner, further investigation is necessary, namely on interparticle forces and attaining the required de-agglomeration energy in a fluidized bed configuration.

Therefore, this work aims to develop a novel technique to first de-agglomerate, then coat NPs in a controllable and scalable manner, producing stable dispersible NPs. For this purpose, we break down the project into three following steps:

1) To design and construct a continuous controllable technique for de-agglomerating NP agglomerates in a fluidized bed, using a jet-impactor configuration;

2) To link the solid phase distribution in the jet-impactor fluidized bed with the kinetic energy of impaction to formulate an operating window

3) To develop a continuous coating technique to be combined with de-agglomeration process and investigate the physico-chemical properties of treated particles

In the first section, we have developed a continuous controllable process to de-agglomerate industrially supplied silica NPs using a jet-impactor assisted fluidized bed (JIAFB). The particle size distribution of NPs was studied at different jet velocities and de-agglomeration energy was roughly calculated using a single-phase CFD simulation. In the second section, in order to formulate an operating window for maximizing the probability of agglomerate breakage, we investigated the particle concentration and velocity in the vicinity of the jet-impactor system using gamma-ray densitometry technique and two-phase CFD simulation, respectively. Multiplying those profiles illustrates where the maximum momentum of impaction occurs. Those results, then, were confirmed by measuring applied forces from the jet flow to the impactor using a force sensor. In a broader view, this part was, also, important for deep understanding of how adding a secondary gas jet changes the hydrodynamic of fluidized bed of nanopowder. In the final part of this thesis, a novel continuous coating technique based on photo-initiated chemical vapor deposition (PICVD) was combined with the JIAFB to coat de-agglomerated NPs. The carbonaceous coating, based on polymethyl methacrylate chemistry (PMMA), passivated the NP surface and reduced the interparticle forces to prevent re-agglomeration. In addition, the coating efficiency was studied by comparing the dispersion behavior of bare and coated particles in polar to non-polar solvents. The versatility of this continuous technique, combined with the fact that it operates at ambient temperature and atmospheric pressure, is solvent-free and has low scaling costs, makes it a

promising candidate as a unit operation to be integrated into continuous aerosol nanopowders synthesis processes.

TABLE OF CONTENTS

LIST OF TABLES

LIST OF FIGURES

LIST OF SYMBOLS AND ABBREVIATIONS

ALD   Atomic layer deposition

CFD   Computational fluid dynamics

D50   Median diameter

FTIR   Fourier-transform infrared spectroscopy

GM   Geometric mean (diameter)

GSD   Geometric standard deviation

JIAFB   Jet-impactor assisted fluidized bed

MIONP   Magnetic iron oxide nanoparticle

NP   Nanoparticle

Nano-TiO_2 Titanium oxide nanoparticle

PECVD   Plasma-enhanced chemical vapor deposition

PI   Photo initiator

PICVD   Photo-initiated chemical vapor deposition

PS   Photo sensitizer

RESS   Rapid Expansion of Supercritical Suspensions

SD   Standard deviation

SMPS   Scanning mobility particle sizer

TACVD   Thermally-activated chemical vapor deposition

TEM   Transmission electron microscope/microscopy

U   Fluidization velocity

U_j Jet velocity

U_{mf} Minimum fluidization velocity

LIST OF APPENDICES

CHAPTER 1   INTRODUCTION AND MOTIVATION

Nanoparticles (NPs) are particles in the size range of 1 to 100 nm with outstanding combined properties. They have unique physical and chemical properties such as mechanical, electrical, optical, and chemical properties which make them different from their counterparts. Adding a small amount of these particles to different materials such as polymers, composites, and fluids enhances their performance in different aspects such as mechanical, optical, electrical, and other properties. To date, the application of NPs has exponentially grown in a broad range of fields such as electronics, catalysis, drug delivery, sensors, cosmetics, pharmaceutical equipment, and air/water remediation. Unique properties of NPs stem from their high surface area to volume ratio and the presence of free atoms on their surfaces. For those reasons, the properties of their bulk are different than those of individual NPs. However, the presence of free atoms on the particle surface is a double-edged sword: this increases their surface energy and makes them highly unstable and prone to sticking together and build larger structures, called "agglomerates". The agglomeration of NPs occurs during their production, transportation, storage, or process due to the presence of interparticle forces (van der Waals, electrostatic and/or capillary forces). Agglomeration not only leads to heterogeneity in NP properties because of polydispersity, but also causes particles to lose their extraordinary "nanoproperties". For example, agglomeration of metal nanoparticles, as catalysts, in fuel cells significantly decreases their electrocatalytic properties that leads to reduction of their performance. Hence, it is essential to break up agglomerates and stabilize them before use. The ability to produce bulk quantities of stable NPs with homogeneous properties is a major limitation of nanotechnology.

Techniques for de-agglomeration and stabilization of NPs have been traditionally developed in the liquid phase based on the classical wet chemistry, but other new methods, resulting from combining fluidization and gas phase treatment techniques (e.g. atomic layer deposition, plasma, and chemical vapour deposition) and aerosol-based techniques are growing quite fast. While liquid phase techniques are generally effective at dispersing NPs, they do not directly address the issue of re-agglomeration. From a processing point of view, they suffer from using toxic or environmentally unfriendly solvents, introduction of impurities, complex preparation methods, and downstream operations (e.g. filtration, separation and drying) which are time consuming and eventually lead to further agglomeration. Moreover, from a stabilization point of view, using surfactants and additives

has several limitations, not the least of which is thermal instability. On the other hand, gas phase techniques offer inherent advantages such as the absence of solvent waste, less separation problems, the feasibility of continuous processing as opposed to batch processing, and versatility with respect to particle material and size and structure. Among gas phase methods, the continuous aerosol-based techniques are preferable since de-agglomeration and stabilization is more controllable. In the opposite, the batch and semi-batch processes (e.g. fluidized beds) suffer from dynamic agglomeration, which leads to heterogeneity in product such as variation of the particle size distribution from batch to batch. This process heterogeneity, then, propagates through commercial products and limits their impact. This affirms nanopowders must be de-agglomerated before any process in a controllable manner.

Despite vast studies on de-agglomeration and coating processes on NPs, this issue has not been addressed through in the literature. Hence, this research aims to develop a controllable and scalable technique for producing stable de-agglomerated NPs from supplied agglomerated nanopowders towards producing stable individual NPs. In this research we focus on metal oxide NPs such as silica (SiO_2), magnetic iron oxide (Fe_2O_3), and titania (TiO_2) NPs. Metal and metal oxide NPs are among the most widely studied nanomaterials given their uses in a broad range of fields. For example silicon dioxide (SiO_2) is used as an additive in the food industry because of its functionality as an anti-binder, anti-foaming agent, viscosity controller, desiccant, beverage clarifier and as an excipient of medications and vitamins. Similarly, photocatalytic properties of TiO_2 NPs make them suitable to be used as photocatalytic degradation and splitting, photovoltaic cells, electrochromic devices, hydrogen storage, and sensing instruments.

CHAPTER 2   LITERATURE REVIEW

2.1 Nanoparticles

Nanotechnology refers to science involving matter or the manipulation of matter at the scale of 1 billionth of a meter (10^{-9} m). NPs are the most fundamental component in the fabrication of nanostructured materials, which are leading technologists beyond the scale where Newton's laws govern the world. There have been diverse definitions for NPs; however, the definition suggested by NASA [1] and Britanica [2] is accepted as the most thorough description: "the creation of functional materials, devices and systems through control of matter on the nanometer length scale (1–100 nm), and exploitation of novel phenomena and properties (physical, chemical, biological) at that length scale" [1]. According to ISO defines nanoparticles as "nano-objects that all external dimensions in the nanoscale where the lengths of the longest and the shortest axes of the nano-object do not differ significantly" [3]. In many cases, NPs are defined as ultrafine particles in the range of 1 and 100 nm in size.

NPs have two key features that bring about different properties from the bulk materials of the same materials: particle surface activation, and high surface area to volume ratio. These changes in fundamental properties are called "size effect" or "quantum effect". For instance, metallic NPs have different physical and chemical properties from bulk metals such as lower melting point, specific optical properties, mechanical strength, and specific magnetization. All solid materials consist of atoms and molecules. As they break into the ultrafine particles, they begin to show different behavior from those of the bulk solid. In other words, they tend to be influenced by their atoms and/or molecules themselves. This behavior is attributed to the free atoms on their surfaces. The free atoms or unbounded atoms are the fraction of atoms which are located at the surface of the NPs and because of their free hand they can readily bond with other materials or response to the energy. Kittel and McEuen [4] showed that with an assumption of atomic distance of 0.2 nm for a cubic particle, the fraction of surface atoms for a particle size of 20 μm is only 0.006%, however for a particle size of 200 nm it rises up to 0.6%, and finally for a 2 nm particle size, more than half of the atoms are located on the surface of particles. Table 2.1 shows this calculation for particles with different sizes. The optical properties of gold particles is a well-known example of changing property as a result of changing particle size. Smaller nanospheres (~30 nm) primarily

absorb light near 520 nm (blue-green portion), while larger spheres show increased scattering and the peaks shift towards longer wavelengths (known as red-shifting).

Table 2.1 Relation between cubic particle size and free atoms on the particle surface [4]

Numbers of atoms in a side	Number of atoms at the surface	Total number of atoms	Number ratio of surface atoms (%)	Example of particle size and powder
2	8	8	100	
3	26	27	97	
4	56	64	87.5	
5	98	125	78.5	
10	488	1,000	48.8	2 nm
100	58,800	1×10^6	5.9	20 nm (colloidal silica)
1,000	6×10^6	1×10^9	0.6	200 nm (titanium dioxide)
10,000	6×10^8	1×10^{12}	0.06	2 µm (light calcium carbonate)
100,000	1×10^{10}	1×10^{15}	0.006	20 µm (green tea powder, chalk)

Concurrently, when we crush particles, the surface area to volume ratio of particles increases. It is computed that when a particle of 1 cm is micronized into 1 µm and 10 nm particles, the specific surface area increases ten thousand times and one million times, respectively. This affects directly the particle properties (e.g. reaction rate and solution of these particles through providing much more surface area in a smaller volume).

NPs are not a new discovery of science, nor are they an innovation, as regards to their definition based on their particle size or as a technical achievement. They have always been components of smoke. Their use as natural iron oxide and carbon black particles has already been applied in prehistoric cave paintings, such as in Altamira. Daniel et al. [5] and Horikoshi et. al. [6] have summarized the history of NPs from ancient times to the Middle Ages. The first use of NPs is attributed to the preparation of "soluble gold" for aesthetics and curative purposes around the 5th or 4th century B.C. in Egypt and China. NPs have also been used because of their attractive optical properties in sculptures, paintings, and glass windows. The Lycurgus cup, made in the 4th century A. D., is the most famous example of a very special type of glass, known as dichroic glass, that

changes color when held up to the light [7]. The result of analysis shows that manufacturers have used a very small amount of metal crystals of silver and gold (~70 nm) in an approximate molar ratio of 14:1, which provide such unusual optical properties. The first book about colloidal gold was written in 1618 by the philosopher and medical doctor Francisci Antonii [8]. It contains information about methods of preparing colloidal gold and its application in medicine [9]. Another evident application of NPs is in colorful windows of old churches. In a New York Times article [10], Kenneth Chang described the relationship between the color of stained glass and the size/shape of the NPs used in these ancient stained glass. A chronological table in connection with NPs (nanotechnology) is presented by Horikoshi et al. [6] that illuminates the application of NPs since 1200-1300 BC up to current century.

Figure 2.1 Lycurgus cup, 4th century A. D. in the British Museum, is the most famous example of a very special type of glass [7]

Although the application of nanotechnology is relatively new, the history of developing this field as a science dates back to 1959, when Richard P. Feynman, a physicist at California Institute of Technology, forecasted the emerging of nanomaterials. He suggested that scaling down to nano-scale and starting from the bottom would be the key to future technology and advancement [11].

1.1.1 NP Classification

There are different classifications of NPs, proposed by various authors according to the diameter of a particle as well as the number of atoms in a particle [12], dimension [13], and the constituents [14]. Based on the constituents, NPs can be classified into five categories:

1) Fullerenes (Carbon 60) and Carbon Nanotubes (CNTs)

2) Quantum dots

3) Polymeric NPs

4) Metalic NPs

5) Ceramic/Metal oxide NPs

Fullerenes (Carbon 60): Fullerenes are hollow spherical cages containing 28 to more than 100 carbon atoms; includes carbon 60 (C_{60}). The carbon atoms are interconnected in the structure as pentagons and hexagons. Because of their unique structure, they show extraordinary properties such as regaining their shape after releasing extreme pressure and electronic properties. This provides them major potential for applications as electronic field, data storage, lubricants, and medical applications [15].

Quantum Dots (QDs): Quantum dots are semiconductor nanocrystals with unique optical and electronic properties. They are composed of combinations of chemical elements from Groups II and IV or Groups III and V of the periodic table. Because of their unique optical and electronic properties, they have been developed in form of semiconductors, insulators, metals, magnetic materials or metal oxides. They can be used for optical and optoelectronic devices, solar batteries, fast DNA tests, therapeutic agents for simultaneous drug delivery, *in vivo* imaging, and tissue engineering [16]. QDs can have from a single electron to a collection of several thousand electrons with precise control of their number, shape, and size. Cadmium selenide (CdSe), cadmium telluride (CdTe), indium arsenide (InAs), and indium phosphide (InP) are the most commonly used QDs [17, 18].

Polymeric NPs (PNPs): Polymeric NPs are prepared from polymers based on two main methods: dispersion of preformed polymers or polymerization of monomers. Various techniques can be utilized to produce polymer NPs, such as solvent evaporation, salting-out, dialysis, supercritical fluid technology, micro-emulsion, mini-emulsion, surfactant-free emulsion, and interfacial polymerization. Suitable preparation methods are selected based on a number of factors such as the type of polymeric system, area of application and size requirement. For instance, a polymeric system that is developed for an application in the biomedical or environmental fields should be completely free from additives or reactants such as surfactants or traces of organic solvents. In this case, techniques like RESS (rapid expansion of a supercritical solution) or RESOLV (rapid expansion of a supercritical solution into a liquid solvent) can be selected [19, 20]. Polymer NPs

have attracted the interest of many research groups because of their potential in biomedical engineering applications such as drug delivery devices to particular organs and tissues. These NPs are also used as DNA in gene therapy and delivery of proteins, peptides, and genes through oral route administration [21]. Poly(lactic-co-glycolic acid) (PLGA) and polylactide-tocopheryl polyethylene glycol succinate (PLA-TPGS) are commonly used polymer NPs in biomedical applications. Also, dendrimers are one kind of polymeric NPs constructed by the addition of layers of branching groups. The properties of dendrimers are dominated by the functional groups on the molecular surface. Dendrimers can be used as detecting agents (such as a dye molecule), affinity ligands, targeting components, radioligands, imaging agents, pharmaceutically active compounds (drug and gene delivery), and solubilizing agents [22, 23].

Metallic NPs (MNPs): Metallic NPs such as gold, iron, titanium, silver, copper are widely used in catalysis, sensing, photonics, environmental cleanup, imaging, electronic storage system, magnetic separation, and specifically biomedical science such as targeted drug delivery and vehicles for gene and drug delivery [24-26]. They are a center of interest because these materials can be produced and modified with various functional groups which makes them unique materials to be conjugated with antibodies, drugs, and different ligands in order to utilize in a vast range of applications. In addition, metallic NPs take advantage of having unique optical, electrical, and magnetic properties which are different compared to their larger counterparts. This difference in physiochemical properties of metallic NPs makes them excellent candidate for biomedical applications as variety of biological process occur at nanometer scales [24].

Ceramic/Metal oxide NPs: Ceramic NPs are synthesized from inorganic, non-metallic materials mostly consist of nitrides, oxides, or carbides such as silica (SiO_2), alumina (Al_2O_3), zirconia (ZrO_2), and tungsten carbide (WC) NPs [27]. Because of their heat resistance and chemical inertness, these materials are excellent candidates for coating materials. Some of them such as zirconia are utilized as medical implants because of their biocompatibility, or as membrane components in fuel cells. Superconducting wires made of ceramic NPs are more flexible compared to the traditional ceramic materials [28].

Inorganic NPs, i.e. metal and metal oxide NPs, are among the most widely studied nanomaterials given their uses in a broad range of fields such as electronic, catalysis, drug delivery, sensors, cosmetics, pharmaceutical equipment, and air/water remediation. Tailoring nanoparticles for

specific applications through surface treatment has been the focus of vast research in the past two decades [29-35].

2.2 Agglomeration and Aggregation

Powders generally consist of a complex blend of primary particles and particle assemblages in the form of agglomerates and aggregates. Primary particles are discrete particles which may have different geometrical forms, for instance in spherical, cuboidal, or rod-like geometry. Primary particles can collect into assemblages as a result of interparticle bonding, sintering, fusion, and growth during crystallization (for crystalline substances) in the mother liquor, filtration, drying, milling, transfer, or storage of the final bulk powder. The final assemblages can be as small as two-particle assemblages or huge fractals with joined primary particles in random arrays [36].

Powder technologists use different terminologies for such assemblages, including agglomerate, aggregate, coalescence, or coagulation. Some of these terms tend to be used frequently when referring to charged species in a liquid phase. However, agglomerate and aggregate are two distinct terms that have a specific meaning but, unfortunately, are frequently interchanged. Nicholas et al. have made an effort to clarify these terminologies [36]: agglomerates or soft agglomerates are friable and readily dispersed assemblages of particles, whereas aggregates or hard agglomerates are non-friable, gritty, and not readily dispersed particles. An agglomerate is a loose array of attached primary particles for instance at the corners and edges. Thus, total surface area of an agglomerate does not differ appreciably from the sum of the surface area of the individual particles. Conversely, an aggregate consists of primary particles attached at their surfaces. Therefore, total accessible surface of final aggregate compared with the sum of the surface of the individual particles is reduced. Discriminating between particle assemblages is essential since the degree of association of particles in an assemblage determines their behavior in the process through changing the particle characteristics.

Generally, soft agglomerates will not affect the properties of bulk powders because they tend to be broken up by relatively mild forces in the process [37]. In fact, soft agglomerates may facilitate the flowing of powders by making them more cohesive. On the other hand, the presence of hard agglomerates or aggregates in a powder may have a contrary effect on the behavior of the powder bulk. By making discrete, polycrystalline, and larger particles, they decrease the dissolution rate

and influence the flow by reducing the cohesiveness of particles. Aggregates, because of their stronger bonds between constituent particles, will not tend to be dispersed during bulk powder processing such as blending or powder transfer [38].

Accordingly, agglomerates are not fixed units, and the agglomeration phenomenon in a medium is dynamic. Their shape and size can vary based on changing parameters of the surrounding medium e.g. pressure, temperature, density, viscosity, pH. Larger agglomerates may break down into smaller agglomerates or, adversely, smaller agglomerates may join together and form larger agglomerates. The density of agglomerates depends on the particle size distribution of the primary particles (based on assumption of equal geometry and chemical composition) [36].

Although aggregates and agglomerates are two different kinds of assemblage, they can occur at the same time during the formation of a larger particle. For example, five primary particles form an agglomerate by adhesion. When crystal growth begins, two different agglomerates may be converted into one new larger formed particle which is an aggregate. The particles are firmly fused together; however, the original geometry of the primary particles is still visible in the final aggregate, as can be seen in Figure 2.2.
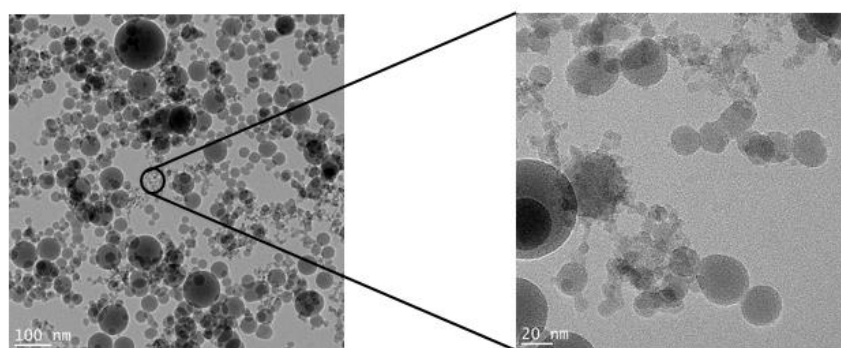
Figure 2.2 TEM micrograph of SiO2 NPs manufactured by TEKNA containing primary particles, agglomerates, and aggregates

From another perspective, such agglomerates are macroscopically perceived as one particle and may break down into their primary particles in biological materials; this dissociation phenomenon is related to their toxicological properties [39]. Nanotoxicology is the subdiscipline of the science of toxicology that is concerned with understanding the adverse effects resulting from exposures to nanomaterials in biologic systems, including effects to humans, animals, and the environment.

Research in this field shows that NPs, due to their very small size, are able to pass through cells or be adsorbed via the respiratory tract. Therefore, from this aspect, being stable in agglomerated form is crucial [40].

2.3 Characterization of Agglomeration

The strength of an agglomerate particle in a nanopowder bulk mainly depends on the interparticle forces between its constituent primaries and internal coordination numbers [41]. These will affect its resistance to break up under stress, and ultimately also determine bulk material properties such as cohesiveness and deagglomeration of powders. Accordingly, in order to study the behavior of nanopowders, it is important to know which type of interparticle forces are involved along with the fractal dimension, a parameter representing the coordination number in an agglomerate or aggregate.

2.3.1 Interparticle forces

When two particles in a gaseous media or in a vacuum environment come close, they usually experience attractive forces. Inefficient powder dispersion in gaseous environment occurs due to these interparticle forces which are, from strongest to weakest: 1) solid bridge force, 2) liquid bridge force, 3) van der Waals force, 4) electrostatic force, and 5) other forces such as magnetic force, hydrogen bond.

2.3.1.1 Capillary or Liquid Bridge Force

In humid environments, as a result of condensation on the particle surfaces, a liquid bridge forms among neighboring particles. Thus, an attractive force between particles is produced due to the surface tension of the liquid and pressure deficiency in the bulk of the liquid [42, 43]. Capillary condensation of the fluid in the void between the particles in close contact may occur at high humidity ($> 65\%$), as illustrated in Figure 2.3, resulting in an additional attractive force to the van der Waals attraction. This force, F_c, for two smooth, spherical particles of radius R and a fluid of surface tension γ is given by:

$$F_c = 2\pi\gamma R \hspace{4cm} \text{Equation 2.1}$$
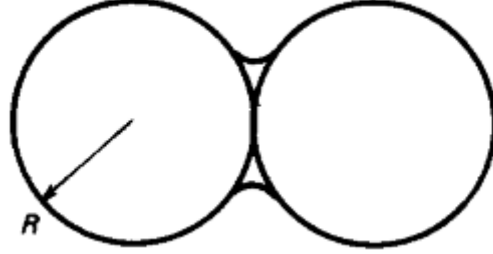
Figure 2.3 Capillary condensation of fluid in the void between two neighboring particles

2.3.1.2   Van der Waals Force

When two particle approach each other, they begin to affect each other due to van der Waals force (F_{vdW}). Hamaker [44] proved that this force for the particles with the same composition is always attractive. This force arises due to the dispersion effect which is the interaction between instantaneous dipoles formed in their atoms by orbiting electrons [45]. For two smooth spherical particles this force calculated by formula presented by Krupp [46]:

$$F_{vdW} = \frac{h\overline{\omega}}{8\pi Z^2} R \left(1 + \frac{h\overline{\omega}}{8\pi^2 Z^3 H_r}\right) \hspace{3cm} \text{Equation 2.2}$$

Where $h\overline{\omega}$ is the Liftshits-van der Waals coefficient which is a function of the nature of the bodies in contact and of the surrounding medium, H_r is the hardness of particles, R is the particle radii, and Z is the distance between two particles. The simplified version of this equation was presented by Hamaker earlier [44]:

$$F_{vdW} = \frac{A}{12Z^2} \left(\frac{d_i d_j}{d_i + d_j}\right) \hspace{3cm} \text{Equation 2.3}$$

where A is the Hamaker constant (a material property that represents the strength of van der Waals interactions), Z is the distance between particles, and d_i and d_j are the diameters of the spheres. The Hamaker constant in the gas phase, in general, is larger than in the liquid phase [47] .In the absence of solid bridge and liquid bridge forces, van der Waals force is the most dominant interparticle forces as particle size decreases [48]. The amount of this force is approximately 100 times greater than gravity for 10 μm particles [49].

2.3.1.3 Electrostatic Force

Electrostatic force (F_E) is another interparticle force leading to the formation of agglomerates in a gaseous medium [50]. The electrostatic charge strongly depends on the interaction history of particles with other materials, causing an exchange of electrons in their surface layer. This phenomenon is called "triboelectrification" and causes the particles to be electrically charged. Electrostatic force for two spherical particles with sizes much smaller than the distance between them, acting along a straight line from one to the other is given by Coulomb's Law [51]:

$$F_E = \frac{1}{4\pi\epsilon} \frac{q_i q_j}{Z^2} \qquad \text{Equation 2.4}$$

where constant ϵ is the permittivity of free space ($8.85{\times}10^{-12}$ C^2.m^2.N^{-1}), q_i and q_j are the charge of the particles (C), and Z is the distance between two particles (m). Electrostatic forces are typically less relevant at the sub-micron scale. They can, however, play an important role as a force between agglomerates.

2.3.1.4 Additional Specific Attractive Forces

A specific additional attraction may occur when particles can be magnetized. Due to the long range of magnetic forces, very high attraction forces can be attained, depending on the degree of magnetization, p. Only for weakly magnetized particles such as magnetite the additional attraction forces are less pronounced but still noticeable [52]. This magnetic force F_M is given by:

$$F_M = \frac{p^2}{6\pi\mu H^2}$$
<div align="right">Equation 2.5</div>

In general, electrostatic and capillary forces are smaller than the ubiquitous van der Waals force [43]. According to the numerical calculations performed by Krupp [53], the additional attraction forces given above will only contribute to the omnipresent van der Waals attraction in extreme cases. In Figure 2.4 different interparticle forces have been compared. All forces are normalized by dividing them by the gravity forces on a single particle while the capillary force is given in the presence of water.
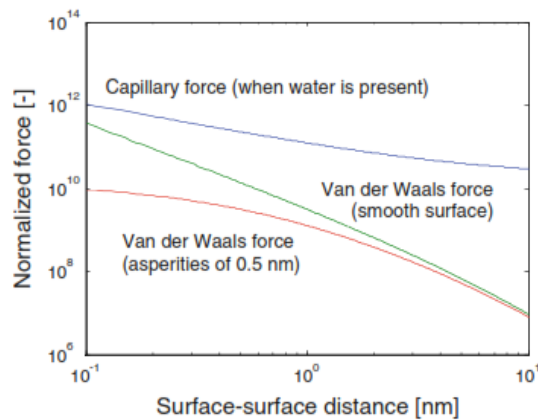
Figure 2.4 The main forces between two silica particles of 10 nm as a function of the interparticle distance [47]

2.3.2 Primary Particle Size and Fractal Dimension

Rather than interparticle forces, primary particle size as well as shape of the agglomerate or aggregate are two important characteristics that can describe the behavior of the nanopowders in different process conditions.

The concept of fractal dimension, developed in 1990 by Kaye, is very useful for this purpose [54]. The structure of agglomerates can be described by a power-law relation between the number of

primary particles per agglomerate and a characteristic agglomerate diameter. The exponent in this power law is called the fractal dimension:

$$N = A \left(\frac{d_p}{d_0}\right)^{D_f}$$

Equation 2.6

where N is the average number of primary particles per agglomerate, A the proportionality constant, d_0 the primary particle diameter, d_p the characteristic agglomerate diameter or mobility equivalent diameter, and, D_f the fractal dimension. For $D_f = 1$ the agglomerate is string-like, and the average number of bonds per primary particle is 2. For $D_f = 3$ the agglomerate is spheroidal, and the coordination number cannot be higher than 12. The limiting coordination number of 12 for closed-pack structure in three dimension has not been observed for aerosol agglomerates [55].

For agglomerates, the fractal dimension is often determined by analysis of transmission electron microscopy (TEM) micrographs. Moreover, an *in situ* technique has been developed to characterize the structure of aerosol agglomerates [55]. In this approach, kinetic of restructuring of online sampled nanoparticles are calculated based on the change in free energy per primary particle during restructuring. In aerosol technology, the fractal dimension can be used to calculate some physical properties of agglomerated powders, such as the rate of aggregation, mobility, drag resistance, and the rate of diffusion. This parameter represents the openness or compactness structure of the agglomerates, which can influence the physical properties of the powder. For instance, the openness of the agglomerate structure for TiO_2 pigments is related to the dispersion strength of the powder and consequently to its whiteness. Moreover, Shaeffer and Hurd have shown that fractal dimension is a useful parameter to describe the growth stages of agglomerates by different kinetic growth models [56]. The average coordination number of submicron agglomerate particles in aerosol can be estimated using the concept of fractal dimension on small scale [55]. Weber and Friedlander [57] indicated that for agglomerates with $2 \leq D_f \leq 2.4$, the coordination number calculated based on the fractal dimension showed a reasonable agreement with the results obtained by TEM analysis of low density silver NPs. However, for denser agglomerate ($D_f > 2.4$), the TEM image analysis was not successful due to shadowing effect. Two agglomerates with the same number of primary particle size but different fractal dimensions are illustrated in Figure 2.5.

$$N = 256, d_f = 1.8 \qquad\qquad N = 256, d_f = 2.5$$
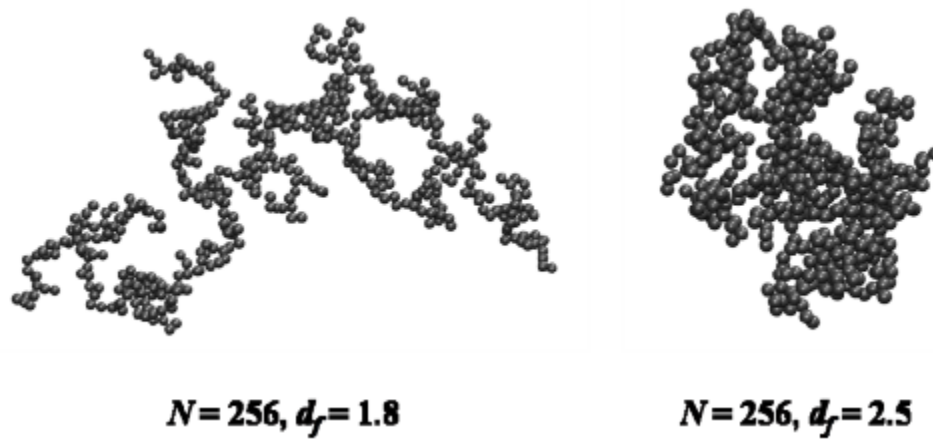
Figure 2.5 Two-dimensional fractal agglomerates containing 256 NPs with different fractal sizes [58]

Primary particle size is another important parameter to determine the strength of agglomerates. Zahardineck [58] and Froeschke et al. [41] investigated the fragmentation of micron and nano-size gas born agglomerates in an aerosol jet and impactor as a function of particle size. They observed that, with decreasing primary particle size, a higher stress intensity to the agglomerates (higher kinetic energy provided) is needed to attain the same degree of deagglomeration. Furthermore, they reported agglomerate fracturing halts for the agglomerates with very small primary particle diameter (less than three nanometers for silver NPs). This can be due to the relatively large interparticle attraction forces.

2.4 Fragmentability of aerosol agglomerates

To predict interparticle or adhesion forces, several mathematical models were developed [37, 41, 59-61]. There are mainly two approaches describing the stability of agglomerates by theoretical models [60, 62, 63]. The first model assumes the agglomerates consist of only two particles (two-particle approach) while the second assumes the spherical agglomerates consist of many primary particles (multi-particle-approach).

In the two-particle approach, JKR theory (developed by Johnson, Kendall and Roberts [64]) and DMT theory [65] (developed by Derjaguin, Muller and Toporov) are the most well-known. Both models include the effect of adhesion force on the deformation of an elastic sphere in contact with

an elastic half space. Muller et al. [66] introduced a Lennard–Jones potential (6–12 potential) into a model and showed that the JKR theory is applicable to soft materials and the DMT theory is applicable to hard materials, and also defined models for intermediate materials. One drawback with these theories is that the stress at the edge of the contact area has an infinite value. To have a better estimation of agglomerate strength, multi-particle approaches are more realistic. The planar fracture model of RUMPF [59] calculates the mean cohesive force (F) based on the pull-off force required to separate into two halves along its cross-section:

$$\sigma_z = \frac{(1 - \varepsilon)k\bar{F}}{\pi d_p^2}$$

Equation 2.7

where ε is the porosity of the agglomerate, k is the coordination number (mean number of contacts per primary particle), d_p the primary particle diameter, and σ_z is the tensile strength. It has been shown that this model overestimates the tensile strength due to inhomogeneties of real agglomerates, which leads to a breakage along the line of the least mechanical resistance [67, 68]. With regard to this limitation, Weiler et al. [60, 69] developed a new model that considers the total and prompt disintegration of a dry powder agglomerate with forces acting on the surface area of the whole agglomerate (Figure 2.6). According to this, the dispersion strength σ_{disp} is calculated as:

$$\sigma_{disp} = \frac{\bar{F}(1 - \varepsilon)k}{2\pi d_{agg}^2} \cdot \left(\frac{d_{agg}^3}{d_p^3} - \frac{4f}{b^2} \right)$$

Equation 2.8

Where d_{agg} and d_p are the agglomerate and particle diameter, respectively, b and f are non-dimensional parameters in the range of $0 < b < 1$ and $0.5 < f < 1$. They showed that for a ratio of $d_{agg}/d_p > 50$ the deviation between these two models is below 4%. However, for dry powder composed of micron sized particles, the difference would be significant, and the Weiler model is instead recommended.
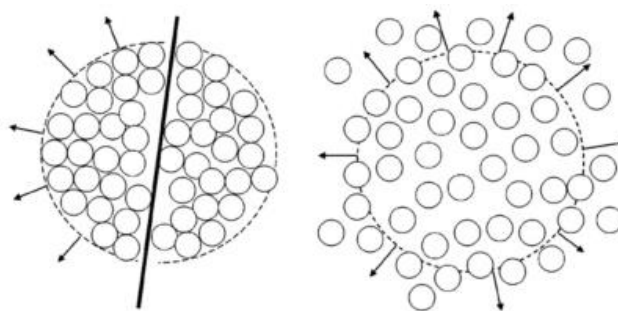
Figure 2.6 Planar fractal or RUMPF model (left) and Total dispersion or Weiler model (right) to estimate the mechanical stability of agglomerates [60]

It is worth mentioning that the pull-off force calculated based on the DMT model describes the separation of two spheres in the most effective way with the drag force acting in opposite directions. This is not likely for the particle separation in an agglomerate during its total disintegration. Thus, the pull-off force of DMT should be in principal smaller than the mean cohesive force calculated by Weiler due to the vectorial nature of the forces [69].

In a different approach, Weber and Sipenbusch [37, 41, 61] measured the agglomeration strength by impaction of gas-born nano-agglomerates from the aerosol phase in a single stage low pressure impactor (SSLPI, Fig 2.7). Based on this method, the strength of an agglomerate is mainly determined by the bond energies between its constituent primaries and the internal coordination numbers [41]. These two parameters affect its resistance and determine bulk material properties, such as cohesiveness and redispersion of powders. They performed different experiments at different impact velocities above the Stoke number range and analyzed the TEM images before and after impaction. Finally, a fragmentation curves obtained from impaction measurements shows the relation of fragmentation degree versus kinetic energy consumed to break up the agglomerates per unit mass of the particles (Fig. 2.7). The degree of fragmentation is defined as the fraction of broken bonds per agglomerate. The bond energies obtained by experiments exceeded calculated interparticle forces, considering pure van der Waals force, by a factor of about 5 [41]. These results showed better agreement compared to the JKR model [64], which had a difference by factor of about 3000 with calculated van der Waals forces. Although the SSLPI provides a controllable fragmentation of NPs, their scalability is limited by requiring extreme operating condition and complicated design.
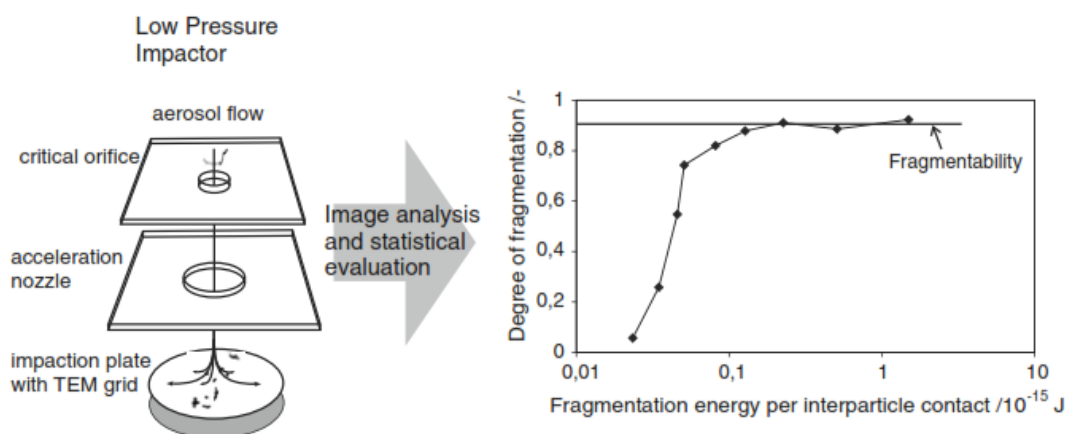
Figure 2.7 Schematic of the single stage impactor (SSLPI) for fragment analysis of nano-agglomerates and fragmentation curve [41]

2.5 Powder Dispersion

Dispersion is the controlled and desired fragmentation of particle assemblages down to their constituent primary particles by applying external forces larger than the interparticle attraction forces. The ability to control dispersion of a broad range of powders, from friable free-flowing agglomerates to robust cohesive aggregates, is an interesting and important field. However, the full disintegration of fine cohesive powders, especially in the size range below 20 µm [70] is difficult, due to the large interparticle attraction forces compared to separating forces [43]. The efficient dispersion of solid particles is of great interest in various industries dealing with powders, such as food, pharmaceutical, and bulk chemical industries. A further area where aerodynamic dispersion is highly important is in therapeutic drug delivery via the lungs using dry powder inhalers (DPIs). Powder dispersion is also used analytically to disintegrate loose agglomerates clusters to determine the particle size distribution, utilizing microscopy methods coupled with image analysis, laser diffraction, and time-of-flight techniques. Powder dispersion can be performed in gas or liquid phases, and a variety of theoretical and experimental studies have been investigated in both.

2.5.1 Liquid Phase

The suspension of solid particles in liquids provides useful advantages in several industrial systems including heat transfer fluids, lubricant fluids, and magnetic fluids [71]. Various techniques have been developed to disperse NPs in different fluids utilizing different mechanisms, including mechanical energy and acoustic energy. Mechanical dispersion methods are classified into stirring, high-speed revolution shearing, milling, and high-pressure jets. These still suffer from instability issues caused by NP agglomeration in the base fluids. To stabilize the suspension and prevent re-agglomeration, different approaches may be applied to impart electrostatic, steric and electrosteric effects. One common method is the addition of surfactants, resulting in electrostatic repulsion between surfactant-coated NPs [72]. This considerably reduces the particle agglomeration caused by attractive van der Waals forces [73]. Although surfactant addition is an effective way to improve the dispersibility of NPs, surfactants may cause several problems [74]. For instance, the addition of surfactants can contaminate the heat transfer media. Surfactants may produce foams when heating, whereas heating and cooling are routine processes in industrial systems. Furthermore, attaching surfactant molecules on the surface of NPs may increase the thermal resistance between the NPs and the base fluid, which limits the enhancement of the effective thermal conductivity of nanofluids [75]. It is worth mentioning that the behavior of solid particles in a liquid phase (colloid) is more developed than in the gas phase (aerosol). For the dispersion of NPs in liquid phase, various methods have been investigated.

2.5.1.1 Ultrasonication

Ultrasonication is a well-known and effective technique of dispersing NPs homogeneously in suspensions. The ultrasonic dispersion mechanism involves acoustic cavitation (formation, growth and implosion of bubbles resulting in the rupture of agglomerates) and acoustic streaming which cause inducing chaotic mixing [76]. If the suspension is not sufficiently stabilized against re-agglomeration resulting from attractive forces, NPs may regroup back into several hundred nanometer clusters shortly after ultrasonication. Therefore, stabilization may be carried out with electrostatic, steric and electrosteric effects. Time, power and irradiation modes (continuous or pulsed) affect the quality of the dispersion in an ultrasonic bath. Nguyen et al. indicated that there is an optimum power input in ultrasonication process, in which the breakup of NP clusters at higher

vibration amplitude will not show better result and re-agglomeration will occur during an ultrasonication process. Furthermore, under optimal conditions, continuous and pulsed irradiations showed almost the same efficiency of de-agglomeration over a given time [77].

2.5.1.2 Milling or Stirring

In milling, beads stirred by rotating pins impinge against a feed slurry introduced from the inlet located at the bottom of the mill (Figure 2.8). The impingement breaks aggregates in the slurry coming up through the mill. The slurry and the beads are separated by centrifugation in the upper part of the mill and only the slurry is discharged through the hollow shaft to the outside of the mill. Usually, the separated slurry is circulated to a feed vessel for repetition of the process. Beads less than 100 µm in diameter are effective for breaking and dispersing agglomerated NPs [78, 79]. Successful dispersion of nano-sized TiO_2 in liquid using 30 µm diameter beads has been reported [79].
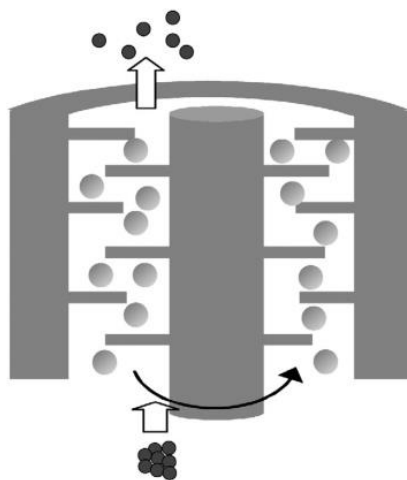
Figure 2.8 Schematic illustration of a bead mill system [51]

2.5.1.3 High pressure Homogenizer

High pressure homogenization is at the heart of many emulsification processes in the food, personal care and pharmaceutical industries. Several studies have applied this method to deagglomerate NP clusters in order to obtain homogeneous suspensions. Figure 2.9 presents a high-pressure homogenizer consisting of two microchannels, dividing a liquid inlet into two streams. Both divided streams are afterwards recombined in a reacting chamber. In this section, the significant

increase in the velocity of pressurized liquid streams in the micro-channels resulted in cavitation in the liquid, the high energy of which was used to break the NP clusters [80].
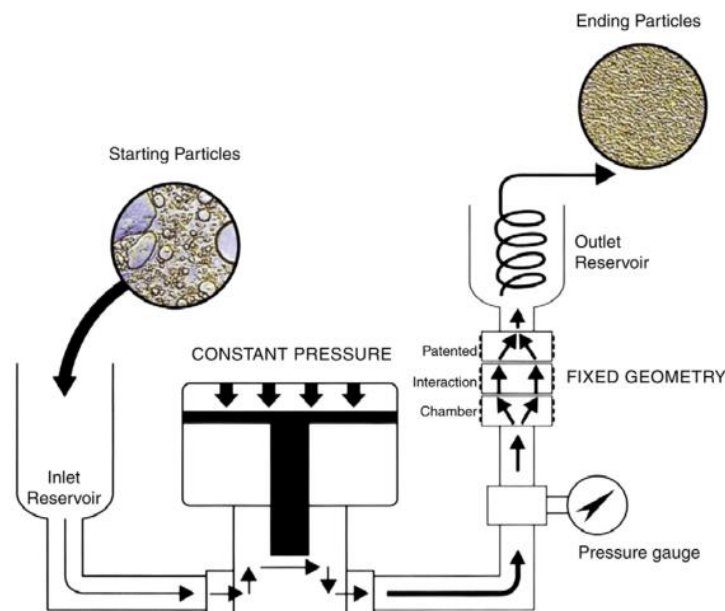
Figure 2.9 Schematic diagram of the high-pressure homogenizer for producing nanofluids [81]

Hwang et al. [81] compared the efficiency of different physical techniques in liquid phase on the dispersion of carbon black (CB, primary particle size of 40 nm) in deionized water and silver NPs (Ag, primary particle size of 35 nm) in silicon oil. In order to prevent the reagglomeration between primary NPs in the base fluid, either sodium dodecyl sulfate (SDS) or oleic acid was added as surfactants to coat the surface of CB and Ag NPs, respectively. They showed, after using various physical techniques including stirring, ultrasonication in a bath or with a disruptor and high-pressure homogenization, that the average diameter of CB NPs was reduced to 182 nm, 147 nm, 66 nm, and 45 nm, respectively, while for Ag NPs, the average diameter of particles was reduced to 150 nm, 90 nm, 40 nm, and 35 nm, respectively. These results indicate that the mechanical and cavitation energy generated by the stirrer and ultrasonication were not sufficient to break down clusters of primary particles. However, the high-pressure homogenizer was able to provide sufficient energy to deagglomerate the particle clusters through a combination of cavitation, shear force, and strong impaction on the NP clusters. Moreover, they reported the morphology of Ag NPs slightly changes which assumed to occur due to a strong impaction of particles in the micro-

channel inside the interaction chamber. TEM images of Ag NPs in silicon oil-based nanofluids presents in Figure 2.10.

(a) No physical treatment   (b) Stirrer   (c) Ultrasonic bath

(d) Ultrasonic disruptor   (e-1) High-pressure homogenizer   (e-2) High-pressure homogenizer
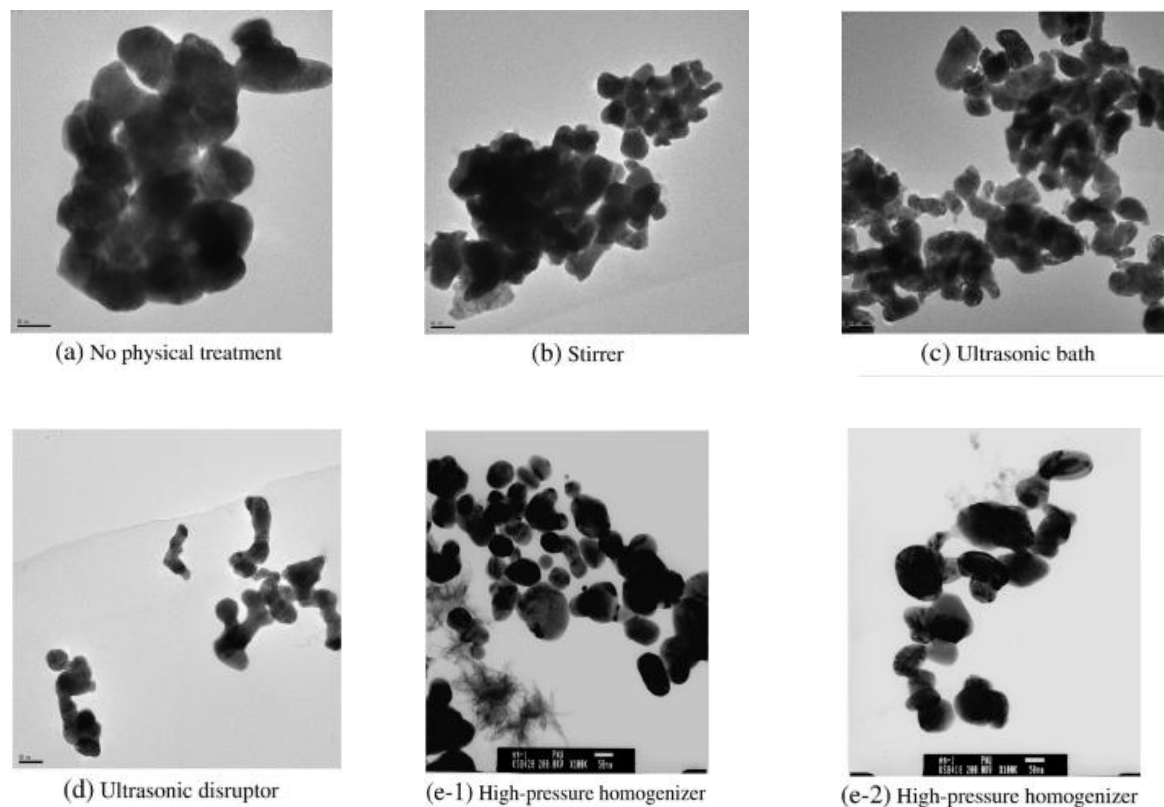
Figure 2.10 TEM images of Ag NPs in silicon oil-based nanofluids (The inserted scale bar is 50 nm.) [81]

2.5.2 Gas Phase

Breaking up aerosolized agglomerates or aerodynamic dispersion of bulk powders refer to the application of forces to overcome interparticle attraction and produce a cloud of primary particles. Primary particle size, as well as shape, density, packing structure (fractal dimension), porosity, contact area, and interparticle bond strength are the most important factors that need to be considered. For the control of dispersion and aggregation of NPs in gas phase, various methods have been investigated.

2.5.2.1   Nozzle

This device is the first and typical disperser. A report studying the breakage of coal dust agglomerates in a nozzle flow was first published in 1950 by Davies et al. [82]. In a typical nozzle disperser, an aerosol stream is accelerated and passed through a nozzle. As a result of shear flow due to the acceleration and subsequent sudden expansion, the agglomerates are dispersed.
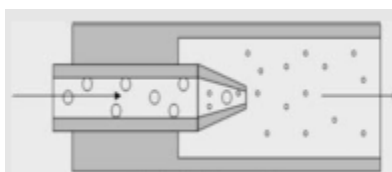
Figure 2.11 Schematic of a nozzle disperser [48]

2.5.2.2   Venturi

Similar to nozzles, venturi dispersers use sudden converging and expanding of particle laden flows over a short length to break up agglomerates. The main disintegration mechanism in this type of device is acceleration and deceleration which is an effective mechanism as long as the relative velocity between particle and carrier gas is large [83]. Kousaka et al. [83] reported that the relative velocity decrease required in the venturi decreases with particle size. Considering these two effects, the size distribution cannot be broadened or sharpened as a result of limitation in relative velocity, in particular for submicron particles.
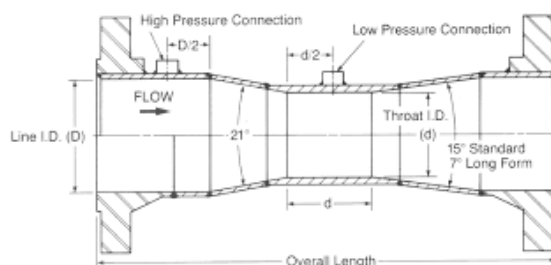
Figure 2.12 Typical venturi disperser [48]

2.5.2.3 Orifice

A standard orifice is a device with a sudden reduction followed by a sudden expansion that produce rapid acceleration and deceleration at one point. The possible mechanisms for de-agglomeration are acceleration of particles due to sudden contraction of gas flow, impact of particle at the orifice wall, velocity gradient of flow, and applying shear by turbulence. Yammamoto and Suganuma [84] found a relationship between the degree of dispersion and the intensity of the gas flow through the orifice:

$$\frac{D_{p50}}{D_{p50s}} = 31.3 \left(\frac{0.4 \Delta P \bar{u}}{d_0} \right)^{-0.2} \qquad \text{Equation 2.9}$$

where D_{p50s} is the mass median diameter of primary particles, D_{p50} median particle diameter, ΔP is the pressure difference over the orifice, $\bar{u}$ is the average fluid velocity, and d_0 the diameter of the orifice. According to this formula, in order to fully disperse the powder (i.e. $\frac{D_{p50}}{D_{p50s}} = 1$) it is possible to calculate the fluid flow rate. It is worth mentioning that fully dispersing the powder also depends on the properties of the powder such as cohesion, shape, packing structure, density, asperity.
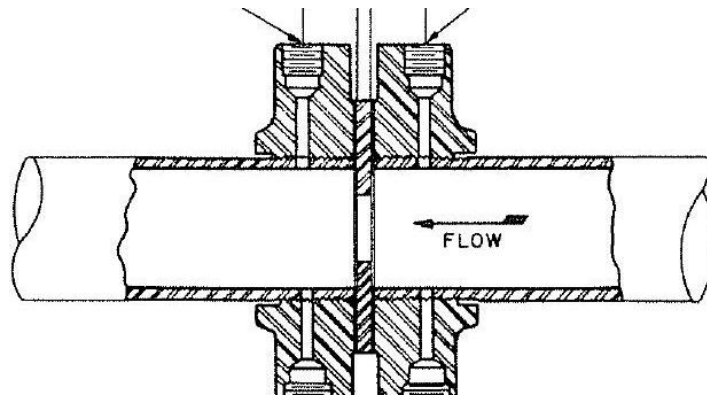
Figure 2.13 schematic of a typical orifice [85]

2.5.2.4 Capillary tube

The difference between the orifice and the capillary tube exists only in the length of contraction zone. A typical capillary tube disperser generally uses a velocity gradient across the cross section of the capillary to apply the shear to the agglomerates promoting dispersion. Experiments have

been done by Kousaka et al. [83] showed that controlling the dispersion mechanism of both orifice and capillary tubes is nearly similar. Because of the same dimension at their contraction zone, aggregates collide with the inlet plate of the capillary as well as the orifice plate by inertia in the same way as with the wire screens. In addition, they showed that the length of the capillary tube has no effect on the final particle size distribution. This means that the surviving clusters do not disintegrate further along the capillary tube through applying shear. Results obtained by Yamamoto [84] confirm this result as well.
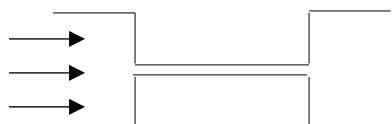
Figure 2.14 Schematic of a capillary tube disperser

2.5.2.5 Eductor

In contrast with nozzles, venturi, and orifices, typical eductors have two feed inlets; one provides a pressurized gas stream, and the other one introduces the particle laden flow into the system (Figure 2.15). Eductors are designed such a way that powder dispersion occur at the throat of the apparatus, where the pressurized stream and the powder stream come across. In this case, the breakage mechanisms include rapid acceleration and/or shear flow. Moreover, particle-particle and particle-wall collisions may assist the dispersion of powder. Two inlet feed streams may be reversed, so the powder stream may be introduced under the influence of gravity or an existing pressure difference between two inlets.
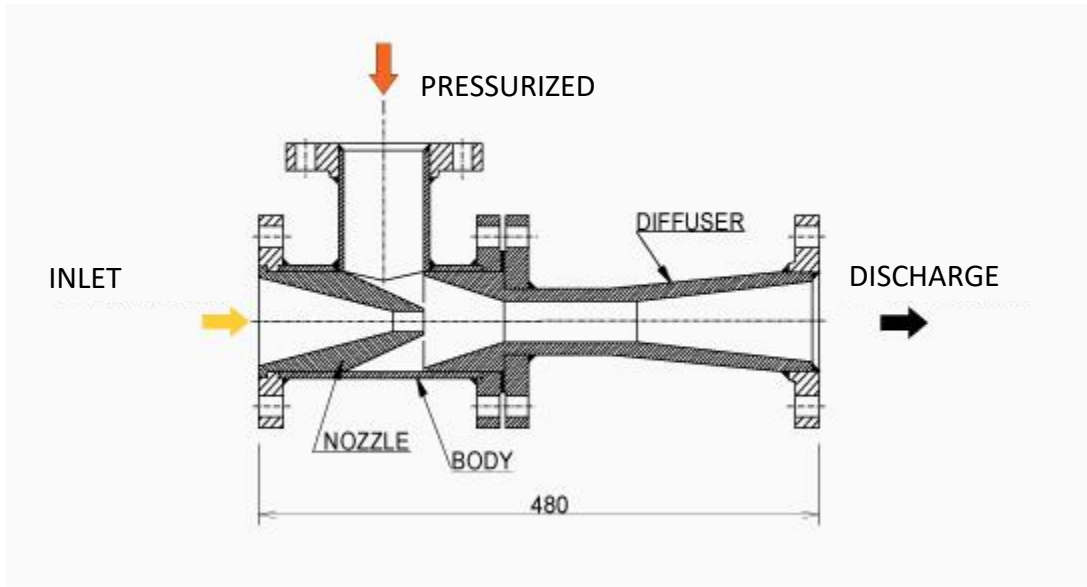
Figure 2.15 Typical eductor disperser [85]

An eductor designed by Nisshin Flour Milling Co. was used to investigate its performance and ability to disperse the fine powders [86]. Kousaka et al. [83] used the same apparatus to break up polystyrene latex agglomerates with diameter of 2 and 5.2 µm. Results showed the process of dispersing larger particles (i.e. 5 µm) is highly efficient, and it is possible to break up all the particles within this range of size. Additionally, Masuda and Gotoh [87] revealed that as long as the mass flow ratio is maintained constant, the performance of the eductor designed by Nisshin Flour Milling Co. [86] and the mixer type are similar. For smaller particle sizes, around 1 µm, Endo et al. [63] studied the effect of powder cohesion on the dispersion performance. They tried to predict the powder dispersion by defining a dimensionless Dispersibility factor (DS) as the ratio of produced dispersion force (F_d) to the interparticle force (F_{ad}).

$$DS = \frac{F_d}{2F_{ad}}$$
Equation 2.10

According to their results for several monodisperse and polydisperse latex particles, TiO_2 and SiC, they concluded that the theoretical dispersion and relative cohesion force are suitable parameters to characterize the degree of dispersion of powders. In a recent work, Tang et al. [88] used an online laser diffraction system for particle size measurement to compare their eductor disperser with two commercial models, model 3433 (TSI, Shoreview, USA) and the Scirocco dry powder disperser

(Malvern Instruments, Malvern, UK). They indicated that their eductor system worked as efficiently as the two commercial systems.

2.5.2.6 Mixer-type or rotating blade disperser

A standard mixer-type disperser is shown in Figure 2.16. Experimental and theoretical studies have indicated that, depending on how particles will be introduced into the system, there are different disintegration mechanisms for the powders in mixer-type dispersers. If the powders are fed into the system as an aerosol, it is less efficient in spite of producing turbulence in the system. If the powder is introduced into the disperser in agglomerate form, since the clusters are sufficiently large to be hit by the blade, the impaction action on the blade improves dispersion efficiency. Gotoh et al. [87] showed that the dispersibility of agglomerated particles depends on both the size of primary particles and the morphological structure of agglomerated particles. Moreover, they reported the agglomerates constituted of particles having a size near the median particle diameter were readily dispersed, while it is difficult to disperse particles with diameters in the tails of the size distribution diagram [87].
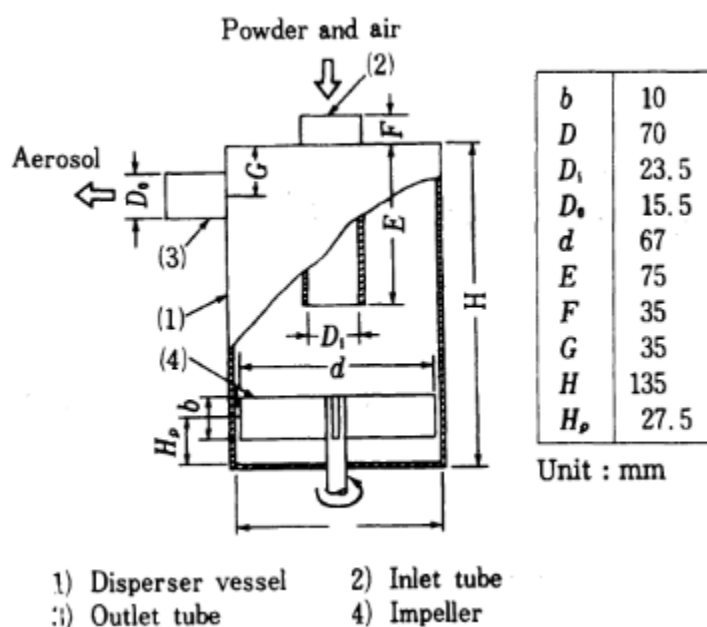
Figure 2.16 typical mixer type disperser [87]

2.5.2.7 Fluidized bed

Fluidized beds are used in different applications such as drying powders, gas cleaning, heat treatment for roasting or calcining, chemical reactions with gases or liquids (Figure 2.17). For processing small solid particles, gas-solid fluidized beds show significant advantages such as high heat and mass transfer rates, uniform and controllable bed temperature, high flowability of particles, ability to handle a wide variety of particle properties and suitability for large scale operations [89]. Even though during past decade several variations of this method such as jet-assisted, sound-assisted, or magnetic-assisted fluidized beds have been developed, dispersing and fluidizing cohesive group C powders (according to the Geldart classification [70]) and in particular ultrafine particles remains difficult. This problem is not only due to the interparticle attractive forces in these powders that are much larger than the gravitational forces, but also because the drag force applied on these particles by the gas is not sufficiently large for fluidization [43]. This difficulty is compounded when combining fluidized beds with techniques for particle surface treatment. As mentioned earlier, to overcome the problem of fluidization quality of NP agglomerates, different generated forces have been added to the method such as: acoustic [90], electric [91], or magnetic [92] fields, or mechanical vibrations [93]. Furthermore, using a centrifugal fluidized bed, a tapered fluidized bed, microjets as a secondary flow in the bed [94], and the addition of foreign particles have been considered as solutions. However, considering all these issues, NP dispersion remains a challenge in fluidized beds.
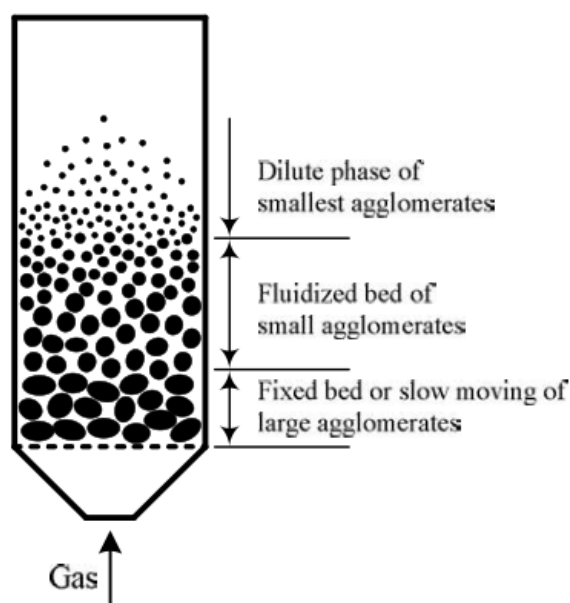
Figure 2.17 Schematic of a fluidized bed [42]

2.5.2.8 Impactor

Impactors are simple fluid-dynamical devices in which one or several gas jets entraining particles through a nozzle subsequently collide with an impaction plate that is perpendicular to the flow. The acceleration and/or shear flow through the nozzle and more importantly the impaction upon the stationary plate are the dispersion mechanisms. Kousaka et al. [83] examined an impactor equipped with eight wire screens, and by comparing with other methods such as nozzle, venturi, mixer-type, orifice, and capillary concluded that dispersion performed by impaction was the most efficient mechanism, as it is the most aggressive dispersion methods for the micron-sized powders. Furthermore, Froeschke [41] and Seipenbusch [37] proved that impactors are the best technique to provide sufficient energy to break up the agglomerates down to their primary particles for different metal and metal oxide NPs such as silver, titania, nickel, platinum NP with primary particle size of 3-8 nm (Ag), 95 nm (TiO_2), 4 nm (Ni), and 8-24 nm (Pt), respectively. Theoretical and experimental results obtained by de la Mora et al. [95] have shown that, in a slightly supersonic regime, it is possible to obtain sharp size distribution of particles under a critical pressure. In impactors, the force required to break up agglomerates is controlled by the pressure inside the impaction zone. Varying the pressure causes variations of the gas jet velocity that determines the kinetic energy of

particles upon impaction. Compared to other continuous techniques, this is the most developed technique regarding the theoretical and experimental works [37, 41, 95-103]. Although many researchers point to the dynamic process of agglomeration-deagglomeration, as yet no study has reported on the post treatment of fragmented NPs in the aerosol phase to counteract this reagglomeration issue and end up with stable de-agglomerated NPs.
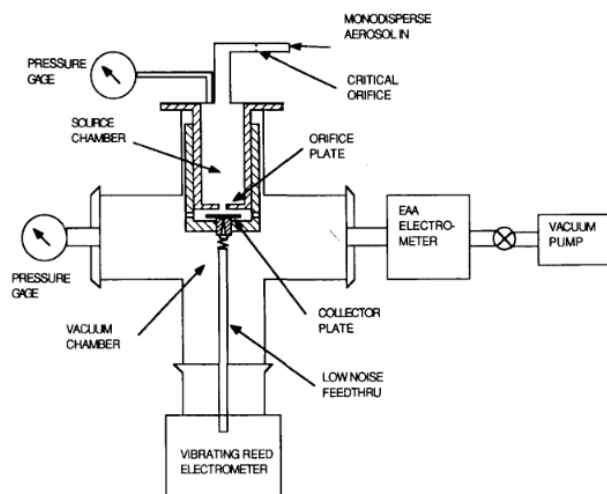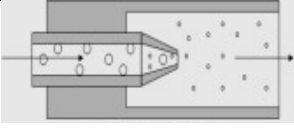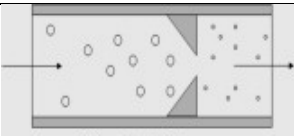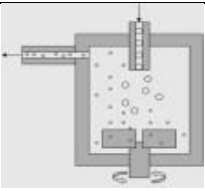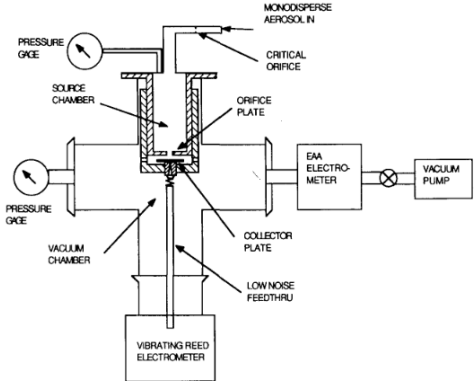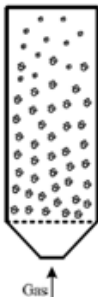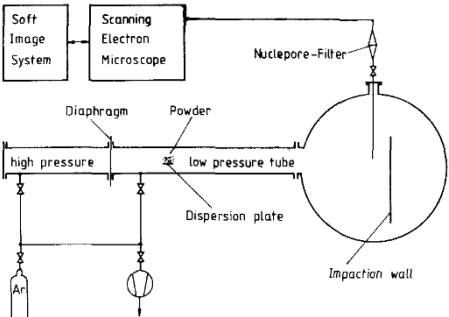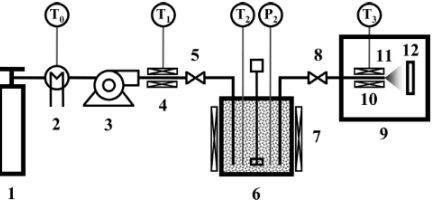
Figure 2.18 Schematic of an impactor designed by de la Mora [95]

All the breakup methods and particles which have been studied are summarized in Table 2.

Table 2.2 A summary of methods and materials for breakup of solid NPs in gas phase

Technique	Mechanism	Material (Ref.)
Nozzle	• Acceleration and/or shear flow • Collisions with other particle clusters and device walls	SiO_2 2.5 µm, borosilicate glass 138 µm (Kurkela, Brown et al. 2008); coal dust aerosol (Davies, C. N., Aylward, M., & Leacy, D., 1951)
Orifice	• Acceleration and/or shear flow • Impaction on the orifice plate	fly ash ~5 um (Yuu and Oda 1983); CeO_2 (PPs 14, 70 nm); TiO_2 (PPs 27, 42 nm); TiZrAlO (26 nm); $SrCO_3$ (17 nm) (Stahlmecke, Wagener et al. 2009); TiO_2 27 nm (Ihalainen, Lind et al.

Technique	Mechanism	Material (Ref.)
		2013); TiO_2 and copper particles (Ihalainen, Lind et al. 2012); (Yuu and Oda 1983, Stahlmecke, Wagener et al. 2009)
 Mixer-type	• Acceleration and/or shear flow • Impaction impeller blades	metallic silicon and calcium carbonate (Iinoya and Masuda 1980)
 Impactor	• Acceleration and/or shear flow through the nozzle • Impaction on the stationary plate	TiO_2 95 nm, Ni 4 nm, Ag 3-8 nm (Froeschke, Kohler et al. 2003); Ni 12-28 nm, Pt 8-24 nm, Ag 6-8 nm (Seipenbusch, Toneva et al. 2007); Ag 10 and 60 nm (Rennecke and Weber 2013); Pd 4.7 nm, Ag .8.6 nm, Ni 8 nm (Guo, Wagner et al. 2015); Pharmaceutical powder (Adi, Adi et al. 2013, Kwek, Heng et al. 2013); ; latex ranging from 1.62 to 4.07 μm (John and Sethi 1993); Numerical modeling de-agglomeration by impaction (Tong, Adi et al. 2011); BSA 1 μm with different roughness amounts (Adi, Adi et al. 2013); Model for impact velocity (Rennecke and Weber 2013);

Technique	Mechanism	Material (Ref.)
 Fluidized bed	• Acceleration from the fluidizing air • Impaction between the powder and the dispersing aids	(Francis, Kreider et al. 2010, Sosnowski, Giżyńska et al. 2014)
 Shockwave - Impaction	• Shear flow as result of turbulency • Impaction on the stationary plate	(Brandt, Rajathurai et al. 1987, Strecker and Roth 1992, Rajathurai, Roth et al. 2007)
Free Falling Nanopowders equipped vibrated rotating beaker	• Acceleration from the gravity force • Vibration and particle-particle collision	TiO_2 5-10 nm; SiO_2 12 nm (Ibaseta, Climent et al. 2008)
 Rapid Expansion of Supercritical Suspensions (RESS)	• Shear flow as result of rapid expansion • Impaction as the powder enters the capillary tube	commercially MWCNT (Quigley, Herrington et al. 2014); alumina and silica nanopowders 13, 21 nm (To, Dave et al. 2009); silica 108 nm (Ghosh, Deguchi et al. 2007); SiO_2 1.4 μm, TiO_2 70 nm (Kongsombut, Tsutsumi et al. 2009)

2.6 Reduction of interparticle attraction force

The reduction of interparticle attraction can be beneficial for dispersion of nanopowders as well as preventing particles from re-agglomeratng. Techniques include powder coating [29, 104-106], spacer or glidant particles [107] or the addition of secondary material [108].

An area where aerodynamic dispersion is highly important is in therapeutic drug delivery via the lungs using dry powder inhalers (DPIs). Dry powder inhaler (DPI) formulations usually contain an excipient with a common powder being fine lactose. It has been shown that an increase in dispersion is possible when lactose is added to a DPI formulation, due to lactose having a lower interparticle attraction [109]. The ability to improve powder dispersibility without additional material but by increasing surface roughness has also been investigated [108]. Asperities reduce particle contact area therefore reducing cohesion/adhesion. The advantage of these methods is that the choice of inhaler and required entrainment flow rate are less critical.

Spacer or glidant particles are also used in industry to improve the flow properties of powders. Tedeschi et al. [110] reported improved dispersion performance of 15–45 nm thin aluminium flakes when mixed with fumed silica. The addition of the fumed silica increased the interparticle spacing, thus reducing the van der Waals forces between the flakes. The silica was shown to have maximum effectiveness at 4 wt%.

Also, adding ternary components to dry powder aerosols has been analysed. Louey et al [111] showed that fine particle fractions (FPF) from ternary mixtures is dependent on carrier type, ternary concentration, and ternary component type. Excluding experiments containing superfine powder, ternary mixtures were able to produce higher FPF than binary mixtures.

Masuda and Gotoh [87] studied the effect of treating powders with ethanol vapour and used a re-entrainment test. This test can evaluate the rupture phenomenon of aggregated particles caused by the flow of a gas over a powder bed. After 12 hours treating with ethanol vapor, the cohesion of particles significantly decreased and dispersion performance slightly increased. Although the technique is simple, treating powders with ethanol vapour can be time consuming and powders can re-agglomerate when again exposed to air.

Beside these methods, more engineering approaches have been presented in the literature in order to reduce interparticle forces of powders such as aerogel powders, needle crystals, and spray-freeze dried-particles. However, most of these methods are not as efficient for dispersion of nanopowders as coating methods [48]. Particle coatings can be used to reduce the Hamaker constant and consequently reduce van der Waals attraction between particles. In fact, to overcome phase separation and re-agglomeration of NPs, their surface energy should be reduced by surface

passivation, steric repulsion or surface functionalization. Beyond the benefit to prevent agglomeration, surface modification of inorganic NPs improves integration and the interface between NPs and polymer matrices in nanocomposites applications [112]. Because of the variety and importance of particle coating methods, these techniques will be discussed in detail under three main classes: batch, semi-continuous, and continuous treatment processes.

2.6.1 Batch Processes

Conventionally, NPs are synthesized and coated batch-wise, in the liquid phase, through several processes such as nanoprecipitation [113, 114], sol–gel [115-117], ultrasonic [118, 119], micro emulsion [120, 121] and reduction methods [122, 123] exploiting well-known synthetic mechanisms. The processing of NPs, either organic or inorganic, typically consists of three stages: 1) nucleation, 2) growth, and 3) separation. During a batch synthesis, these three stages inevitably occur at the same time, which makes it difficult to control the size of the final product. To overcome this issue, surfactants are usually used. Surface modification by adsorption of polymeric dispersants is one of the simplest methods to improve the dispersion behavior of NPs in aqueous systems. Hydrophilic NPs can be dispersed in highly nonpolar organic solvents by using anionic or cationic polymer dispersants. These dispersants generate steric repulsive forces among the polymer chains and increase the surface charge, which results in better dispersibility of the NPs. For example, for anionic surfactants, various types of polycarboxylic acids and their salts have been used to disperse many types of oxide NPs, such as TiO_2, Al_2O_3, and Fe_2O_3 [124-126]. The capping agents or surfactants, such as trioctylphosphine oxides (TOPO), oleic acid and amines, are dissolved during synthesis or dispersed in solution using methods such as ultrasonication to prevent the agglomeration of NPs. Although surfactants are generally effective in dispersing NPs, there is still a huge challenge in controlling size distribution of final NPs. This stem from the lack of control of mixing and separation during particle growth from agglomeration processes, which results in a high batch-to-batch variation in both size and size distribution of NPs. Further, up-scaling a batch synthesis will add more difficulties by aggravating mixing and mass transfer problems, which leads to a polydispersed population of NPs having various physical and chemical characteristics [127, 128]. Also, surfactants, as disperser agents, suffer from thermal instability which limits their applicability in many applications such as nanofluids, nanocomposites and thermoset polymers. It

was reported that many surfactants detached from the surface of the NPs at 70 °C [129]. More importantly, the post-treatment operations such as drying leads to severe re-agglomeration of NPs induced by capillary pressure or surface tension [130].

2.6.2 Semi-batch Processes

When it comes to processing powders, fluidized beds are a widespread technique characterized by excellent gas-solid contact, uniformity of heat and mass transfer across the bed, the ability to handle a wide variety of particles, and suitability for large scale operations. Fluidized bed technology applied to coating is used in numerous industries such as chemical processing, agriculture, food, pharmaceutical and cosmetic industries [131]. Fluidization, also, plays an important role in both the production [132, 133] and coating of NPs [29, 105, 134].

Fluidized beds have been combined with other gas phase coating methods such as TACVD (thermally-activated CVD) [134], PECVD (plasma-enhanced CVD) [135], PICVD (photo-initiated CVD) [29], ALD (atomic layer deposition) [136], microwave-assisted coating [137], and polymerization compounding [105]. Merging such mature techniques, typically referred to as fluidized bed chemical vapor deposition (FBCVD), leads to a flexible and cost-effective powder treatment process. Effective contact between the gaseous reactant(s) and the solid particles to be treated is the strength of FBCVD. The first use of FBCVD dates back to 1960 for nuclear applications; however, its application in other fields essentially began to grow since 1990 [138] and it continued for coating nanopowders thus far. Habibzadeh and Chaouki [134] reported a conformal multilayer $TiO_2/SiO_2/TiO_2$ coating deposited on the surface of a micron size soda lime glass particles using FBCVD. The reaction occurred under atmospheric pressure and high temperatures (300 °C) as the titania precursor requires high temperature to be vaporized, which limits its application for heat-sensitive materials. Van Ommen et al. [135] coated copper oxide powders (CuO, 20-30 µm) using a PECVD process in a fluidized bed and studied the interaction between the plasma and the fluidized bed hydrodynamics. They observed that adding hexamethyldisiloxane (HMDSO) to a plasma, with and without oxygen present in the carrier gas, changes the composition of the coated polymeric film from organic polydimethylsiloxane-like coatings to inorganic quartz-like deposits, respectively. However, both coatings change the wettability of the CuO powder from hydrophilic to hydrophobic behavior. Although, unlike

TACVD, a non-thermal PECVD process allows treating heat-sensitive materials, it suffers the fact that it needs to operate at very low pressures, high energy consumption, and complex reactor design for generation of plasma. In another example of FBCVD, Farhanian and Tavares [29] presented the combination of PICVD and jet-assisted fluidized bed as a scalable process to coat magnetic iron oxide NPs (MIONP, 20-30 nm). Using syngas as the precursor, they encapsulated MIONPs with a nanometric carbon film consisting mainly of aliphatic hydrocarbons that enhanced dispersibility of MIONP in non-polar solvent. While this FB-PICVD technique has advantages such as operating under normal condition and relatively low scaling costs, coating NP agglomerates is still its drawback. Hakim et al [136] modified the surface of silica and zirconia NPs (in the size range of 7-40 nm) via FB-ALD technique, and studied the fluidization behavior of uncoated and coated NPs as well as the dynamic behavior of agglomerates during fluidization. Zirconia and silica NPs were conformally coated, but in the form of multiple-level structures (i.e. complex agglomerates) due to multiple interparticle forces. They also showed that coating NPs reduces their minimum fluidization velocities, allowing for higher bed expansions, by decreasing the particle-to-particle interactions. The image of fluidized nanopowders (Figure 2.19), shows that the agglomerates are fluidized in micron-size, with a sphericity of about 0.5, and loosely packed structures. Due to the relatively large size of the fluidizing agglomerates and the frequent collisions with other agglomerates within fluidized bed, they investigated the agglomeration behavior by coloring Aerosil OX-50 silica NPs in red, green and white. The powders, without prior mixing, were fluidized together for 1 h under mechanical vibration, and a sample of the resulting powder was analyzed under a light microscope (Figure 2.19 b). They observed agglomerates contain all three colors, indicating that the initial agglomerates broke apart and reformed into new complex agglomerates. This is a qualitative evidence of the dynamic agglomeration of pre-existing NP agglomerates during fluidization. However, they [136] did not report the scale of the mixing.
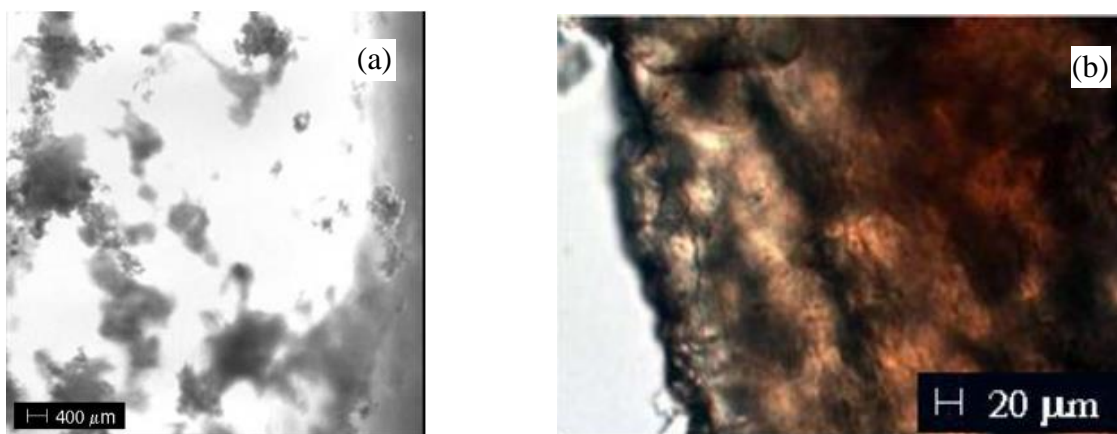
Figure 2.19 (a) Image of fluidized agglomerates of silica NPs with primary particle size of 7 nm, and (b) microscopic image of Aerosil OX-50 silica NP agglomerates consisting different colors, indicating a dynamic agglomeration [136].

Esmaeili et al. [105] used a fluidized bed to encapsulate zirconia and alumina NPs by polymerization compounding using Ziegler–Natta catalysts. They were able to control the thickness of coating (i.e. rate of polymerization) by adjusting the operating conditions such as pressure and temperature. Further, compared to the batch processes in liquid phase, this solvent-free process simplifies the coating by reducing the time and costs associated with filtering and drying liquid coatings. However, further electron microscopy analysis revealed that zirconia NPs tend to be coated in an agglomerated state. They compared the size of coated agglomerates in their fluidized bed and a slurry phase reactor, and showed the size of agglomerates in the slurry phase is smaller [105].

2.6.3 Continuous processes

While several semi-batch methods have been developed in the gas phase, few continuous processes are available [139-145]:

- Wang et al. [139] used supercritical CO_2 as a solvent-free technique to physically encapsulate silica NPs with Eudragit (polymethacrylate-based copolymers). Flashing the NP-polymer-supercritical CO_2 suspension from 32 °C and 8.27 MPa to ambient

temperature and atmospheric pressure causes a heterogeneous polymer nucleation with the NPs acting as nuclei and a subsequent growth of polymer on the surface of the NPs.

- Poostforooshan et al. [140] achieved a carbon shell coating using aerosol polymerization via heterogenous condensation of both monomer and initiator on the surface of NPs.

- Pfeiffer et al. [141] coated metal NPs using a continuous PVD system. In this technique, an aerosol of freshly generated core particles was passed through a metal vapor cloud, formed by spark ablation, followed by a quick quench. This causes a metal shell to quickly condense around the core particle and form a core-shell NP.

- Tavares et al [142, 143] synthesized copper NPs and functionalized their surfaces in-flight with hydrophilic and hydrophobic groups in a dual plasma process.

- Munzer et al [144] synthesized silica NPs using plasma, which were then coated via decomposition of an organic precursor (e.g. ethylene) on the surface in the afterglow heat of the plasma.

- Zhang et al [145] used photo-initiated chemical vapor deposition technique to physically coat aerosolized NaCl NPs with different organic films.

Although these techniques serve as examples that solvent-free techniques can be applied for continuous, in-line processing of NPs, they suffer from the use toxic materials, extreme operating conditions, complex infrastructure requirements, and high scaling costs.

2.7 Measuring solid concentration in fluidized beds

Solid concentration or solid hold up is one of the hydrodynamic parameters of fluidized beds that demonstrates the distribution of emulsion (dense) phase versus bubble phase in time or space domain. Solid distribution in a fluidized bed varies by varying the fluidization velocity, addition of secondary streams or physical barriers in the system. For example, a bubbling regime is characterized by continuous dense phase and dispersed bubbles while by increasing the superficial velocity up to turbulent regime, the bubble concentration significantly increases so that elongated and irregular voids are observed along with violently moving particle strands. Knowledge of solid concentration is crucial in designing, optimizing and scaling up of such systems. Further, solid concentration is an important parameter to better understand the agglomeration, de-agglomeration, and re-agglomeration mechanisms in the dense zone, jet zone, and dilute zone. Indeed, increasing

the particle concentration (number of particles) in the jet zone can be a sign of de-agglomeration. In parallel, it increases the probability of re-agglomeration of particles after the impaction zone due to particle-particle or cluster-cluster collisions. There are several invasive and non-invasive techniques for measuring solid concentration in fluidized beds. Some of the common techniques are explained further in below.

2.7.1 Direct visualization

Direct visualization and video recording are the most straight forward qualitative methods for studying solid distribution. Video recording facilitates observing very fast phenomena to the eye (e.g. the size, shape, and velocity, and frequency of bubbles) using the slow-motion mode. Several studies have been reported studying solid distribution or bubble velocity using high-speed cameras and image processing [146-149]. However, as a result of opaque nature of most powders, this is limited to the transparent systems such as glass or Plexiglass columns.

2.7.2 Pressure measurements

Pressure measurements are simple and cheap methods to measure the solid distribution. This is the only method that is widely used at the lab scale as well as in industrial units. Measuring pressure differences Δp between two vertical positions with spacing h provides an estimation of average bulk density between these two points: $\rho_{bulk} = \Delta p/(hg)$, which can be translated as local average solid concentration. This value is calculated based on a time-averaged pressure measurement. In a time-resolved or dynamic pressure measurement, when the pressure is measured at sufficiently high frequency (more than frequency of bubbles), the pressure fluctuations signal can provide more information about the bubbles and consequently the solids. The time-resolved measurement can use a single-point absolute measurement or differential pressure between two vertical positions in the bed. In this case, the calculated solid distribution reflects the local hydrodynamic behavior at that single point or between two points. Dimensions of the pressure transducer probe, free entrance of the probe, signal filtering, proper placement of the probe, and total recording time are important parameters that should be taken into account to obtain reliable results [150].

2.7.3 Optical probe

Optical probes are fine probes that consist of sender and receiver optics (e.g. optical fiber). Visible light is sent through the sender fiber into the bed and the reflections are recorded. According to the pre-calibration, the received signal can demonstrate the concentration of solid particles that crossed the measuring volume in the bed. The optical probes can work in reflection or transmission mode. Further, many researches (see, e.g. [151]) have been used two receiving fibers for measuring velocity of particles by finding the time of flight of particles from one receiver to another and cross correlating their signals. The limitations of using optical fibers are the lack of properly defined measuring volume and becoming unusable for cohesive powders due to significant reduction of signals. The latter becomes more important in case of group C particles and specifically nanoparticles [152].

2.7.4 Capacitance probe

Capacitance probes uses the dielectric permittivity of the bed material to quantify the concentration of solid particles in the gas-solid mixture. In this invasive technique, two parallel flat plates, as capacitance probes, are placed in the bed so that the spacing of the electrodes is typically in the order of millimeters. The capacitance of the plates as a function of time can be translated to time-resolved solid concentrations. This becomes possible through calibration of a given probe in the pure gas phase and in the fixed bed or minimum fluidization. Although this measurement technique is easy to perform and interpret, like other invasive techniques, it suffers from interfering the natural flow inside the fluidized bed.

2.7.5 Electric capacitance tomography (ECT)

Like capacitance probe, ECT works based on the dielectric permittivity of gas-solid mixture. This technique takes advantages of significant difference between dielectric constant of gases and solids. Since most solid particles used in fluidized beds are dielectric materials, meaning they tend to concentrate electric field within themselves, this technique can be widely used in fluidized beds. In this technique, multiple electrodes (typically between 8 to 12) are arranged around the column and all electrode capacitances are fired one by one and the signal obtained from each is measured. An N-electrode system can only provide $N(N-1)/2$ independent measurements. These signals,

using calibration curves obtained from measuring in the pure gas and fixed bed of solid particles, then can be translated to the distribution of sloid particles. Further, implementing linear reconstruction principles allows mapping gas/solid distribution in the bed. While ECT allows measurement time-resolution as high as 1000 frame/sec, poor spatial resolution limits its usage.

2.7.6 X-ray and gamma-ray tomography

This class of non-invasive measurement techniques uses high-energy photons that travels through the bed of gas-sold mixture. The solid concentration, according to Beer-Lambert low: $\frac{I(x)}{I_0} = \exp(-\mu x)$, can be calculated by measuring the attenuation of the photon intensity. Unlike the probe measurements that measuring volume is very small (close to the probe tip), these tomography techniques provide line-averaged solid concentrations. By measuring over multiple independent lines, enough information can be recorded for either mapping the solid concentration or tomographic map of the column. Also, the random nature of nuclear photons creates inherent noise in the counted photons (N). This introduces errors in the calculation which diminishes with the rate of $1/\sqrt{N}$. This implies the measurement time cannot be chosen short without using excessively strong and long-life sources. Therefore, this class of measurements provide solid concentration profile in time-averaged base as well as line-average. Due to the high-energy photons, they can easily travel through any systems. This makes them suitable for measuring very concentrated or very large systems. Further, as a non-invasive technique they can measure solid distribution in the region of interest without disturbing or distorting the flow fields. These advantages make them suitable to be used for measuring solid concentration in fluidization of nanopowders.

CHAPTER 3   OBJECTIVES AND ORGANIZATION OF THE ARTICLES

According to the literature review, nanoparticles (NPs) naturally tend to form agglomerates, and if those are not stabilized by treating their surfaces, it causes heterogeneity of processed nanopowder, meaning variation of particle size distribution from batch to batch, which then propagates through commercial products. Among the techniques for breaking up agglomerates, impactors seem to be an efficient technique that can controllably break up nanoparticle agglomerates. Form the other side, assisted fluidized beds (FBs), as simple scalable techniques, have a high potential for processing powders. Even though several studies have combined FB with other gas phase coating techniques (e.g. chemical vapor deposition techniques) to coat nanopowders, referred to as FBCVD techniques, at the end all process showed an inhomogeneity in the size distribution of final product. This happens because nanopowders form multi-level structures complex agglomerates during fluidization due to random collisions within the bed. Further, although coating nanopowders via FBCVD show a reduced minimum fluidization velocity and higher expansion, indicating reduction of interparticle forces, fluidized coated particles are still in the form of huge fractal-shape agglomerates. This occurs due to the fact that NPs are fluidized in the agglomerate form as a result of high ratio of interparticle forces to hydrodynamic forces (i.e. gravity and drag). Due to the dynamic agglomeration re-agglomeration occurs in the batch and semi-batch processes, a controllable de-agglomeration would not be inherently possible in those types of processes. This affirms nanopowders are required to be de-agglomerated before coating, as two separate steps. However, this has not been thoroughly addressed in the literature. The two-step continuous technique requires developing a continuous coating technique. Available continuous solvent-free techniques suffer from the use toxic materials, extreme operating conditions, complex infrastructure requirements, and high scaling costs. It demands developing a simple online coating approach that can quickly coat nanoparticles after de-agglomeration before those re-agglomerate. Among coating technique presented in the literature review, the PICVD technique has a high potential due to the fact that it operates at ambient temperature and atmospheric pressure and has low scaling costs.

The growing use of NPs and engineered nanomaterials implicates developing novel techniques for producing stable NPs with more homogeneity in properties. Hence, this thesis aims to develop a

novel scalable combined approach for producing stable coated NPs from supplied agglomerated metal oxide nanopowders. This project is the first study on de-agglomerating NP agglomerates along with coating them continuously in the gas phase to improve homogeneity in processing of nanopowders.

3.1 Objectives

3.1.1 General Objective

The main objective of this research is to develop a scalable combined technique for producing stable de-agglomerated NPs from agglomerated metal oxide nanopowders.

3.1.2 Specific Objectives

To achieve the general objective, the following specific objectives are outlined:

1) To design and construct a continuous controllable technique for de-agglomerating NP agglomerates in a fluidized bed, using a jet-impactor configuration;

2) To link the solid phase distribution in the jet-impactor fluidized bed with the kinetic energy of impaction to formulate an operating window

3) To develop a continuous coating technique to be combined with de-agglomeration process and investigate the physico-chemical properties of treated particles

3.2 Organization of The Articles

To satisfy the specific objectives, outcomes of this research are presented in three scientific journal articles. Chapters 4 to 6 provide the main results of this thesis and corresponding scientific findings. A brief description of each chapter and the link between them is provided below:

Chapter 4 describes the first article of this thesis entitled: "De-agglomeration of NPs in a jet impactor-assisted fluidized bed". This work was presented at the Fluidization XV conference in Montebello, Québec, Canada in May 2016 and was published in Powder Technology in 2017, Vol. 316, p. 455-461 (special issue on Fluidization for Emerging Green Technologies). In this article, we present a novel technique, called the "Jet-Impactor assisted fluidized bed (JIAFB)", for de-

agglomerating fluidized NPs directly within a fluidized bed. The JIAFB consists of a micro-jet and an impaction plate that are placed inside the bed, as well as an air-driven venturi pump installed on the outlet of the column. The JIAFB uses a high-speed jet to accelerate the fluidized agglomerates onto the impaction plate, while the venturi pump entrains the broken particles out of the bed to a particle sizer. To demonstrate the process, we study de-agglomeration of dry silica nanopowder. In order to ascertain the jet length and that the kinetic energy of particles is sufficient for de-agglomeration, a CFD simulation was carried out using ANSYS Fluent 6.3. In addition, to study the de-agglomeration process, a Scanning Mobility Particle Sizer (SMPS, online) and a Transmission Electron Microscope (TEM, offline) were used to measure the particle sizes. Mr. Jean Huard helped with designing, ordering parts and building the JIAFB. Mr. Amir Modarreszadeh helped me with building and meshing the geometry in the Gambit software and technical guides on modeling. Also, Dr. Vincent Darras trained me with the SMPS instrument. I was responsible for the simulation, data analysis, designing and building the JIAFB, experimental works, interpretation of the experimental results and writing the article.

Chapter 5 presents the second article of this study entitled: "*Solid Hold-Up Measurement in a Jet-Impactor Assisted Fluidized Bed Using Gamma-ray Densitometry*". This manuscript has been submitted to *AIChE Journal*. In this article, we study and compare the fluidization of NPs in three configurations: conventional, jet-assisted, and jet-impactor assisted fluidized bed to provide a better insight on the gas-solid dynamics resulting from the introduction of the jet and impactor. This study is essential to optimize the de-agglomeration process by determining the impactor-to-jet distance at which the NP agglomerates have maximum momentum. For this purpose, the solid hold-up of NPs in the jet stream was measured using an improved gamma-ray densitometry technique. The velocity of NP agglomerates in the jet stream was calculated using a two-phase CFD simulation. Maximum momentum occurs where the multiplication of those profiles is maximized. These findings serve to define an operating window and guide selection of the impactor-to-jet distance that will be necessary for scale-up. Mr. Amir Modarreszadeh helped me with two-phase simulation and particle study in Fluent. Also, Dr. Majid Rasouli trained me with on the gamma-ray densitometry technique. I was responsible for the simulation, data analysis, experimental works, interpretation of the experimental results and writing the article.

Chapter 6 is the third article of this research entitled: "*Continuous Aerosol Photopolymerization to Coat De-agglomerated Nanoparticles*". This manuscript has been submitted to *Chemical Engineering Journal*. In this section, we combine the JIAFB system with a novel simple technique to continuously coat de-agglomerated NPs in-flight. After de-agglomeration in the JIAFB, monomer vapors are condensed onto the surface of aerosol NPs via heterogeneous condensation. Photopolymerization is initiated through exposure to UVC light. To demonstrate the process, titanium dioxide (TiO_2) and methyl methacrylate (MMA) were selected as NP and organic monomer, respectively. In the first part of this paper, we demonstrated this light-based technique, is able to graft an MMA oligomeric film on the surface of NPs. In the second part, we evaluate the de-agglomeration process and coating efficiency by measuring particle size in suspension state and the suspension stability, respectively. Mr. Sylvain Simard Fleury and Mr. Yanik Landry-Ducharme helped with construction of the setup and Mr. Jean-Philippe Masse assisted in microscopic characterization. I was responsible for designing and building the setup, experimental works, sampling and characterizing, interpretation of the experimental results and writing the article.

In all cases, co-authors J.R. Tavares and J. Chaouki reviewed the manuscripts thoroughly and supervised the work.

CHAPTER 4   ARTICLE 1: DE-AGGLOMERATION OF NANOPARTICLES IN A JET IMPACTOR-ASSISTED FLUIDIZED BED

Hamed Nasri Lari, Jamal Chaouki, Jason R. Tavares

Department of Chemical Engineering, École Polytechnique de Montréal, P.O. Box 6079, Station Centre-Ville, Montreal, Quebec, H3C 3A7, Canada

KEYWORDS:

Fluidized bed, NPs, De-agglomeration, Impaction, Particle size distribution, Interparticle forces

Abstract

NPs in agglomerated state lose their outstanding properties; hence, it is essential to break them up prior to use and prevent their re-agglomeration. Even though there are several dry techniques to disperse nanopowders, none of them have been able to produce truly nanoscale aerosols so far. Here, we study de-agglomeration of dry silica nanopowder via a jet impactor-assisted fluidized bed (JIAFB). The particle size distribution of fragmented powders was characterized by in-line scanning mobility particle spectrometry (SMPS) and offline transmission electron microscopy (TEM). In order to ascertain the jet length and that the kinetic energy of particles is sufficient for de-agglomeration, a CFD simulation was carried out. Both SMPS and TEM measurements imply that at a certain fluidization velocity, increasing the jet velocity shifts the particle size distribution towards smaller diameters, and at higher velocities the mode value reduced from 113 130 to 55–60 nm. However, the geometric standard deviation or degree of polydispersity rises from 1.5 to 2.0 by increasing the jet velocity up to 197 m/s, as it will increase the total superficial velocity and consequently entrainment of larger particles from the bed. In addition, the TEM results indicate that the range of individual particle sizes in the supplied nanopowder is wide; hence, increasing the geometric standard deviation can be an indicator of a higher level of agglomerate dispersion.

4.1 Introduction

Nanoparticles, due to their high surface area-to-volume ratio and free atoms on their surfaces, have a tendency to assemble together as well as absorb a wide range of molecules such as water, oxygen, etc. In other words, these features will lead the particles to have high surface energy, become unstable and be very cohesive. Therefore, individual nanoparticles, in order to reach a lower energy state, attract each other and form assemblages under the influence of some external and internal interparticle forces such as van der Waals, electrostatic, and capillary forces [1]. These friable and readily dispersed assemblages of particles are called agglomerates or "soft" agglomerates and can be formed during production, transportation or storage as a result of Brownian motion, collisions, and pressure arising from stacking. In this form, particles lose the extraordinary surface-driven properties they had as individual nanoparticles. In order to take advantage of their "nanoproperties", it is necessary to break up the agglomerates and reduce their high surface energy,

or "passivate" them, before use. The ability to produce bulk quantities of highly dispersed nanoparticles is a significant limitation of nanotechnology [2].

De-agglomeration of nanopowder can be performed in the gas [3-11] or liquid phase [12-17], and a variety of theoretical and experimental studies have been conducted (Table 1). Various techniques have been developed to disperse nanoparticles in fluids, typically through use of mechanical and acoustic energy. Ultrasonication is a well-known technique to disperse nanoparticles homogeneously in suspensions using acoustic energy. Through acoustic cavitation and streaming, the formation, growth and implosion of bubbles occur, resulting in the rupture of agglomerates. Time, power and irradiation modes (continuous or pulsed) are the key parameters affecting dispersion quality in an ultrasonic bath. Nguyen et al. [16] showed that there is an optimum power input in ultrasonication: past a certain point, a higher vibration amplitude will not improve dispersion quality, but will actually increase the re-agglomeration rate. High-speed revolution shearing, milling [14], and high-pressure homogenizers [13] are the main mechanical dispersion approaches. In milling, dispersed nanoparticles are introduced from the bottom of the mill in a slurry. Agglomerates are broken by passing through the stirrer, impinging the beads, and being stirred by rotating pins. In the upper part of the mill, the beads and slurry are separated by centrifugation and the dispersed-particle containing slurry is discharged. Similar to sonication, Inkyo et al. [14] also indicated that there is an optimum time for milling, after which re-agglomeration occurs.

Table 4.1 Comparison of different NP dispersion methods in liquid and gas phase

Techniques	Mechanism of Dispersion	Advantages	Disadvantages	References
Ultrasonication	Acoustic cavitation	Simplicity. Applicable for a wide range of NPs. Efficient for high particle concentration. Wide range of liquid viscosities. Possibility to control more parameters	Re-agglomeration problem. Contamination of NPs, additives required (thermal stability issues). Downstream separation problem	[12] and [16]

Techniques	Mechanism of Dispersion	Advantages	Disadvantages	References
		(amplitude, irradiation mode, pressure, temperature, viscosity, and concentration)		
Bead milling	Friction and shear flow	Applicable for a wide range of NPs. Multi-pass and continuous. Scalable	Complex design. High energy input. High polydispersity. Damaging to particle structure. Additives required (thermal stability issues). Addition of impurities to NPs	[14] and [15]
High-pressure homogenizer		Well established technology. Effective dispersion. Suitable for thermos-sensitive material Reproducible. Scalable.	Extremely high energy inputs. High polydispersity	[13] and [17]
Nozzle and orifice	Shear flow and collisions with other particle, clusters, and walls	Controllable. Low cost and energy. Continuous. Scalable	Not able to produce sub-100 nm particles. Re-agglomeration issues	[7-9]
Low pressure impactors	Shear flow through the nozzle and impaction	Well established. Ability to produce monodisperse powders. Low cost and energy. Continuous	Complex design. Extremely low pressures. Re-agglomeration issues	[4] and [10]
Fluidized bed	Acceleration and impaction between the	Well established. Possibility of pre-	Low dispersion energy.	[5] and [6]

Techniques	Mechanism of Dispersion	Advantages	Disadvantages	References
	powder that causes attrition	and post-treatment *in situ.* Scalable	Difficult to produce sub-100 nm particles. Re-agglomeration issues	
Rapid Expansion of Supercritical Suspensions (RESS)	Shear flow as result of rapid expansion and impaction as the powder enters the capillary tube	Possibility of pre- and post-treatment (e.g. ultrasonication and encapsulation). Benign de-agglomeration. Suitable for non-spherical NPs (e.g. carbon nanotubes)	Difficult to control. Extremely high pressures (supercritical fluids).	[3] and [11]

While liquid phase techniques are generally effective at dispersing nanoparticles, they do not directly address the issue of re-agglomeration. To stabilize the suspension, additives must be supplied to provided electrostatic, steric and electrosteric repulsion effects. Surfactants are commonly used for this purpose, resulting in electrostatic repulsion between surfactant-coated nanoparticles [18] and reducing particle agglomeration caused by attractive van der Waals forces [19]. However, surfactants face several limitations, not the least of which is their thermal instability: surfactants can desorb from nanomaterials at relatively low temperatures (65–70 °C) [20], cancelling out their repulsive properties.

Gas phase methods have several advantages over liquid-phase approaches, such as the absence of solvent waste, the simplification of downstream separation, the feasibility of continuous processing, and the versatility with respect to particle material and size and structure [21]. The de-agglomeration of nanoparticles down to their constituent primary particles in the gas phase can be achieved by applying an external force larger than the interparticle forces. There are several methods to de-agglomerate nanoparticle clusters in the gas phase ranging from high energy (e.g. rapid expansion of supercritical suspensions [3] or low pressure single stage impactors [4]) to low energy (e.g. fluidized bed [5]). However, so far, the low energy methods have not been able to produce sub-100 nm particle sizes, and the high energy methods have significant scale-up issues

because of their operating conditions. Indeed, the rapid expansion of supercritical suspension systems requires high pressures (1.9–7.9 MPa). Nurkiewicz et al. [6] presented a nanoparticle aerosol generator consisting of a vibrating fluidized bed with a baffle, a vibrating Venturi disperser and a cyclone separator. Although they discussed the de-agglomeration of nanopowders and preventing re-agglomeration (strictly through dilution), the investigation was mostly focused on generating nanoparticle aerosols at constant particle concentration over time to perform inhalation studies, limiting the scale-up potential. In order to break agglomerates in a controllable and scalable manner, further investigation is necessary, namely on interparticle forces and attaining the required de-agglomeration energy in a fluidized bed configuration.

In this work, we break the large fractal-shaped agglomerates of silica nanoparticles to smaller clusters continuously through use of a jet impactor-assisted fluidized bed (JIAFB). The force required to destroy the agglomerates is controlled by the gas jet velocity in the impaction zone. Calculating the impaction velocity determines the kinetic energy of particles upon impaction, making it possible to measure the theoretical fragmentation degree of nanoparticles. As agglomeration is a reversible phenomenon, in order to produce stable particles, reducing interparticle attraction and preventing the nanoparticles from re-agglomeration are inevitable. Therefore, following agglomerate destruction, the JIAFB includes a surface functionalization post-treatment, based on photo-initiated chemical vapor deposition (PICVD) [22], to ensure particle stability and prevent re-agglomeration (not reported here).

4.2 Experimental

4.2.1 Materials

Silica nanopowder manufactured by TEKNA™, via thermal plasma synthesis, was used for all fluidization experiments. Primary particles have an average diameter of 20 nm. The powder's specific surface area is 200 m^2/g, with a solid density of 2200 kg/m^3, and bulk density of 35 kg/m^3. As nanopowders are a strong absorber of humidity, the particles were dried at 140 °C and $-$ 70 kPa vacuum before any fluidization experiments. Argon was used as fluidizing gas and air was used as jet and diluter gas in all experiments.

4.2.2 Experimental set-up

The JIAFB consists of a jet and an impaction plate that are placed inside the bed, as well as an air-driven venturi pump installed on the outlet of the column (Fig. 4.1.a). The JIAFB uses a high-speed jet to accelerate the fluidized agglomerates onto the impaction plate. The venturi pump provides a vacuum in order to entrain out broken particles, as well as minimize re-agglomeration of dispersed particles by diluting the outlet flow and send it to the particle sizer (dilution ratio of 1:25). The particle size and mass concentration produced by the JIAFB were measured utilizing an in-line scanning mobility particle spectrometer (SMPS), operated in aerosol mode. A calibrated rotameter was used to set the inlet flow rate to the particle sizer. A cylindrical quartz tube was used as the fluidized bed with an internal diameter of 8 mm and a height of 60 cm. After passing through a porous glass wool distributor, argon gas is introduced to the quartz tube. The superficial gas velocity was adjusted using a mass flow controller. A 250-μm jet was installed vertically, upwards, by passing through the distributor. The compressed air flow was supplied for the high speed jet after passing through a mass flow controller. An impaction plate welded to a stainless steel rod was introduced to the fluidized bed from the top. The jet-to-plate distance was set to 5 mm. For transmission electron microscopy (TEM) sampling, four sites were selected on the lateral surface of the rod to attach the TEM grids.

In order to study the effect, if any, of the fluidized bed system on the particle size distribution, the setup was configured in a "bypass" mode (Fig. 4.1.b). In this case, the supplied silica nanopowder container is connected directly to the venturi pump. The connection to the SMPS remained the same, and the same air flow rate used during normal experiments was supplied to the venturi to generate a vacuum.
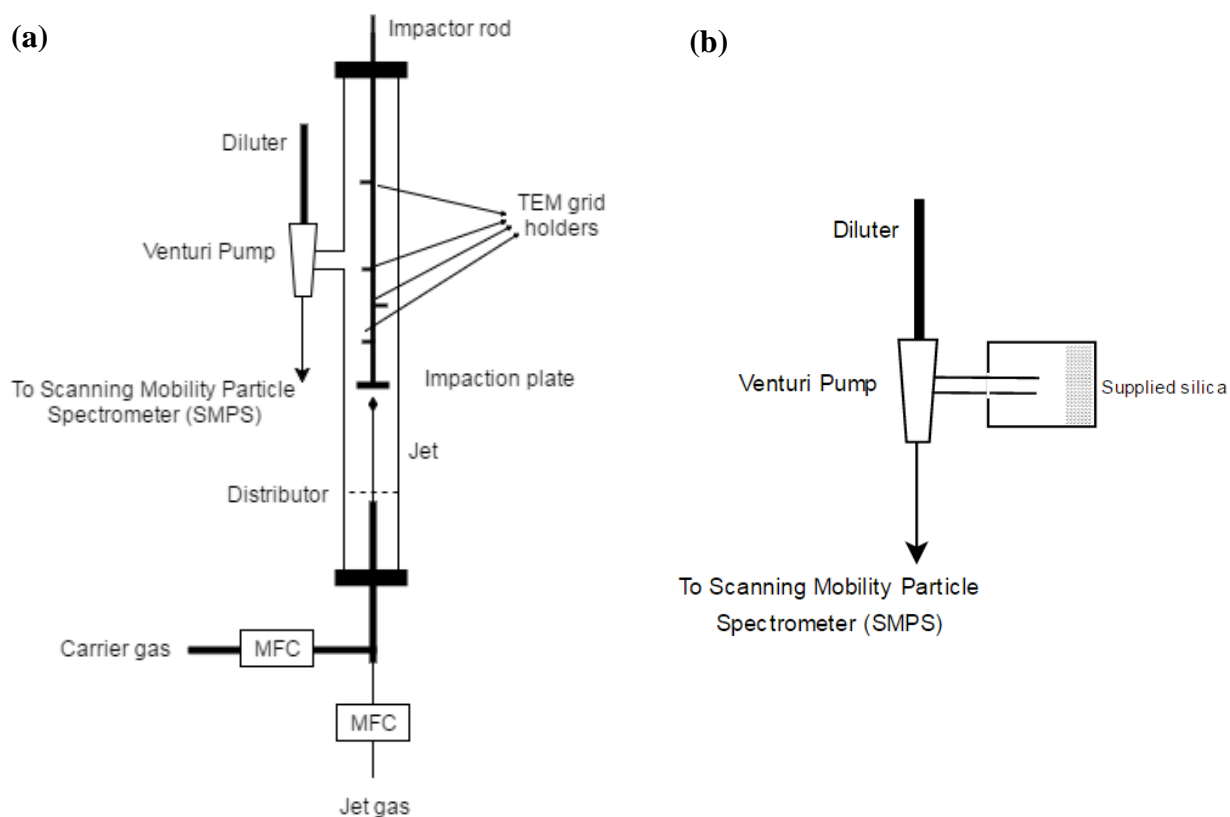
Figure 4.1 Schematic of (a) the JIAFB; (b) bypass configuration.

4.2.3 Measurement methods

A SMPS (TSI Inc., Shoreview, MN, USA) was used to measure the real time number distribution of the particles in the outlet stream of the fluidized bed. TEM was performed on a JEOL JEM-2100F operated at 200 kV in bright-field imaging to confirm the effect of impaction on dispersion. The particles were collected on TEM grids (Electron Microscopy Sciences, CF-400-Cu, carbon film on a 400 square mesh copper grid), directly from the aerosol phase.

4.3 Results and discussions

In order to ascertain that the jet length and applied kinetic energy are sufficient for de-agglomeration, a single-phase computational fluid dynamics (CFD) simulation in the vicinity of

the jet and plate was performed for all jet velocities using the ANSYS Fluent 6.3 CFD software. The two-dimensional axisymmetric case was solved isothermally at constant room temperature and the conservation equations for momentum were solved for a computational domain. The geometry was defined as an 8 mm by 50 cm rectangle. A 250 μm line was defined as the tip of the jet and a rectangular impaction plate (5 mm by 1.5 mm) was place 5 mm from the jet. The geometries of the computational domains were generated and meshed by Gambit 2.4.6, leading to a multi-zone grid structure in which cell sizes ranged from 8×10^{-5} m near the impaction plate to 2×10^{-3} m near the outlet. Downstream from the impaction plate, mesh sizes were stretched away with the length of the cells adjacent to the impactor section. The geometries were meshed with quadrilateral meshes, that, after grid adaption to y-plus to meet the mesh requirement of the near-wall modeling of turbulence, gave a total number of cells of around 8×10^4. Air was selected as a compressible fluid flow medium. The air jet velocity changes from 33 to 197 m/s, while the co-flow velocity outside of the jet is 0.2 m/s. The Reynolds numbers for the jet, based on the outlet velocity and the inner diameter of the jet, lay approximately in the range of 3 to 8×10^3, indicating that the jet is fully turbulent. Hence, k-ε turbulent physics were used for the case of stationary studies. The turbulence intensity was assumed to be 2% for the subsonic jet. The boundary conditions were the fluid inlets for the fluidizing gas (0.2 m/s — $U/U_{mf} = 6.2$) and jet velocity (ranging from 0 to 197 m/s) at x = 0 as well as fluid outlets at x = 50. The other boundaries, including wall column and impaction plate, were considered as a wall. Also, as the velocity field close to the wall (impaction plate) is crucial for turbulence modeling, enhanced wall treatment was selected as the wall function according to the y-plus value. To apply the enhanced wall treatment, a fine mesh that can resolve the viscosity-affected near-wall region was defined. A y-plus value < 5 is considered acceptable, as long as it is well inside the viscous sublayer (FLUENT 6.3 User's Guide). For the worst flow condition (highest jet velocity), y-plus was checked after the solution had converged. When y-plus did not fulfill the requirement, grid adaptation was applied and the solution was processed again. As an example, the resulting velocity field in an axial symmetry view at the maximum jet velocity of 197 m/s is shown in Fig. 4.2. The CFD simulation does not account for the motion of particles, but it serves as a gross approximation to determine the maximum kinetic energy of per unit mass of particles based on the gas velocity field, calculated as half of the near-wall velocity squared (Table 4.2). This near-wall velocity term implicitly accounts for turbulent kinetic energy through an artificial viscous term

(calculated through the RANS k-ε turbulent physics model). At a jet velocity of 197 m/s, the gas velocity at the impactor is on the order of 100 m/s. Froeschke et al. [10] showed that the energy required to break up large fractals (with a fractal dimension of 1.7–2.7) of air-borne metal oxide nanoparticles with primary particle sizes on the order of 6 to 95 nm lay in the range of 1 to 10×10^3 m^2/s^2. For instance, in their experiments, titania agglomerates could be almost completely fragmented at a kinetic energy per unit mass of particles corresponding to $8 \times 10^3 \, m^2/s^2$. Comparing the amount of kinetic energy provided for fragmentation in the present study with their numbers demonstrates that impaction velocities > 48 m/s lay within the acceptable range to provide the kinetic energy to break-up the agglomerates into smaller clusters. The agglomerates can further be fragmented to their constituent nanoparticles, provided that the gas jet velocity is higher than 99 m/s. Particle size measurements confirm this by showing a significant drop of the mode size at both fluidization velocities (Table 3). The jet penetration length was calculated according to correlations proposed by Guo [23] and Hirsan [24] for upward jets in a fluidized bed (Table 2). The jet length penetration values indicate that the jet of air, even at the lowest velocity, can still penetrate through the bed and touch the plate.
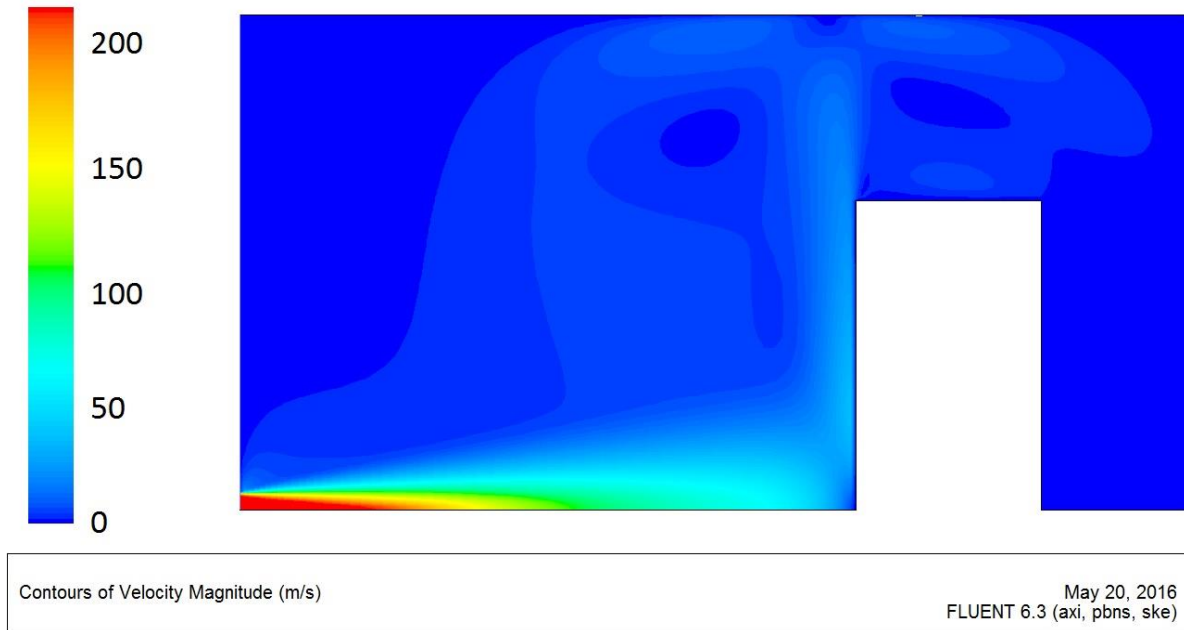
Figure 4.2 Velocity profile of gas phase in vicinity of the impaction plate.

Table 4.2 Calculation of jet length, gas velocity and jet energy close to the plate.

Gas jet velocity (m/s)	Gas velocity close to the plate (distance - 0.5 mm) (m/s)	Jet length (cm)		Maximum kinetic energy per unit mass of particles (m²/s²)
		Guo [1]	Hirsan [2]	
33	13	0.86	0.47	85
99	48	1.33	1.05	1150
132	65	1.48	1.30	2110
165	80	1.62	1.54	3200
197	97	1.74	1.76	4700

Table 4.3 Particle statistics for produced silica aerosols at different fluidization velocities (particle sizes in nm).

Jet velocity (m/s)	$U/U_{mf} = 5.5$				$U/U_{mf} = 6.2$			
	Mode ± SD	D50	GM[1]	GSD[2]	Mode ± SD	D50	GM	GSD
Bypass[3]	125±10	140	151	1.57	—			
0	131±14	121	120	1.58	113±13	119	125	1.72
33	109±10	124	124	1.57	131±16	105	106	2.01
99	85±6	99	105	1.57	113±3	117	118	2.00
132	59±11	94	100	1.69	107±7	105	109	2.03
165	61±4	85	89	1.72	95±7	97	101	2.07
197	55±10	60	67	1.89	59±6	78	85	1.94
[1]Geometric mean								
[2]Geometric standard deviation								
[3]Bypass values were measured without fluidization								

In this system, two principal parameters affect the choice of an appropriate fluidization velocity: the impactor system level and the particle entrainment rate. The superficial gas velocity must be high enough that the bed can reach the impactor system level (i.e. higher than the jet outlet), but not too high that it leads to a high entrainment of particles beyond the impactor plate. In this particular configuration, for $U/U_{mf} < 5.5$, the jet cannot capture particles and bring them into the jet-impaction system. Conversely, for $U/U_{mf} > 6.2$, particle entrainment becomes high, thereby increasing the particle concentration in the aerosol outlet stream beyond the specifications of the SMPS. Therefore, the fluidization velocity range selected for this work was between $U/U_{mf} = 5.5$ and 6.2.
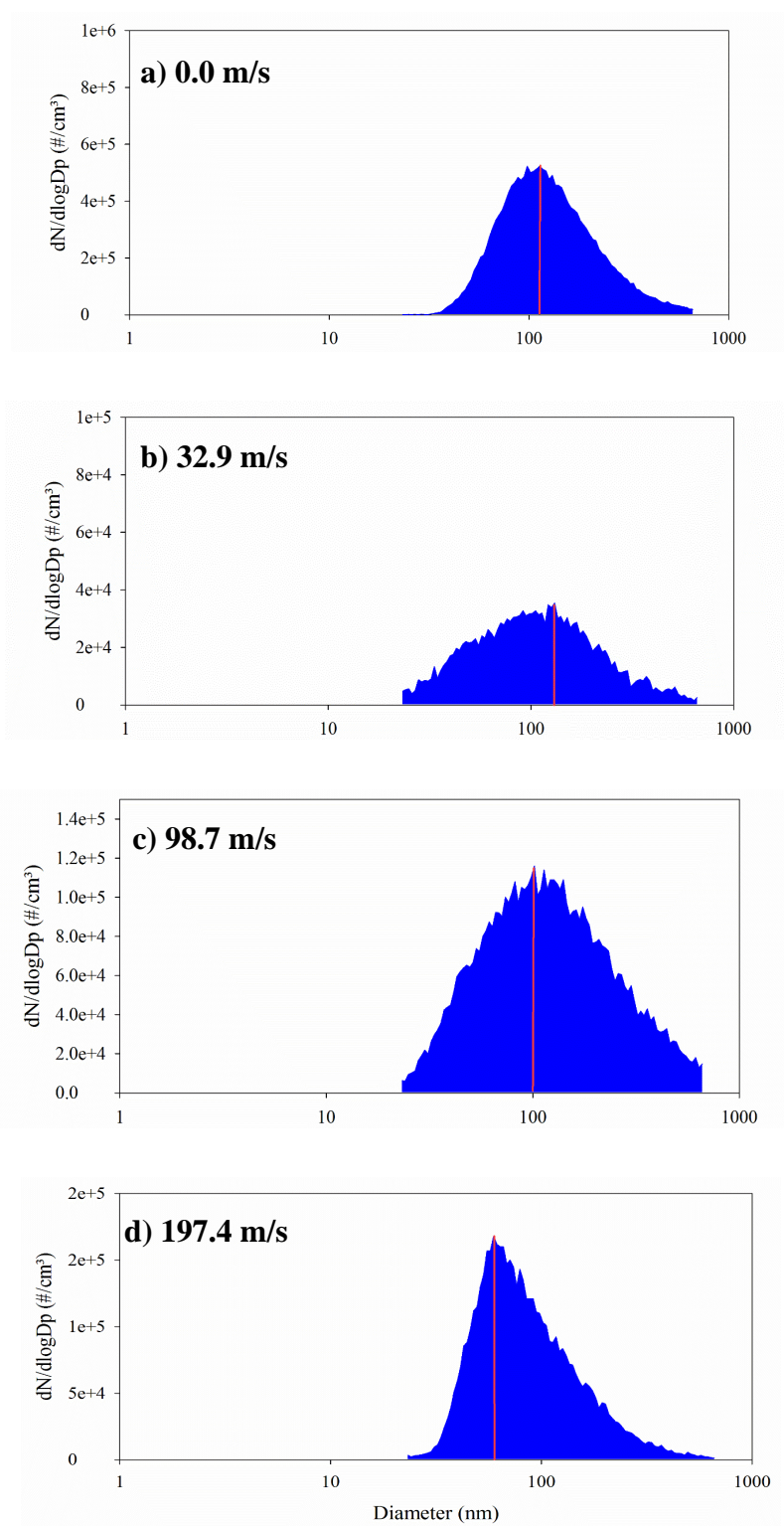
Figure 4.3 Particle size distribution at constant fluidization velocity of U/U$_{mf}$ = 5.5 and different jet velocities.

Fig. 4.3 shows the particle size distributions of the silica NPs at constant fluidization velocity ($U/U_{mf} = 5.5$) and different jet velocities, running from 0 to 197 m/s. All data are number-weighted and show the electrical mobility diameter of particles. The geometric mean diameters differ from the median diameters by 0–12% and follow the same trend with increasing jet velocity. The graphs show that under the same fluidization conditions, by increasing the impaction velocity, the particle size distribution shifts towards smaller sizes for jet velocities > 99 m/s, reaching their smallest values (below 100 nm) at a jet velocity of 197 m/s. However, the geometric standard deviation (GSD), as a dispersity criterion of particle size distribution, increases at the same time (Table 4.3). This can happen owing to the fact that increasing the local jet velocity increases the total superficial velocity, which in turn leads to entrainment of larger particles. Furthermore, due to the wide range of individual NP sizes in the supplied nanopowder, increasing the GSD can actually be an indicator of a higher level of agglomerate dispersion. On the other hand, as seen in Fig. 4.3, by increasing the jet velocity the overall particle concentration increases. Indeed, increasing the superficial velocity in a bed increases the particle loss from the bed.

In the bypass configuration, the particle size distribution of the nanopowders does not change considerably compared to the control case (jet velocity = 0 m/s), confirming that de-agglomeration occurs mainly as a result of impaction inside the bed, not through collisions in the fluidized bed.

Finally, TEM images and geometric particle size distribution obtained from them confirm the effect of impaction on dispersion of dry agglomerates (Fig. 4.4). The non-impacted sample was collected on TEM grids by installing the TEM grid on the lateral surface of the rod close to the bed. This allows fluidized particles to sit on TEM grids only by a diffusion mechanism. Dendritic structures with high fractal-like dimensions are observed, typical of silica NP agglomerates in the gas phase. Particles collected on a TEM grid attached to the impaction plate, following treatment with a jet velocity of 99 m/s (Fig. 4, right) are dispersed into small clusters. ImageJ [25] was used to analyze the TEM micrographs and extract particle size distributions, implementing watershed separation after the threshold was set to neutralize any shielding effects. Particle sphericity close to unity facilitated calculations of the particle diameter from the surface area. To plot the histogram, image artefacts showing diameters smaller than the primary particle size (20 nm) were eliminated. A large number of small primary particles ranging from 20 to 550 nm were identified after impaction, three times greater than the number of discrete particles before impaction. After impaction, almost 80%

of the particles were smaller than 100 nm, with the remainder composed of larger individual particles and some small clusters. On the other hand, before impaction, the size of agglomerates reached 900 nm. It should be noted that TEM sampling was conducted directly at the impactor level — it therefore illustrates the trend of de-agglomeration, but the size distribution is different from that observed downstream at the SMPS. In addition, TEM results revealed that the supplied nanopowder has a wide primary particle size distribution in the range of 20 to 500 nm. This affects the fluidization behavior, the agglomeration/de-agglomeration rate of powders, and accounts for some of the increased GSD.
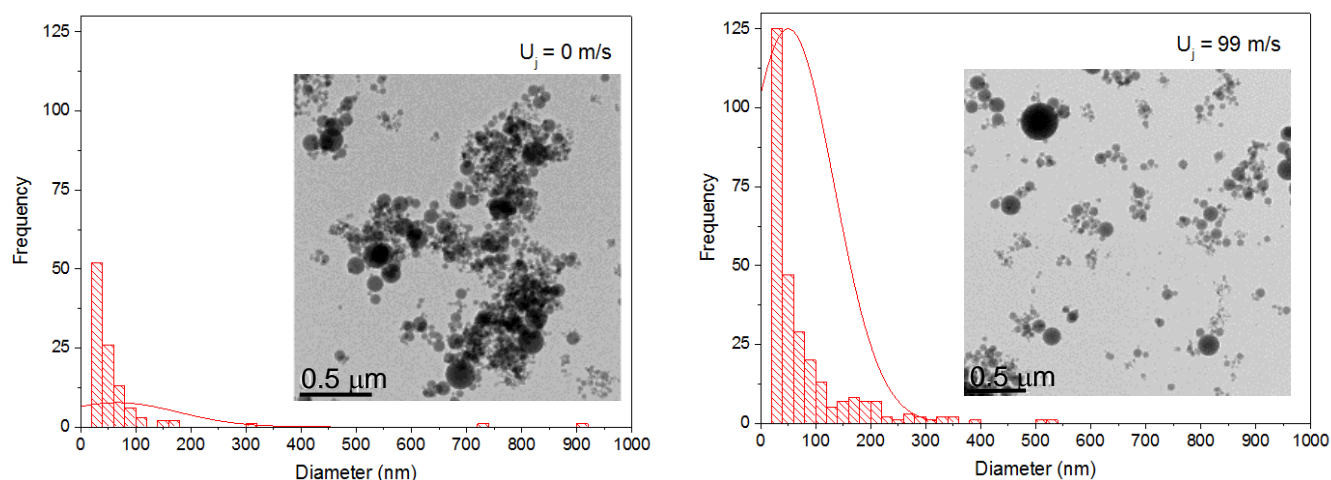
Figure 4.4 Particle size distributions obtained from TEM images and corresponding TEM mages of non-impacted (left) and impacted (right) silica NP.

4.4 Conclusion

This experimental work forms the basis of our efforts towards a controllable technique for NP dispersion in the gas phase. Here, we showed that utilizing a high speed jet and impaction plate in a fluidized bed can increase the de-agglomeration rate of NPs and produce particles with a smaller mode size. The results of CFD simulation reveal that the kinetic energy of particles upon impaction is high enough to break up the agglomerates, which is confirmed by SMPS monitoring. TEM results also confirm the effect of impaction on fragmentation of large agglomerates to smaller clusters and individual NPs. As confirmed by a bypass configuration study, the de-agglomeration rate is strictly controlled by jet velocity, which governs the impaction mechanism. However, the

effect of re-agglomeration inside the fluidized bed after impaction remains unknown and will be the focus of on-going work. Furthermore, to overcome reagglomeration of NPs, their surface energy needs to be reduced by surface functionalization, which will be the focus of an upcoming work.

Acknowledgements

4.5 References

[1] Y. Min, M. Akbulut, K. Kristiansen, Y. Golan, J. Israelachvili, The role of interparticle and external forces in nanoparticle assembly, Nat Mater, 7 (2008) 527-538.

[2] G. Calvert, M. Ghadiri, R. Tweedie, Aerodynamic dispersion of cohesive powders: A review of understanding and technology, Advanced Powder Technology, 20 (2009) 4-16.

[3] D. To, R. Dave, X. Yin, S. Sundaresan, Deagglomeration of nanoparticle aggregates via rapid expansion of supercritical or high-pressure suspensions, AIChE Journal, 55 (2009) 2807-2826.

[4] M. Seipenbusch, P. Toneva, W. Peukert, A.P. Weber, Impact Fragmentation of Metal Nanoparticle Agglomerates, Particle & Particle Systems Characterization, 24 (2007) 193-200.

[5] S.S. Ali, E.H. Al-Ghurabi, A. Ajbar, Y.A. Mohammed, M. Boumaza, M. Asif, Effect of Frequency on Pulsed Fluidized Beds of Ultrafine Powders, Journal of Nanomaterials, 2016 (2016) 1-12.

[6] T.R.N. Jinghai Yi, Nanoparticle aerosol generator, West Virginia University, 2010.

[7] B. Stahlmecke, S. Wagener, C. Asbach, H. Kaminski, H. Fissan, T.A.J. Kuhlbusch, Investigation of airborne nanopowder agglomerate stability in an orifice under various differential pressure conditions, Journal of Nanoparticle Research, 11 (2009) 1625-1635.

[8] M. Ihalainen, T. Lind, T. Torvela, K.E.J. Lehtinen, J. Jokiniemi, A Method to Study Agglomerate Breakup and Bounce During Impaction, Aerosol Science and Technology, 46 (2012) 990-1001.

[9] M. Ihalainen, T. Lind, T. Torvela, J. Ruusunen, A. Lahde, P. Tiitta, J. Jokiniemi, Fragmentation and bounce of nanosized agglomerates due to the impaction, Particle Technology Forum 2013 - Core Programming Area at the 2013 AIChE Annual Meeting: Global Challenges for Engineering a Sustainable Future, November 3, 2013 - November 8, 2013, AIChE, San Francisco, CA, United states, 2013, pp. 129-130.

[10] S. Froeschke, S. Kohler, A. P. Weber, G. Kasper, Impact fragmentation of nanoparticle agglomerates, Journal of Aerosol Science, 34 (2003) 275-287.

[11] J.P. Quigley, K. Herrington, M. Bortner, D.G. Baird, Benign reduction of carbon nanotube agglomerates using a supercritical carbon dioxide process, Applied Physics A, 117 (2014) 1003-1017.

[12] K. Hielscher, Ultrasonic Milling and Dispersing Technology for Nano-Particles, MRS Proceedings, 1479 (2012) 21-26.

[13] Y. Hwang, J.-K. Lee, J.-K. Lee, Y.-M. Jeong, S.-i. Cheong, Y.-C. Ahn, S.H. Kim, Production and dispersion stability of nanoparticles in nanofluids, Powder Technology, 186 (2008) 145-153.

[14] M. Inkyo, T. Tahara, T. Iwaki, F. Iskandar, C.J. Hogan, Jr., K. Okuyama, Experimental investigation of nanoparticle dispersion by beads milling with centrifugal bead separation, J Colloid Interface Sci, 304 (2006) 535-540.

[15] S. Miranda, Using an agitator bead mill for nanoparticle dispersion and comminution, Nanotechnology NETZSCH Premier Technologies, (2011).

[16] V.S. Nguyen, D. Rouxel, R. Hadji, B. Vincent, Y. Fort, Effect of ultrasonication and dispersion stability on the cluster size of alumina nanoscale particles in aqueous solutions, Ultrason Sonochem, 18 (2011) 382-388.

[17] R. Shah, D. Eldridge, E. Palombo, I. Harding, Lipid Nanoparticles: Production, Characterization and Stability, Springer International Publishing2014.

[18] L. Jiang, L. Gao, J. Sun, Production of aqueous colloidal dispersions of carbon nanotubes, Journal of Colloid and Interface Science, 260 (2003) 89-94.

[19] J.H. Fendler, Colloid chemical approach to nanotechnology, Korean Journal of Chemical Engineering, 18 (2001) 1-13.

[20] D. Wen, Y. Ding, Effective Thermal Conductivity of Aqueous Suspensions of Carbon Nanotubes (Carbon Nanotube Nanofluids), Journal of Thermophysics and Heat Transfer, 18 (2004) 481-485.

[21] J.R. van Ommen, J.M. Valverde, R. Pfeffer, Fluidization of nanopowders: a review, J Nanopart Res, 14 (2012) 737.

[22] C.A. Dorval Dion, W. Raphael, E. Tong, J.R. Tavares, Photo-initiated chemical vapor deposition of thin films using syngas for the functionalization of surfaces at room temperature and near-atmospheric pressure, Surface and Coatings Technology, 244 (2014) 98-108.

[23] Q. Guo, G. Yue, J. Zhang, Z. Liu, Hydrodynamic characteristics of a two-dimensional jetting fluidized bed with binary mixtures, Chemical Engineering Science, 56 (2001) 4685-4694.

[24] T.M. Knowlton, I. Hirsan, The Effect of Pressure on Jet Penetration in Semi-Cylindrical Gas-Fluidized Beds, (1980) 315-324.

[25] C.A. Schneider, W.S. Rasband, K.W. Eliceiri, NIH Image to ImageJ: 25 years of image analysis, Nature Methods, 9 (2012) 671-675.

CHAPTER 5   ARTICLE 2: SOLID HOLD-UP MEASUREMENT IN A JET-IMPACTOR ASSISTED FLUIDIZED BED USING GAMMA-RAY DENSITOMETRY

Hamed Nasri Lari, Majid Rasouli, Jamal Chaouki, Jason R. Tavares

Department of Chemical Engineering, École Polytechnique de Montréal, P.O. Box 6079, Station Centre-Ville, Montreal, Quebec, H3C 3A7, Canada

KEYWORDS:

Nanoparticle fluidization, Solid hold-up, Gamma densitometry, Profile reconstruction, Jet-assisted fluidization

Abstract

A jet-impactor assisted-fluidized bed (JIAFB) for continuous de-agglomeration of nanopowder agglomerates was presented in previous work. Therein, a jet caused agglomerates to impinge up an impactor, where they would break. However, efficient impactor positioning will be dictated by particle momentum: the product of solid concentration and velocity must be highest. Herein, the variation of solid hold-up was measured in a fluidized bed of Fe_2O_3 nanoparticles using gamma densitometry. Behaviour was compared under minimum fluidization and bubbling regimes, over a wide range of jet velocities (0-200 m s^{-1}). A new line-decomposition approach allowed mapping local solid distribution across seven axial and five radial positions, tangibly demonstrating how increasing the gas velocity enhanced the fluidization quality by increasing axial solid diffusivity. Conversely, increasing jet velocity locally decreased solid hold-up in the jet-affected zone, and brought about inhomogeneities. With this information in hand, jet-to-impactor distance was optimized and validated experimentally.

Keywords: nanoparticle fluidization, jet-impactor assisted fluidized bed, solid hold-up, gamma densitometry, profile reconstruction

5.1 Introduction

De-agglomeration and the production of size-controlled powders have been the focus of many studies [1-7] in powder technology applications in the pharmaceutical [8, 9], food [10], and chemical [11] industries. It becomes more important when handling cohesive powders, particularly nanopowders, in which strong interparticle forces (e.g. van der Waals forces) increase the heterogeneity in particle size distribution through the formation of agglomerates. Common gas-based de-agglomeration methods break up dry powder agglomerates by generating a turbulent shear flow, e.g. using microjets [12-14]. Such secondary gas injection into a fluidized bed has been used in many industrial applications such as to control particle size [15], injecting additional reactants locally, promoting selectivity or diluting explosive reagents [16]. In previous work [17], the high kinetic energy of a jet-impactor system inside a fluidized bed was exploited to continuously and controllably break up nanoparticle agglomerates, and demonstrated experimentally that a threshold velocity (i.e. kinetic energy level) must be attained to achieve de-agglomeration. However, that study only considered particle velocity within the jet stream,

ignoring the solid hold-up (the volume fraction of a flow occupied by the solid phase). While high velocity remains a requirement for agglomerate break-up, solid hold-up will dictate the overall rate at which de-agglomeration can occur – in other words, the process efficiency. Therefore, to maximize the efficiency of nanoparticle de-agglomeration, it is necessary to optimize the jet-to-impactor distance with respect to both particle velocity and solid hold-up, and this has not yet been thoroughly addressed in the literature.

In a broader view, adding a high-velocity jet changes the hydrodynamics of a fluidized bed dramatically. While different from the jet-impactor approach, several studies have shown that adding a jet to a fluidized bed system effectively enhances the fluidization performance and powder mixing within the column [12-14, 18-22] (Table 5.1). Hong et al. [13] investigated the effect of downward and upward jets in the fluidization of fine glass beads and fluid catalytic cracking (FCC) particles. Although their work was limited to Geldart group A powders (contrary to nanoparticles, which behave as cohesive Geldart group C particles), they concluded that a high-speed millimeter-sized jet could break the agglomerates and improve fluidization quality. Further, a downward jet located inside the bed avoids jet penetration through the whole bed and provides more efficient solid mixing. Pfeffer et al.[12, 14], by using the same technique with single or multiple micron-sized jets, showed the jet sizes ranging from 127 to 508 μm provided enough shear to break nanoparticle agglomerates or reduce the formation of agglomerates. By measuring the bed expansion and pressure drop through the bed, they indicated that solid particles distribute in a larger segment of the bed, hence increasing the bed expansion. Dimensionless bed height measurements for a wide range of nanopowders show microjet assistance alters the fluidization regime, from Agglomerate Bubbling Fluidization (ABF) to Agglomerate Particulate Fluidization (APF) behavior. The position of the jet has a determinant role in the performance of the bed - higher performance was achieved when the jet tip was close to the gas distributor plate pointing downward. In another work, using Focused Beam Reflectance Measurement (FBRM) and Particle Vision Measurement (PVM) probes, Pfeffer et al. characterized the number-weighted and volume-weighted agglomerate size distributions for both APF and ABF type nanopowders in the splash zone. They demonstrated that, when the superficial gas velocity increases, the concentration of agglomerates decreases, which is in fair agreement with the increased bed expansion and higher porosity observed [21].

To reveal the hydrodynamics of a fluidized bed in the presence of microjets, Van Ommen et al. simulated the system using a CFD-DEM model [22]. They concluded that agglomerate-agglomerate collisions are responsible for the de-agglomeration in the zone below the jet, rather than the drag force applied by the jet. In addition, their results show that voidage does not significantly change when the jet is on or off. As no bed expansion was observed in the simulation results due to high jet speed, they further conclude that the major contribution for bed expansion comes from agglomerate breakage. Although these research endeavors have highlighted positive effects from using jets to fluidize Geldart group C powders, the variations in solid-gas distribution patterns in the presence of jets have not yet been addressed. Understanding these dynamics is essential because the performance of multiphase systems depends significantly on the phase distribution.

Table 5.1 Material and jet properties used in the literature for the fluidization of particulate materials.

Powder	Powder Type	Jet direction(s)	Diameter of the Jet	Mach number (Jet velocity)	Objective of paper	Ref.
Glass beads	Diameter = 40 μm, Density = 2.5 g·cm^{-3} Group A	Downward and upward	2.54 cm	0.04 to 0.18 (15 to 61 m s^{-1})	Experimental and numerical study	[13]
Sand	Diameter = 421 μm, Group B	Downward jet	Downcomer size of 6 mm, opening size of 64 mm	0.015 to 0.036 (5.1 to 12.4 m s^{-1})	Hydrodynamic study	[19, 20]
Aerosil R974, 200, 90, Raw 90 (SiO$_2$) Aeroxide P25 (TiO$_2$), Alu C (Al$_2$O$_3$)	Diameter = 12-21 nm Group C (both ABF- and APF-type)	Downward and upward	127, 177, 254, and 508 μm	0.93 (320 m s^{-1})	Improving fluidization of ultrafine powders	[12, 14, 18]

Aerosil R974 (APF-type), Aerosil 90 (ABF-type)	Diameter = 12 and 20 nm Group C	Downward	Not mentioned	0.93 (320 m s^{-1})	*In situ* measurement of agglomerate size	[21]
Aeroxide P25 (TiO$_2$)	Diameter = 21 nm Group C (ABF)	Downward	128 μm	0.87 (300 m s^{-1})	Experimental and numerical study	[22]
Silica (SiO$_2$)	Diameter = 20 nm Group C (ABF)	Upward (coupled with an impactor)	254 μm	0.57 (197 m s^{-1})	De-agglomeration	[17]

The hydrodynamic properties in fluidized beds can be measured using two groups of techniques: invasive and non-invasive techniques. In invasive techniques, such as fiber optic or capacitance probes, a probe is installed inside the system and can measure phase fraction distributions locally, although this disrupts the internal flow pattern. Such disruptions are compounded in the case of cohesive powders, due to sticking on the tip of the probe. On the other hand, non-invasive techniques, such as electrical capacitance tomography (ECT), X-ray computed tomography (CT), gamma-ray tomography, and gamma-ray densitometry, generally provide information about the phase profile in a broader range such as over a line, a cross-section, or in a volume, and do not face issues related to powders sticking on the probe [23, 24]. Gamma-ray densitometry in particular is flexible, having good spatial resolution, and being suitable for a wide range of column sizes. Multi-source gamma densitometry even allows for the reconstruction of bubbles [18, 25]. Despite this, there is still a lack of simple reconstruction techniques that can assess the local phase hold-up.

Several studies have made advances to measure the solid-gas distribution, mainly using solid hold-up inside fluidized beds in the presence of jets, but not for Group C powders. The flow pattern of high-velocity gas injection into both fixed and fluidized beds was studied by Koeninger et al. [26] for fine glass beads using non-invasive particle image velocimetry (PIV) and X-ray Computed Tomography. Stimulating the bed with a horizontal millimeter-sized jet decreased the solid concentration (solid fraction of 0-3%) in the jet line, which reduced further at higher jet velocities.

Hence, particle entrainment mainly occurs in the zone around the jet boundary. Moreover, no significant differences were observed for the particle velocity in fluidized and fixed states. Another non-invasive technique, gamma-ray computed tomography, was also used to measure the solid hold-up in a fluidized bed of Geldart B particles [27], showing that increasing the gas velocity not only increases the voidage of the bed (in the core), but also improves mixing within the column, leading to more homogeneous particle fluidization. Further, the gas hold-up in the system depends on the solid particle density. The lower the particle density, the higher the voidage (i.e. lower solid phase) in the center of the bed, and a region of higher gas hold-up in the center and a region of low gas hold-up (higher solids concentration) can be determined near the walls. Koeninger et al. studied particle concentration and velocity in the vicinity of a horizontal jet in a bed of glass beads (92 μm) [26]. They showed a dilute zone forms near the tip of the nozzle with a very low (1-3%) axial solid concentration, which then significantly increases and reaches a maximum corresponding to the solid concentration of the dense bed. The distance from low concentration to dense bed is translated as the nozzle penetration length. The solid concentration inside the jet is reduced by increasing the gas velocity. Nevertheless, the particle concentration is higher close to the tip due to the venturi effect.

Measuring the solid hold-up during nanoparticle fluidization using gamma densitometry has been the focus of a few works [23, 28]. Jiradilok et al. measured the silica nanoparticle volume fraction in a circulating fluidized bed riser, showing that solid compression occurs in the riser due to pressure wave propagation following the detonation of high pressure, high temperature gas in the bed [28]. Esmaeili and Chaouki [23] measured the solid hold-up in a fluidized bed by means of both gamma densitometry and fiber optic probing. They showed that, although bed expansion is not large enough for zirconia and aluminum nanopowders (ABF type), these fluidize uniformly in the bed. The solid hold-up in the lower part of the bed (close to the distributor) changes significantly as a function of gas velocity, whereas it remains unchanged in the upper part of the bed. This contrasts with invasive fiber optic measurements that overestimated the overall solid concentration at higher gas velocities when considering the bed expansion results.

However, adding a high velocity jet dramatically changes the hydrodynamics of a nanopowder fluidized bed, and this has not yet been addressed in the literature. Understanding the hydrodynamics of fluidized beds is key to their effective scale-up, efficient operation, and proper

design. Beyond enabling to better situate an impactor for de-agglomeration, solid concentration is an important parameter to understand the agglomeration and de-agglomeration mechanisms in a fluidized bed.

Herein, the influence of a microjet flow was evaluated on the solid distribution in a fluidized bed of nanopowders in three different configurations: conventional, jet-assisted, and jet impactor-assisted fluidized bed. The axial and radial solid distribution profiles were measured for all configurations using gamma-ray densitometry, and subsequently used to reconstruct and map the local profiles. Gamma densitometry allows measurements with focus on the jet zone through adjusting the size of the beam. Also, Fe_2O_3 nanopowder was selected for this study, because of its stable long-term fluidization, higher density (i.e. lower voidage), and higher attenuation coefficient. With this information in hand, we then focus on the jet-impactor region to optimize the jet-to-impactor distance with respect to the impact momentum of particles and verify the optimum point with experimental force measurements. The optimized de-agglomerator can then be combined with a continuous coating process to prevent re-agglomeration [29].

5.2 Method

5.2.1 Principles of Gamma Densitometry

On the basis of the Beer-Lambert law, Knoll [30] showed that when a beam of mono-energetic gamma rays is propagated through a two-phase mixture, the number of photons counted per second, C, is given by:

$$ln\left(\frac{C}{C_0}\right) = -\left[(1 - \varepsilon)\left[\frac{\mu}{\rho}\right]_p \rho_p + \varepsilon\left[\frac{\mu}{\rho}\right]_g \rho_g\right] d \qquad \text{Equation 5.1}$$

where C_0 is the number of photons counted per second while the system is under vacuum; ε is the voidage of the bed; $\left[\frac{\mu}{\rho}\right]_p$ and $\left[\frac{\mu}{\rho}\right]_g$ are the mass attenuation coefficients of the solid and gas phases, respectively; ρ_p and ρ_g are the densities of solid and gas phases, respectively, and d is the path length of the gamma ray through the system. By neglecting the attenuation of the gas compared to

the attenuation of the solid phase,, the average solid fraction in the system $(1 - \varepsilon)$ along the gamma ray line can be calculated as:

$$\varepsilon_s = 1 - \varepsilon = (1 - \varepsilon_b)\frac{ln(C_g/C)}{ln(C_g/C_b)} \qquad \text{Equation 5.2}$$

where subscripts s and g refer to the solid and gas and the ε_b is the voidage or porosity of the bulk powder, which can be calculated by measuring the loose bulk density of powder (ρ_b) and particle density (ρ_p) reported by the manufacturer:

$$\varepsilon_b = 1 - \frac{\rho_b}{\rho_p} \qquad \text{Equation 5.3}$$

The loose bulk density of the powders is measured in a graduated cylinder having the same diameter as the column (repeated three times). The graduated cylinder was filled with powders and leveled up to a minimum height of 10 cm without compaction. The apparent density of the bulk powder is then calculated as $\rho_b = m/V$ by reading the apparent volume (V) and measuring the weight of the powder (m) with 0.1% accuracy (Table 5.2).

After evaluating a series of line-averaged solid hold-up values at a given height (z) and different chords (r), the cross-section solid hold-up at a given z is simply calculated by numerical integration over the cross-section based on the trapezoidal rule, assuming azimuthal symmetry. Similarly, the overall solid hold-up is calculated by integration of the cross-section solid hold-up values over the z direction.

5.3 Experimental

5.3.1 Materials

Magnetic iron oxide (Fe_2O_3) nanopowders, supplied by Nanostructured & Amorphous Materials, Inc. (Los Alamos, New Mexico, USA) were used for all solid hold-up experiments, owing to their ability for long-term fluidization with negligible particle entrainment, lower voidage, and high mass attenuation coefficient compared to their counterparts (e.g. silica nanopowder). Physical properties of the Fe_2O_3 nanopowders are summarized in Table 2. Very large agglomerates produced

during storage, packing, and transportation were sieved out using a 40-mesh sieve with 420 μm openings before fluidization experiments. Dry nitrogen (Air Liquide 99.999 %, water content < 3 ppm) was used as both the fluidizing gas at about 40 psig (275.8 kPa) and the microjet flow at 100 psig (689.5 kPa).

Table 5.2 Physical properties of powders

Powder	Primary particle size (μm)	Particle Density (kg m^{-3})	Powder Type	Voidage*	Mass attenuation coefficient* (m^2 kg^{-1})
Fe$_2$O$_3$	0.020 – 0.030	5240	Geldart C/ABF	0.78 ± 0.01	0.0051 ± 0.0003

* This data was obtained experimentally

5.3.2 Gamma Densitometry Tests

Gamma-ray densitometry was used to measure the solid concentration distribution in the bed and in the vicinity of the jet. A single source-detector system measured line-averaged time-averaged solid hold-up at seven axial and five radial positions, totaling 35 measurement points. The gamma densitometer consisted of a gamma-ray source, a NaI (Tl) scintillation detector (Teledyne Isotope S-1212-I), and a data acquisition system that includes a pre-amplifier, an amplifier and a discriminator (ORTEC ACE Mate) to record the signals. A scandium element (Sc 46) was used as the gamma-ray source with a half-life of 84 days, activated in the SLOWPOKE reactor at Polytechnique Montreal. For all experiments, the 450 μCi source was retained, using a two-minute total scan time for each position, as these conditions led to the lowest error measurement (~0.1%). To scan one bed cross-section, the source-detector pair, located on the opposite sides of the bed, moved along the axis perpendicular to the beam. For each cross-section, count data was collected at five chords 1 cm apart (Fig. 5.1). According to the jet half angle calculations [31], the collimator was designed such that the spatial resolution of the gamma densitometer is 2 mm at the bed center line (e.g. at the tip of the nozzle), calculated based on the collimator configuration parameter [25, 32]. This guarantees the entire beam is within the jet zone. Additional details pertaining to the gamma-ray densitometry approach are provided as supplementary information (Fig. 5.S1,2).
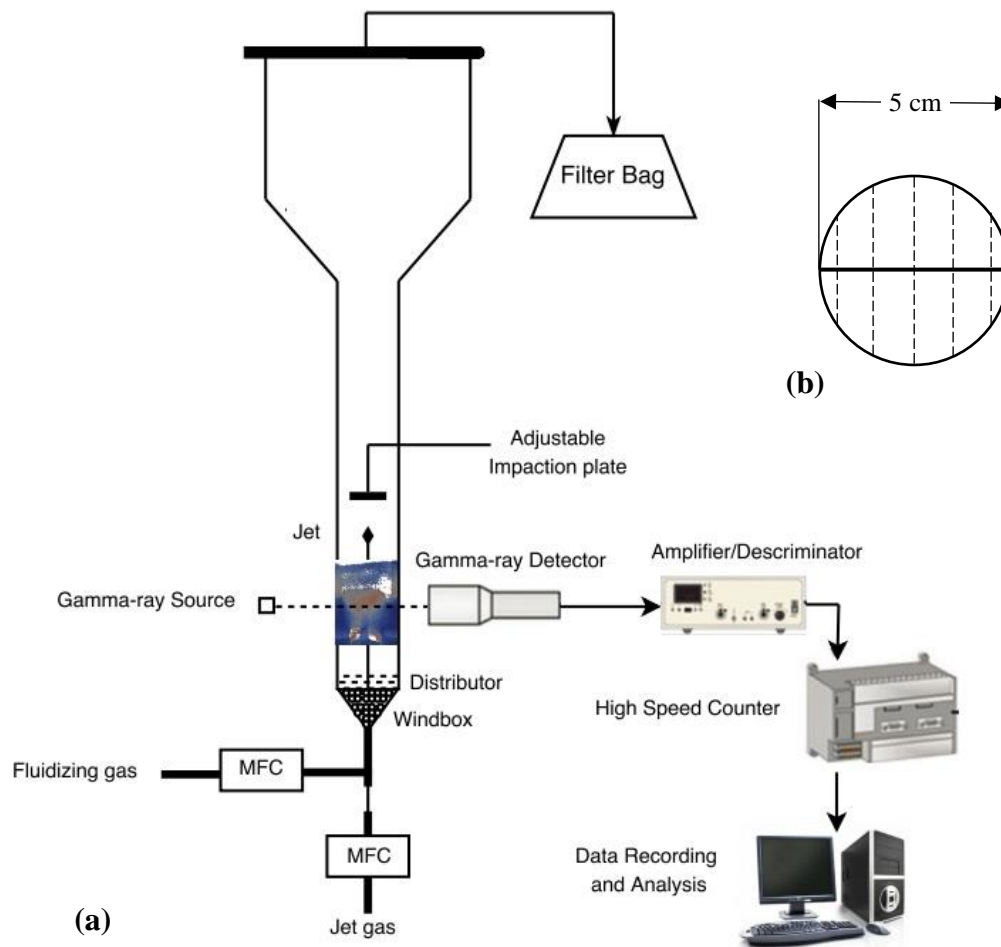
Figure 5.1 (a) Schematic of the fluidized bed and gamma-ray densitometry system; (b) Five radial positions (chords) to map solid hold-up in a column cross section

5.3.3 Experimental Setup

The fluidization column consisted of a poly(methyl methacrylate) (Plexiglas) tube with an internal diameter of 0.05 m and a wall thickness of 0.007 m (Fig. 5.1). The total height of the bed and freeboard was 60 cm, and it was connected to a larger cylinder with a diameter of 0.3 m, used as the disengagement zone. This prevented the particles from being entrained out of the bed by decreasing the upward flux of particles and gas. Several ports at different heights allowed for the installation of the microjet and the impactor plate. The fluidizing gas, after passing through a mass flow controller (MFC), wind box, and distributor with a pore size of 20 μm entered the column. The wind box contained small wood packings to uniformly distribute the gas flow. A 0.01 inch.

(254 µm) ID upward tube was employed as the jet, and the jet flow was controlled by a second mass flow controller. At the end of the disengagement zone, a HEPA filter bag removed any entrained nanoparticles. Two pressure ports, at the top of the distributor and at the top of the freeboard, were connected to a digital manometer to measure the differential pressure across the bed.

5.3.4 Force Measurements

A commercial piezoresistive force sensor (Honeywell Sensing and Productivity Solutions) was adapted to measure forces applied from the gas and solid particles inside the jet flow. The input voltage was maximized (12 V) to make the sensor more sensitive to the jet flow. The measuring surface of the sensor was extended by gluing a very thin, 1-inch stainless-steel disc on top of its actuator. The force sensor assembly was then attached to a stainless-steel rod and the electronic pins and connections were covered, without touching the actuator, to avoid any damage or errors resulting from nanopowder ingress. The force sensor was calibrated using standard calibration weights before the tests (Fig. 5.S6). The assembly was installed within the fluidized structure such as to allow only vertical displacement without diverging horizontally. The output signal from the sensor was recorded using a data acquisition card connected to a computer. Each data point was recorded over two minutes at a sampling frequency of 10 Hz, and all measurements were repeated three times.

5.4 Results and Discussion

5.4.1 Fluidization behavior of iron oxide nanopowder and overall solid hold-up

Theoretically, 20 nm magnetic Fe_2O_3 nanoparticles, due to their size and density, should be fluidized individually at very low superficial gas velocities, on the order of 10^{-7} cm/s. However, experiments show the onset of fluidization occurs at a gas velocity of 0.85 cm/s (Fig. 5.2), which corresponds to the fluidization of a 70 µm particle (assumed density of 1150 kg/m3) [33].. This significant difference demonstrates that nanopowders are fluidized in the agglomerate state due to the high level of interparticle forces present, mainly van der Waals interactions. At 0.85 cm/s, Fe_2O_3 nanopowders begin to fluidize uniformly with a low bed expansion (10% of initial height of

the bed). Expansion increases to 55% of initial bed height at superficial gas velocities three times larger than minimum fluidization velocity (U_{mf}) (Fig. 5.2). The onset of the bubbling regime occurs at a gas velocity of 1.7 cm/s. Bubble size increases with gas velocity up to 3 cm/s, which may cause negligible elutriation in long-term fluidization. These characteristics, along with the physical properties of the powder (i.e. simple agglomerate size and bulk density), indicate an ABF regime according to the Wang sub-classification [34], in agreement with previous works [35]. As a rule of thumb, nanoparticles (< 100 nm) with a bulk density > 100 kg/m^3 are fluidized as ABF, whereas those with a bulk density < 100 kg/m^3 show an APF behavior [34]. In the presence of the nozzle, the bed expansion increases by a maximum of 5 % at the highest jet velocity (i.e. 200 m/s), confirming that the upward nozzle does not change the fluidization behavior of the nanopowders.
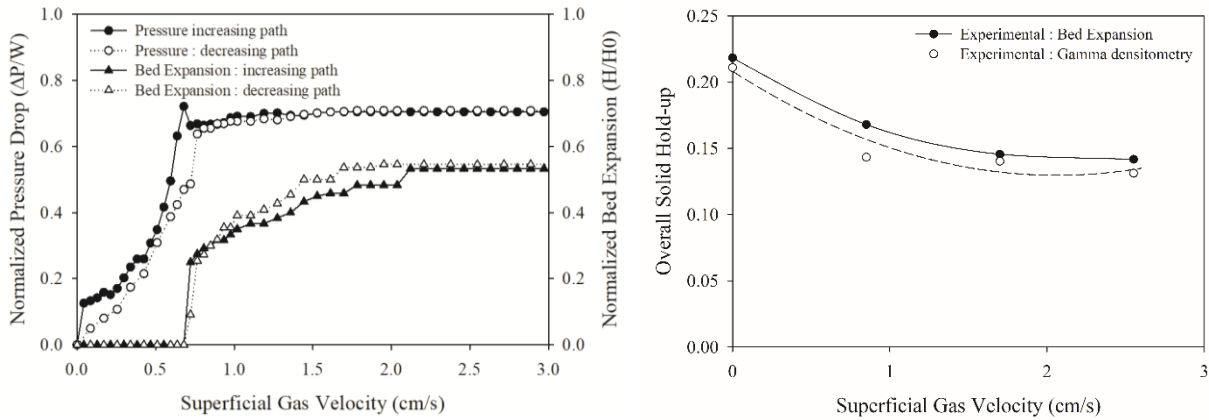
Figure 5.2 (a) Fluidization curve for iron oxide nanoparticles; (b) comparison of overall solid hold-up measurements using bed expansion results and improved gamma densitometry.

Before evaluating solid hold-up in the presence of a jet and an impactor, the results obtained from gamma densitometry, were first verified with the overall solid hold-up results obtained based on the bed expansion measurements. The latter calculates the overall solid hold-up based on the simple mass balance of the uniformly distributed solid powder in the fluidized bed assuming no elutriation. Given that, experimental bed expansion data can provide a rough estimation of the overall solid hold-up over a wide range of superficial gas velocities. Fig. 5.2b compares the calculated overall solid hold-up from both measurements, confirming that it follows the same trend with a maximum solid hold-up error of 2%, which may stem from the bed expansion measurements and rough assumptions in calculating solid hold-up values. This gives confidence to move forward and study

the local solid hold-up in other zones, particularly in the vicinity of the jet, which is not possible to be measured using the bed expansion measurement.

5.4.2 Radial solid hold-up

To study the effect of the microjet and microjet-impactor on the fluidization behavior of Fe_2O_3 nanopowders, a series of experiments were performed over a wide range of jet velocities (0-200 m/s) in three configurations: conventional (unassisted) fluidization, fluidization in the presence of the jet, and fluidization in the presence of both the jet and impactor. Count data was registered for 2 min with a sampling time of 10 ms, leading to 12,000 data points per measurement. In order to study the solid hold-up in the vicinity of the jet, the gamma densitometer scanned the bed 2.5 mm above the nozzle tip.

Conventional fluidization Typical fluidization, without installation of a jet, shows a uniform radial solid phase distribution (Fig 5.3a and 5.3b). In the axial direction, the solid phase is more concentrated at the bottom of the bed, and more diluted in the upper sections. At U_{mf}, as the bed has not yet fully expanded, a very dilute zone is detected in the splash zone (15 cm above the distributor). By increasing the superficial gas velocity up to three times the minimum fluidization velocity, the bed becomes fully uniform, and the solid phase distribution increases at 15 cm above the distributor, due to full bed expansion (Fig. 5.3b). As expected, the cross-section solid hold-up values decrease with rising gas flow in the system.
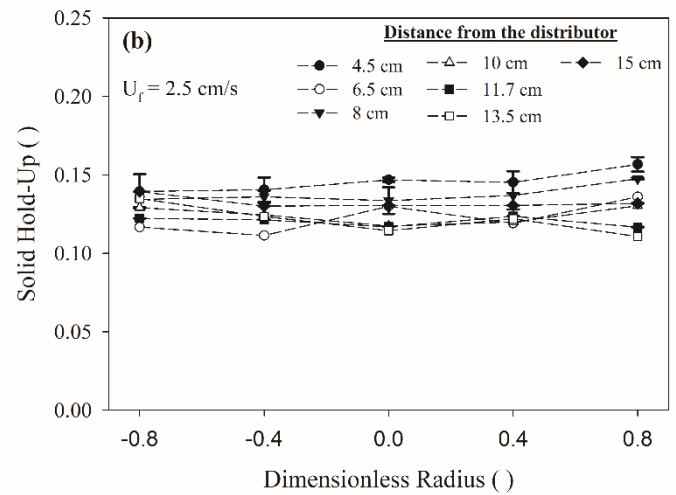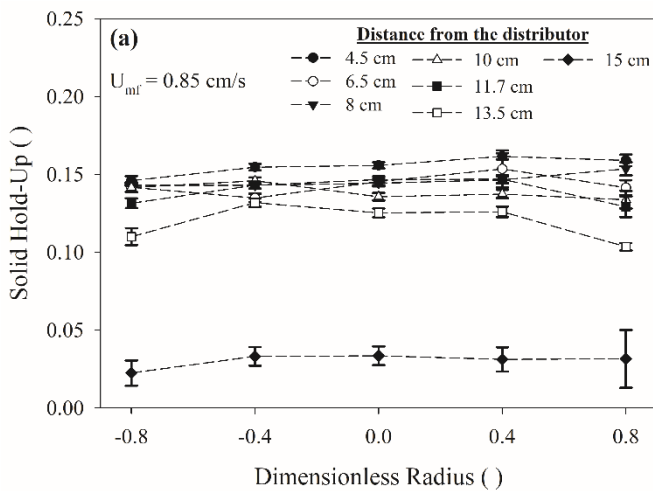
Figure 5.3 (a) Radial solid hold-up at seven levels above the distributor for the conventional fluidization at (a) minimum fluidization ($U_{mf} = 0.85$ cm/s[1]), and (b) bubbling regime ($U_f = 2.5$ cm/s[1])

Microjet-assisted fluidization Once the jet is turned on at U_{mf}, the solid hold-up locally drops at 2.5 mm above the nozzle tip ($r/R = 0$), while it remains almost constant at other radial positions (Fig. 5.4a). The local solid hold-up reduction is more evident at higher jet velocities, representing the formation of a "hole" inside the fluidized bed. This is reasonable as more gas is injected to the system, the less solid hold-up is observed. Comparing the solid hold-up profiles of zero and non-zero jet velocities, injecting the secondary gas stream causes reduction of the mean cross-section solid hold-up in the vicinity of the jet. However, in the bubbling regime (Fig. 5.4b), this local jet effect becomes less apparent. Although the mean cross-section solid hold-up drops compared to the U_{mf} regime because of dilution, the solid hold-up profiles remain almost uniform, while at jet velocities greater than 100 m s^{-1} the jet effect becomes detectable. The results for both regimes show increasing the fluidization gas flow diminishes the effect of the secondary gas flow as a result of increasing bubbles in the system. These alter the flow pattern, thereby increasing mixing and uniformity in the system. Nevertheless, the void created by the microjet is still detectable when the volumetric flow rate of the jet is at least 10% of the superficial gas velocity. This agrees with previous studies for group B and D particles showing that an increase in superficial velocity, exceeding U_{mf}, results in shorter jet lengths [36-39].
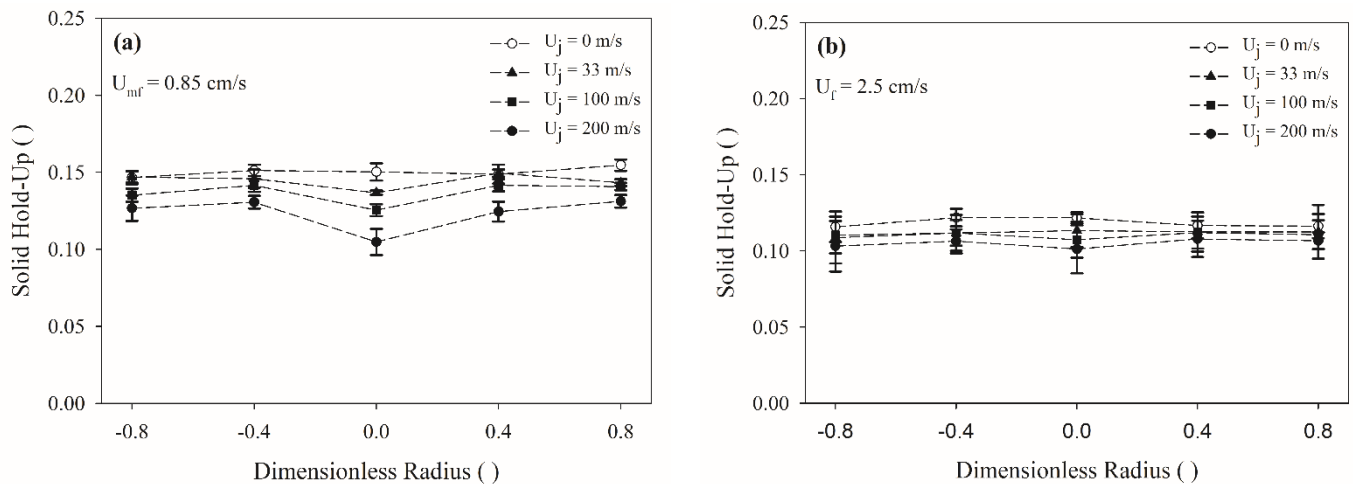
Figure 5.4 Radial solid hold-up profile for microjet- assisted fluidization at (a) minimum fluidization velocity ($U_{mf} = 0.85$ cm/s[1]), and (b) bubbling regime ($U_f = 2.5$ cm/s[1]). Jet is centered at dimensionless radius 0.0.
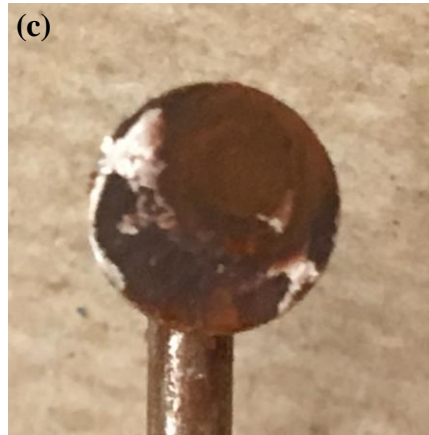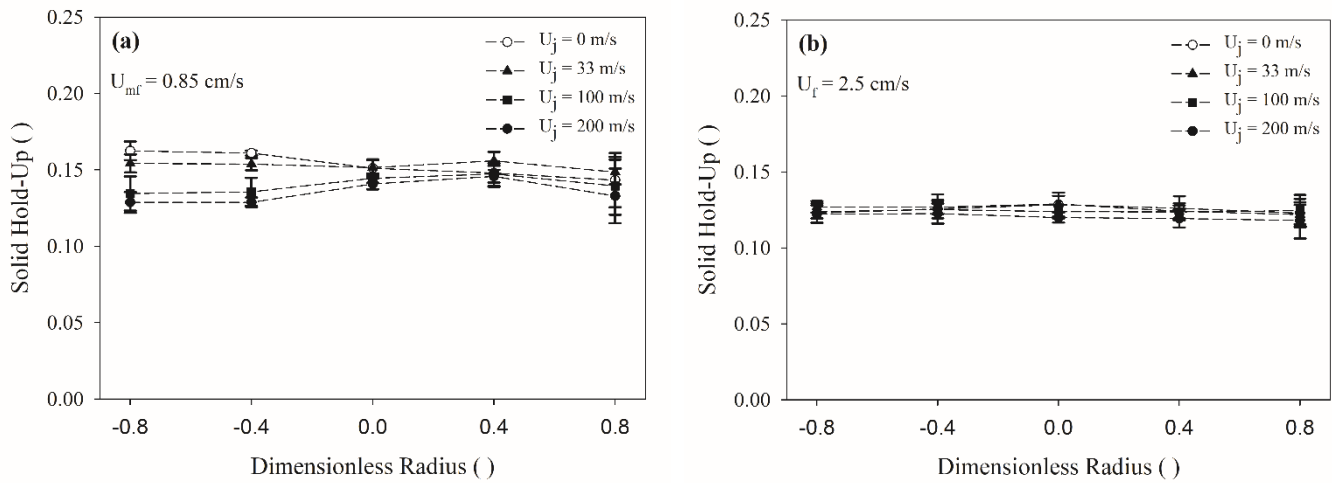
Figure 5.5 Radial solid hold-up profile for microjet-impactor-assisted fluidization at (a) minimum fluidization velocity ($U_{mf} = 0.85$ cm/s[1]) and (b) bubbling regime ($U_f = 2.5$ cm/s[1]); (c) the image of impaction plate after the test.

Microjet-impactor assisted fluidization Installing the impactor causes the solid hold-up profiles to become asymmetric in the vicinity of the microjet-impactor (Fig. 5.5a and 5.5b). In the U_{mf} regime, once the jet is off ($U_j = 0$ m/s[1]), solid hold-up increases slightly from 15% to 17% at the side of the column where the impactor arm is mounted, while it decreases from 15% to 12% at the other side of the column. This occurs due to the side-mounted impactor's arm hindering the free

flow of gas. When starting the jet stream, two different phenomena are observed depending on the jet velocity. At lower jet velocity ($U_j = 33$ m/s^1), solid hold-up slightly reduces under the impactor arm, while it rises under the free section. However, by increasing the jet velocities beyond 100 m/s^1, this flow pattern changes. The mean cross-section solid hold-up drops, and this reduction is more significant under the impactor arm. The jet penetration length calculations based on the Hirsan correlation [36] explains this difference in flow patterns in the vicinity of the microjet-impactor (Table 5.3). Since the distance between the nozzle tip and the impaction plate is 5 mm, at lower jet velocities the maximum jet penetration length is not sufficient to reach to the plate, hence jet flow entrains some particles, splashing them around. However, at jet velocities exceeding 100 m/s^1, the jet length reaches the impactor plate and, due to gas reflection, the solid hold-up drops noticeably at non-centered radial positions. The profile is asymmetric since the impactor has not been installed exactly perpendicular to the jet. Inspecting the impactor after the test confirms this (Fig. 5.5c). This latest result emphasizes that the parametric study (in supplementary information) was improved the densitometry efficiency enough to make this measurement technique sensitive to a slight deviation in jet-impactor installation.

Table 5.3 Minimum, maximum and bubble penetration length as a function of gas jet velocity based on Hirsan correlations [36] for an upward nozzle

Gas Jet Velocity (m s^{-1})	Minimum jet penetration length (mm)	Maximum jet penetration length (mm)	Jet bubble penetration length (mm)
33	0.6	2.6	4.5
100	1.1	6.2	10.1
200	1.9	11.1	16.1

5.4.3 Local Solid hold-up in the vicinity of the jet

Unlike the capacitance probe or fiber optic methods used for characterizing local parameters in previous works, gamma densitometry measures solid phase concentration based on the line-

averaged attenuation of the gamma ray travelling through the system. Although the line-averaged solid hold-up provides information about how the radial and cross-sectional solid particle distribution varies at the jet level as a function of the jet or fluidization velocity, it does not describe the local solid phase distribution in the vicinity of the jet, due to the inherent averaging of the gamma-densitometry technique. In other words, the contribution of secondary gas flow (jet) to solid hold-up distribution is diminished in the fluidizing gas flow. To overcome this problem, a line decomposition approach is proposed to isolate the effect of the secondary microjet flow on the solid hold-up, assuming the solid hold-up is uniform far enough from the jet affected zone (JAZ). For this purpose, the bed is first divided in a number of rings (Fig. 5.6), such that each radial position is allocated to a ring. Next, the solid hold-up needs to be estimated in the outer ring. In the previous section, it was shown Fe_2O_3 nanoparticles fluidize homogenously far away from the jet zone, whereas in the vicinity of the jet the local solid phase concentration changes noticeably due to turbulence. Koeninger et al. [26] showed that, in fluidization of solid particles, solid concentration varies in the jet boundary, where the phase and momentum exchange takes place. Consequently, it is fair to assume that the local solid hold-up is uniform in azimuthal angles far from the JAZ (i.e. in the outer ring). Here, since solid hold-up was measured at five points at each cross section, the surface area is decomposed at each level into three zones (Fig. 5.6). Hence, it may be assumed that:

$$\varepsilon_{l_3} = \varepsilon_r|_{\frac{r}{R}=\pm 0.8} \qquad \qquad \text{Equation 5.4}$$

where, ε_{l_i} and ε_r are the local and radial solid hold-up, respectively. Decomposed solid hold-up values are referred to herein as "local solid hold-up", representing the solid hold-up values in each ring. Generally, solid concentration in fluidized beds varies in all dimensions:

$$\varepsilon_s = \varepsilon_s(r, \theta, z) \qquad \qquad \text{Equation 5.5}$$

At a given height (z) by assuming an azimuthal symmetry as a result of uniform solid distribution, the correlation can be simplified to,

$$\varepsilon_s = \varepsilon_s(r) \qquad \qquad \text{Equation 5.6}$$

Combining this with the Knoll variant of the Beer-Lambert law (Eq. 5.1) considering a constant mass attenuation coefficient gives:

$$A = ln\left(\frac{C}{C_0}\right) \sim \varepsilon_s(r).d \qquad \text{Equation 5.7}$$

On the other hand, the total linear attenuation (A) is the sum of its constituents (i.e. individual interactions of the gamma ray with the solid phase in the ith zone, A_i),

$$A = \sum_i^n A_i(r) \qquad \text{Equation 5.8}$$

Therefore, the time-averaged local solid hold-up at any elevation and radial position is derived from the radial solid hold-up value, by neglecting the non-linear average error in space (acceptable due to the small size of the gamma beam):

$$\varepsilon_r|_{\frac{r}{R}} = \frac{1}{d}\sum_i^n \varepsilon_{l_i}d_i \qquad \text{Equation 5.9}$$

where ε_r is the radial solid hold-up at a given r/R, ε_{l_i} are the local solid hold-up of ith zone, d and d_i are the distance which gamma-ray travels in that radial position and in the ith zone, respectively.

(a)
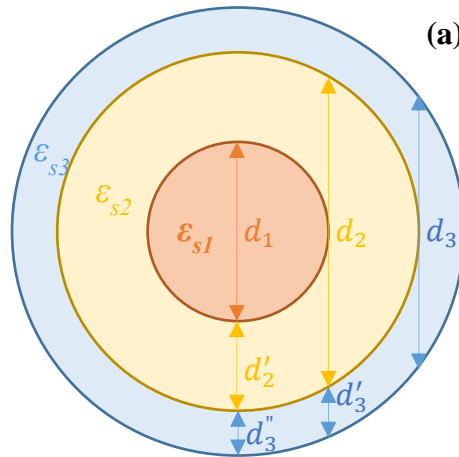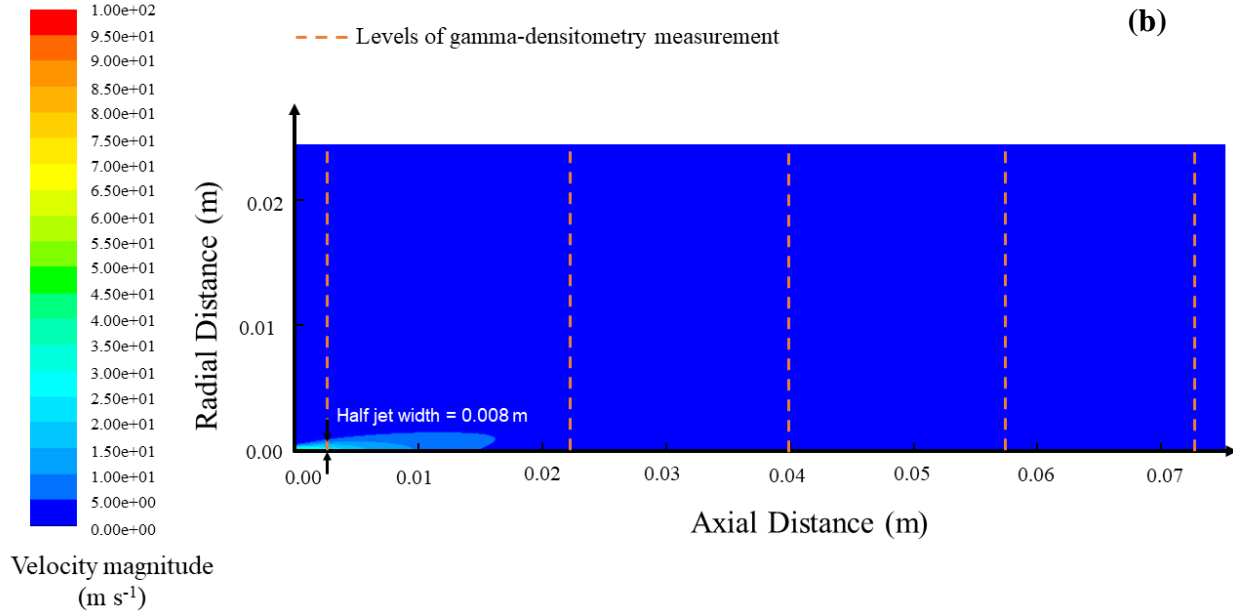
Figure 5.6 (a) Top view of the column showing decomposition of line-averaged solid hold-up; (b) measurement levels overlaid on gas velocity contour obtained by simulation in Fluent to determine the width of JAZ at $U_f = 2.5$ cm s^{-1}and $U_j = 100$ m s^{-1}

To determine the extent of the JAZ (d_1 in Fig. 5.6), a single-phase simulation was performed for all superficial gas and jet velocities using the Fluent 6.3 CFD software. The assumptions and model have been discussed in detail in previous work [17]. By simplifying the model to a two-dimensional axisymmetric case, the geometry was defined as a 5 cm by 60 cm rectangle. A 127 µm line was defined as the tip of the nozzle. Nitrogen was selected as a compressible fluid flow medium. The model was run for two fluidizing gas velocities (0.85 and 2.55 cm/s^1) and three jet velocities (33, 100, and 200 m/s^1). k-ε turbulent physics were used for the case of stationary studies, due to the high Reynolds numbers of the jet (3 to 8×10^3). Although the simulation does not account for the motion of particles, it serves as an approximation to determine the jet widths based on the gas velocity field. The jet width at each cut plane was defined as the position at which the gas velocity reduces to a cut-off point of 5% of the maximum velocity magnitude at the given level. The calculated jet width values show that changing the fluidization regime does not affect the jet width. The half jet width values for all runs show a constant value of 0.008 m at 2.5 mm above the nozzle tip. Since the maximum jet penetration length according to this model and Hirsan correlations (Table 5.3), even at the highest velocity, does not reach to the second gamma densitometry

measurement level, the minimum size of the central zone (d_1) was kept constant at 1 cm during line decomposition. Ultimately, 3D solid hold-up profiles are plotted at seven heights combining the jet widths obtained from this simulation and local solid hold-up values obtained from Eq. 5.9 (Fig. 5.7, 5.8). These figures reveal the locations at which the solid hold-up is reduced and/or increased by the microjet. At U_{mf} (and $U_j = 0$ m s^{-1}), solid hold up is increased near to the bottom of the bed, while it becomes more diluted at higher levels. At the highest level (15 cm above the distributor, the splash zone), the solid concentration is almost zero as the bed has not yet fully expanded. By turning on the jet to $U_j = 33$ m s^{-1} (Fig. 5.7b), the solid hold-up reduces close to the distributor because part of the bed is being carried by the microjet flow. Moreover, a very low solid concentration zone is being formed at 2.5 mm above the tip of the nozzle, due to the injection of the secondary gas flow. However, the jet penetration length is not sufficient to affect the local solid hold-up at higher levels. By increasing the jet velocity to $U_j = 100$ and 200 m s^{-1} (Fig. 5.7c,d), the solid hold-up in the center noticeably reduces not only at the jet level, but even at higher levels since the jet penetration length rises. At the maximum jet velocity ($U_j = 200$ m s^{-1}), the total flow (i.e. fluidizing gas and microjet flow) is high enough to expand the bed to the level of measurement. Also, at all jet velocities, a concentrated zone is identified right under the jet, which indicates formation of a dead-zone under the microjet tube.
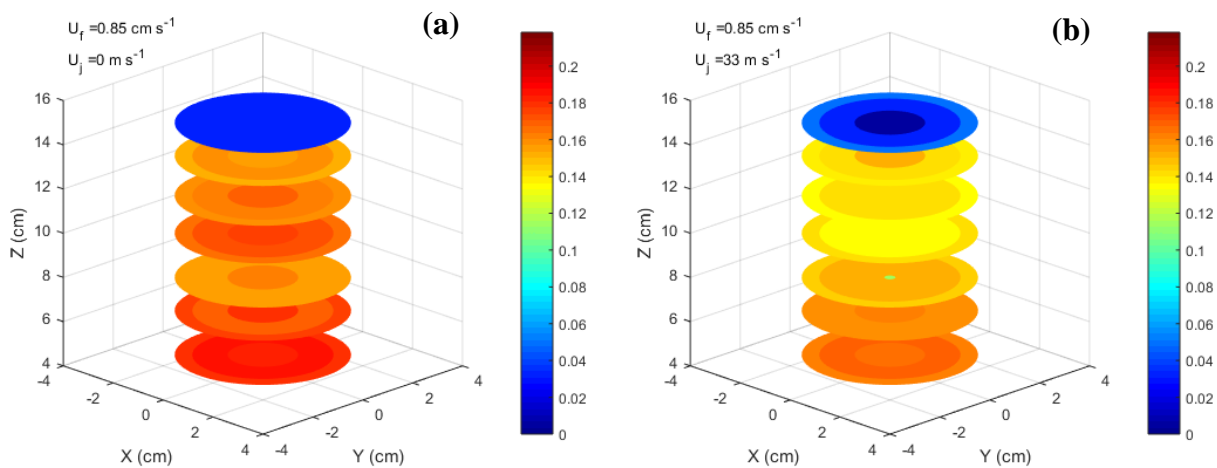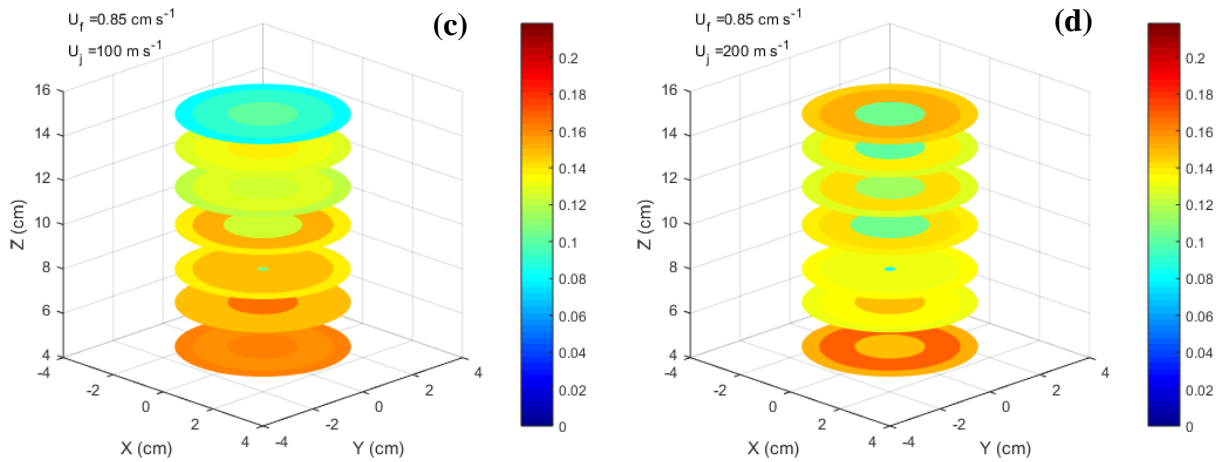
Figure 5.7 (a) 3D local solid hold-up profiles at seven cross sections calculated by line-decomposition approach at $U_{mf} = 0.85$ cm s^{-1}, $U_j = 0$; (b) $U_j = 33$ m s^{-1}; (c) $U_j = 100$ m s^{-1}; (d) $U_j = 200$ m s^{-1}

By changing the fluidization regime to bubbling ($U_f = 2.55$ cm s^{-1}) (Fig. 5.8), the axial solid diffusivity enhances so the solid hold-up through the bed is more homogeneous compared to the minimum fluidization regime. Ettehadieh et al. [40] previously showed a centimeter-sized jet makes the axial solid hold-up uniform for Geldart D particles by increasing the solid diffusivity in this direction. However, since the radial solid diffusivity is constant for small bed diameters [41], the bed remains almost uniform in the radial directions at all gas velocities. In this regime, the general patterns of solid hold-up variations identified at U_{mf} remain, but at proportionally lower solid hold-up values as a result of introducing more fluidizing gas to the system. At this increased fluidization velocity, jet effects are reduced (Fig. 5.7 vs. Fig. 5.8). In the bubbling regime, the dilute zone in the jet is no longer detectable at low U_j (Fig. 5.8b), while it starts developing by increasing U_j to 100 and 200 m s^{-1} (Fig. 5.8c,d). However, the jet penetration length at $U_j = 100$ m s^{-1} is still too short to influence the local solid hold-up at higher levels. Eventually, at $U_j = 200$ m s^{-1} (20 v% of the fluidizing gas flow), the maximum jet penetration length increases. Thus, discharged bubbles from the jet can travel further and consequently reduce the local solid hold-up at higher levels (Fig. 5.8d).

In a broader view, these solid hold-up profiles clarify how, in both regimes, the microjet improves the fluidization quality of nanoparticles and affects the solid hold-up distribution throughout the

bed, despite their local inhomogeneities. This is essential since it enhances mass and heat transfer performance inside fluidized beds. Comparing the local solid hold-up profiles when the jet is off and on (Fig. 5.7a,b and Fig. 5.8a,b) indicates the axial distributions of solid particles have been enhanced. This occurs as a result of overcoming interparticle forces, which in turn leads to breakage of nanoparticle agglomerates [14, 22] and increased total gas flow. The higher the jet momentum, the higher the axial solid diffusivity, and thus the enhanced homogeneity in the bed. While this was expected intuitively, the improved gamma densitometry technique has tangibly demonstrated and quantified local solid hold-up, showing how a given constant local phenomenon (such as a jet) can directly impact solid/gas phase distribution.
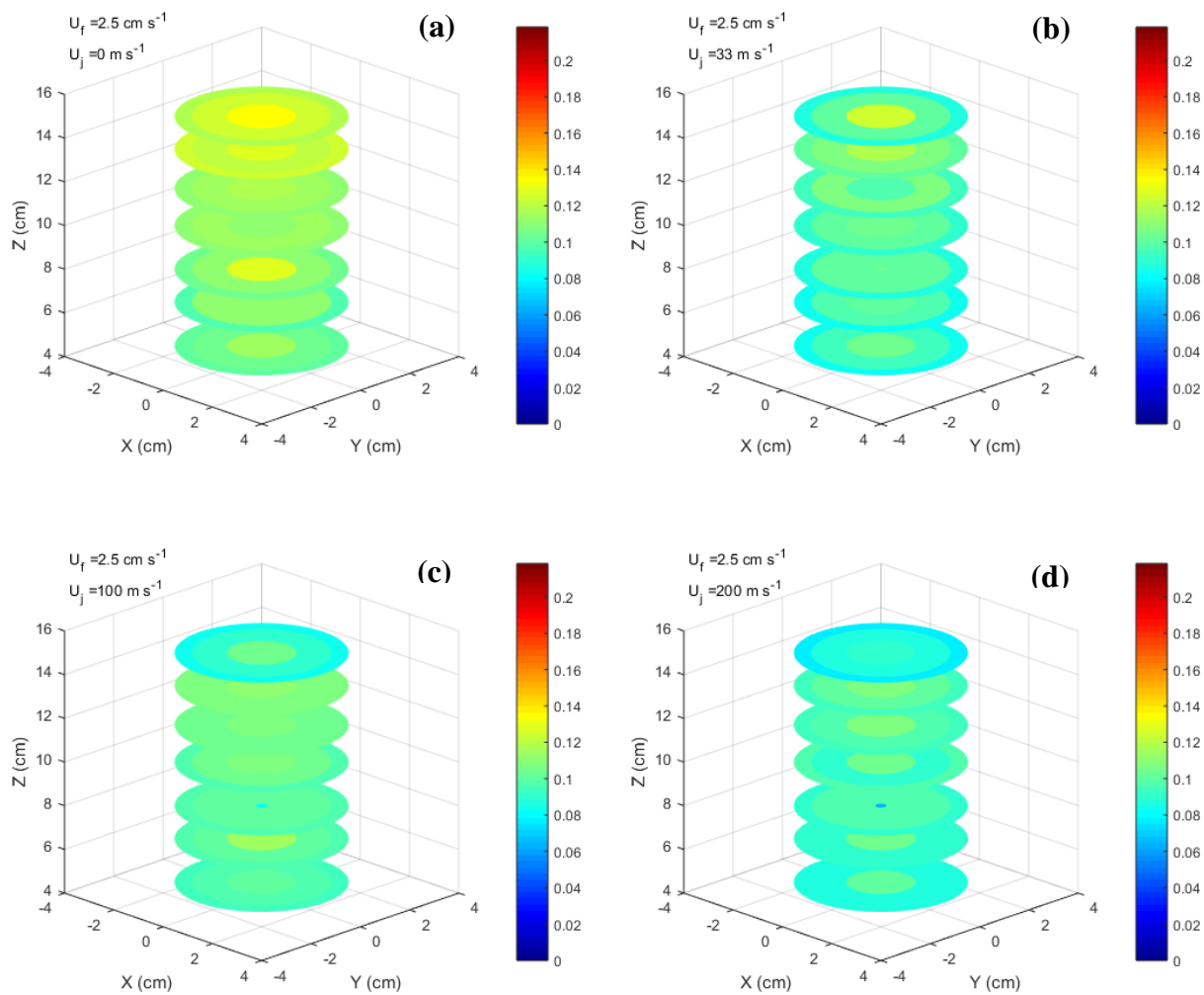
Figure 5.8 3D local solid hold-up profiles at seven cross sections calculated by line-decomposition approach at $U_f = 2.5$ cm s^{-1}. (a) $U_j = 0$ m s^{-1}; (b) $U_j = 33$ m s^{-1}; (c) $U_j = 100$ m s^{-}1; (d) $U_j = 200$ m s^{-1}

5.4.4 Optimizing the jet-to-impactor distance

5.4.4.1 Solid hold-up along the jet axis

The determination of local solid hold-up values (ε_l) along the jet axis at $U_j = 100$ m/s and $U_f = 2.5$ cm/s^1 was made possible by the line decomposition approach presented in the previous section. Fig. 9a illustrates that solid hold-up increases sharply from the nozzle tip (where particle hold-up is zero) up to 7.8% at 0.0025 m above the nozzle tip. At ca. 0.02 m above the tip, it has reached its final value of approximately 10.5%. This is in general agreement with the jet length values calculated by Hirsan [24] (Table 5.3), that show that, at $U_j = 100$ m s^{-1}, the JAZ extends to 0.0011 m (up to 0.0062 m). After this JAZ, the jet loses its form and turns into high-momentum bubbles. In the early section of the JAZ, solid particles are dragged into the jet stream as a result of negative pressure generated via the high-speed jet. Moving away from the tip, more and more particles are entrained into the jet flow until the end of JAZ is reached, at which point solid hold-up remains constant as the jet no longer affect the solid distribution in the bed.
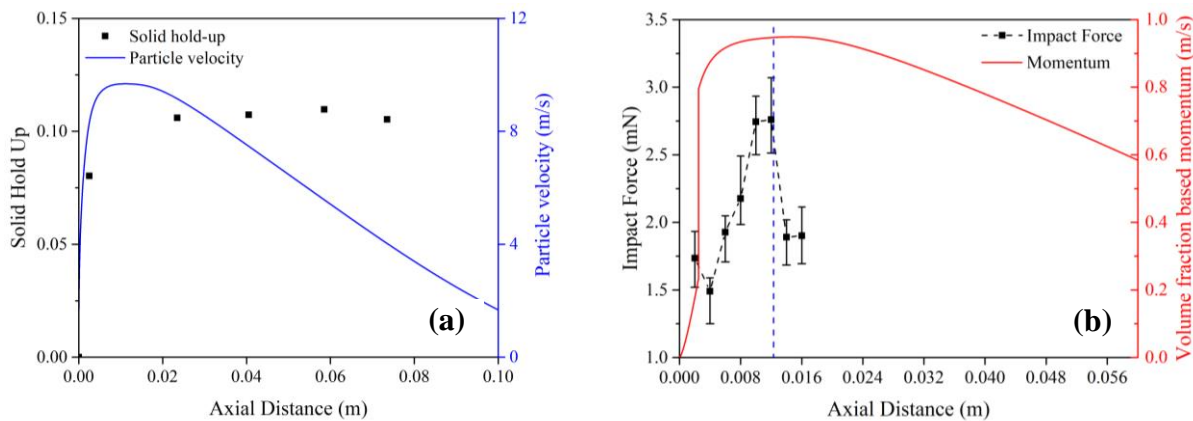
Figure 5.9 (a) local solid hold-up profile as a function of axial distance to the jet tip (black data points) and velocity of particles with the average size of 70 μm (blue curve); (b) Impact force

profile (black data points, error bars show the absolute error) and momentum profile of impacted particles as a function of axial distance to the jet tip

5.4.4.2   Particle velocity

The velocity of fluidized particles in the vicinity of the high-velocity jet was obtained by a two-way coupling simulation using the Fluent 6.3 CFD software (same geometry as simulations used to calculate jet width in the previous section). The fluidized particles were considered as nanoparticle agglomerates with a diameter of 70 μm. k-ε turbulent model was used in combination with wall functions for the continuous gas phase. For the dispersed phase, particle motion is obtained by integrating the force balance. To simplify, only three hydrodynamic forces were considered (drag, buoyancy and gravitational forces) and were written in a Lagrangian frame on the particles. In the set of differential equations that calculate particle velocities and positions, heat and mass transfer are neglected, and particles are assumed to be spherical. In a two-way approach, the velocity field calculated via the Reynolds-averaged Navier–Stokes (RANS) equations is used to solve dispersed phase motion equations. The calculated dispersed phase momentum is then used to update the velocity field of the continuous phase. However, particle-particle interactions are neglected. After solving the equations, a mesh and particle study was performed to ascertain that the injection point of particles and the mesh size did not affect the solution of the model (Fig. 5.S3-S5).

Fig. 5.9a (blue curve) shows the velocity of particles that were entrained and accelerated by the jet flow. The particles rapidly accelerate from their initial fluidization velocity of 2.5 cm s^{-1} and reach their maximum value (10 m s^{-1}) approximately 0.012 m from the tip of the nozzle. The particles then gradually slow down under the effect of gravity until they reach the superficial velocity in the column. Combining the solid hold-up and velocity yields the particle momentum curve (Fig. 5.9b, red), which reaches its apex at approximately 0.012 m above the tip of the nozzle. Thus, for $U_j =$ 100 m s^{-1} and $U_f = 2.5$ cm s^{-1}, this is the optimum point to place an impactor in a jet-impactor system. Extending beyond this specific case, the general rule of thumb would be:

- If the jet penetration length is smaller than the point at which maximum particle velocity is reached, the jet penetration length can be retained as the optimal position to install an impactor;

- If the jet penetration length is greater than the point at which maximum particle velocity is reached, the point of maximum particle velocity can be retained as the optimal position for an impactor.

5.4.4.3 Force measurement tests

To validate the impactor position recommendation (0.012 m), the local force resulting from the impact of jet flow and accelerated particles on the impactor was measured at different jet-to-impactor distances. For this purpose, a force sensor was placed within the bed, perpendicular to the jet flow.
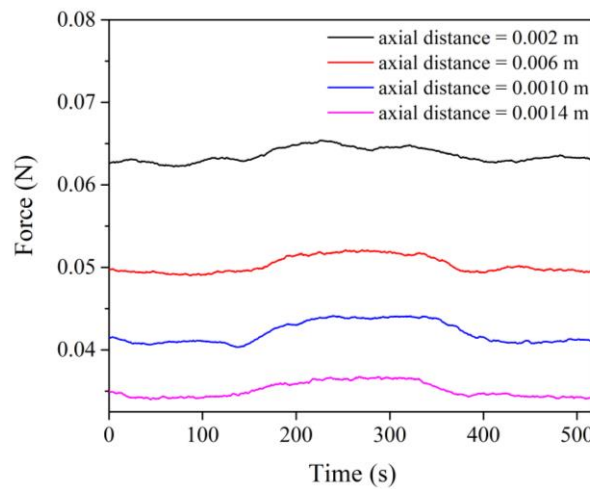
Figure 5.10 force signals measured via force sensor at four different axial distances to the jet tip at $U_f = 2.5$ cm s^{-1} and $U_j = 100$ m s^{-1}

Fig. 5.10 illustrates the force signals recorded at $U_f = 2.5$ cm s^{-1} and $U_j = 100$ m s^{-1} at axial distances of 2, 6, 10 and 14 mm from the jet. The values shown result from the application of a moving average filter with a window size of 20 seconds. The raw signal, noisy from random high

frequency collisions, is provided in supplementary information. The force difference between sections where $U_j = 0$ and $U_j = 100$ m s^{-1} is considered as the force applied by the jet flow (F_j).

By measuring F_j at eight different axial distances, the jet flow force profile is obtained (Fig. 5.9b). In agreement with the overlaid momentum curve, F_j increases in the axial direction and reaches its maximum ca. 0.012 m from the tip of the nozzle.

5.5 Concluding Remarks

The influence of a microjet and microjet-impactor on the fluidization of Fe_2O_3 nanopowder under two fluidization regimes (minimum fluidization and bubbling) and a wide range of jet velocities (0-200 m s^{-1}) was studied using gamma densitometry, and compared with conventional fluidization. In conventional fluidization, a uniform radial solid phase distribution was observed, which was more concentrated at the bottom of the bed. By increasing the jet velocity, the solid hold-up locally drops more and more at the center, forming the JAZ. Adding an impactor against the jet changes the previous symmetric profile to an asymmetric profile due to gas reflection and the impedance of gas by the side-arm mount of the impactor.

To spotlight the JAZ, a line-decomposition approach was proposed to reconstruct the 3D local solid hold-up profile based on the radial solid hold-up values. Local solid hold-up maps showed that, under the minimum fluidization regime, solids are not well distributed axially, while this becomes more homogeneous in transition to the bubbling regime. However, increasing the jet velocity at a given regime locally varies the solid phase distribution along the jet axis as a result of injecting extra gas and causes local inhomogeneities. Further, increasing the fluidizing gas velocity diminishes the jet effect, likely by reducing the jet length.

Finally, the local solid hold-up profile along the jet axis was combined with a particle velocity profile, provided by a two-way CFD simulation, to optimize the jet-to-impactor distance and thus maximize the impact momentum. The highest momentum point occurs at 0.012 m above the tip of the nozzle for $U_f = 2.5$ cm s^{-1} and $U_j = 100$ m s^{-1}. This optimum point was then validated experimentally using local force measurements along the jet axis.

This study provides insights for the proper design and scale-up of the jet-assisted fluidized bed reactors particularly for nanopowders, including cases where an impactor is used. Further, it

provides a methodology for subsequent solid hold-up tests (detailing an improved gamma densitometry technique in supplementary information, and a new line deconvolution approach), and provides guideline to maximize the impact momentum when agglomerate breakage is required.

5.6 Acknowledgments

5.7 Supplementary Materials

5.7.1 Improving Gamma Densitometry Measurements

To ensure the error of measurements using a gamma densitometer remains within an acceptable range, the sampling time, total recording time, and source activity were improved through the following study before the measurements were taken in the fluidized bed.

5.7.2 Sampling Time

Three factors are important in selecting the sampling time: dynamic rate of the system, nonlinear averaging error, and signal-to-noise ratio of the count signals. The sampling time of the counted photons must be sufficiently short to be able to detect the hydrodynamic changes in the system. For example, to measure a 1 cm bubble travelling at a velocity of 1 m/s, a temporal resolution of 0.01 s is required. On the other hand, nonlinear averaging error (due to the Poisson nature of the photon generation process) and finite source activity (that determines the intensity of the signals) increase the required sampling time. In this situation, the Nyquist frequency determines the lower bound of the sampling time spectrum at which the signal power is still distinguishable from noise [1]. Therefore, to determine the sampling time, the autocorrelation function of a raw signal was plotted against the time, and the maximum sampling time was selected as half the Nyquist

frequency. Accordingly, based on a Nyquist frequency of 100 ms and dynamic rate of the fluidized bed, a sampling time of 10 ms was selected for all experiments (Fig. 5.S1).
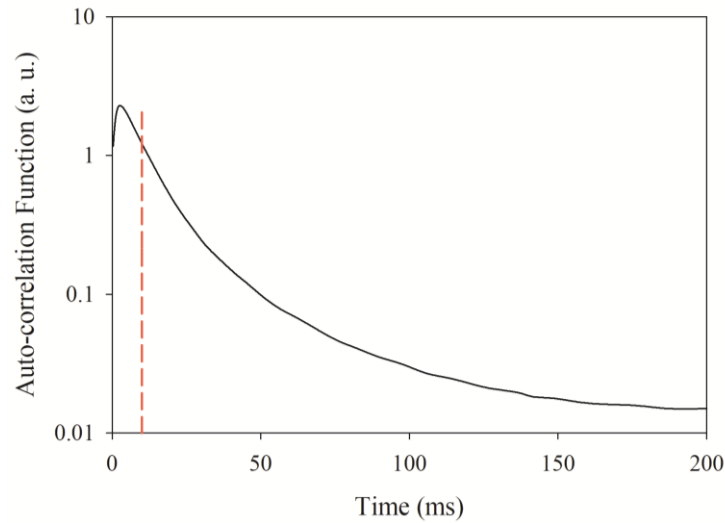
Figure 5.S1 Auto-correlation function of a sample signal in time domain with 10 ms sampling time

5.7.3 Source Activity and Total Scan Time

As radioactive decay is a random process, the count signal generated by a radioactive source is itself random. This introduces the error of determination since there is not a "true" count rate; a sufficient number of data points must be collected for each measurement to ensure that the average counts in the short period of the experiment leads to a reproducible solid hold-up value. To determine this, the count rates for a large number of data were recorded and considered as the "true average count rate". Accordingly, solid hold-up was defined as:

$$\varepsilon_s(t) = \left| \frac{\ln \frac{\bar{C}_f}{\bar{C}(t)}}{\mu_p D} \right| \qquad \text{(Equation 5.S1)}$$

where $\bar{C}_f$ and $\bar{C}(t)$ are the cumulative average of the count number at the final time of 10 min (the true average count rate) and at time t, respectively. The deviation of ε_s values from zero indicates the error of solid hold-up arises from decay randomness. Using that, the effect of the activity of the

gamma-ray source and the total scan time on the solid hold-up value were studied by measuring the count rate of the empty bed at a given point at a constant sampling time of 10 ms.

For this purpose, the count numbers were collected every 12 s for total scan time of 10 minutes. The solid hold-up error was calculated based on the cumulative average at the end of each 12-second period and were plotted over total scan time (Fig. 5.S2). Increasing the collected data reduces the solid hold-up error arising from the randomness of the gamma-ray count signals. Recording data for more than five minutes diminishes the solid hold-up error to less than one percent.

The experiment was repeated for other positions to ensure that the results were independent of the measured point. To keep the solid hold-up error as low as 0.1%, the highest activity source (450 μCi) is retained for subsequent experiments and a total scan time of two minutes was selected.
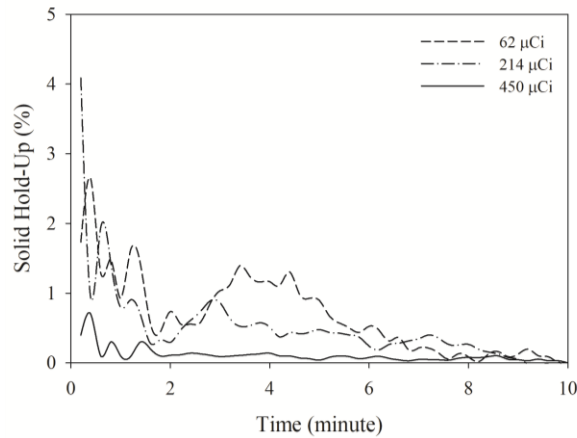
Figure 5.S2 Solid hold-up calculated based on the cumulative average of count rate versus scan time at various particle activities

5.7.4 Mesh and particle study

In order to ascertain the particle injection point and the mesh size did not affect the model, we performed different simulations with different mesh sizes, particularly local mesh size in the vicinity of the jet, and compared the velocity profiles along the jet axis. Fig. 5.S3 and 5.S4 show triangular mesh and corresponding velocity profiles, respectively.
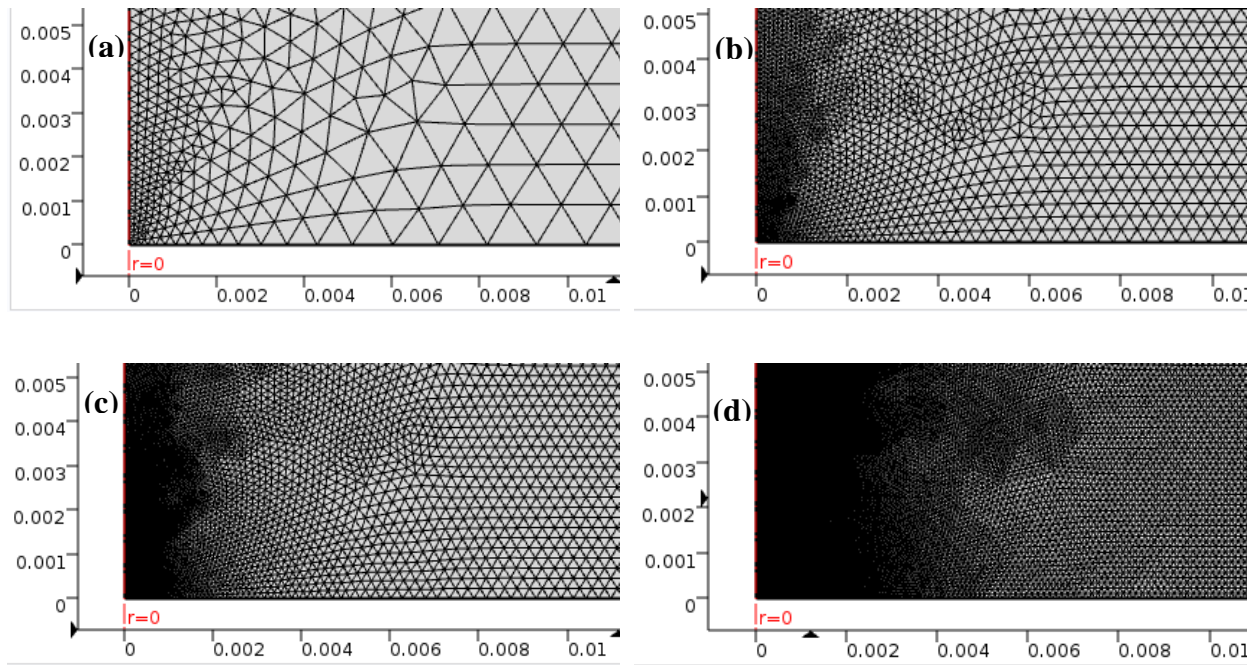
Figure 5.S3 Mesh refinement study and its effect on the velocity field profile in four refinement levels (RL): (a) RL-1; (b) RL-2; (c) RL-3; (d) RL-4.
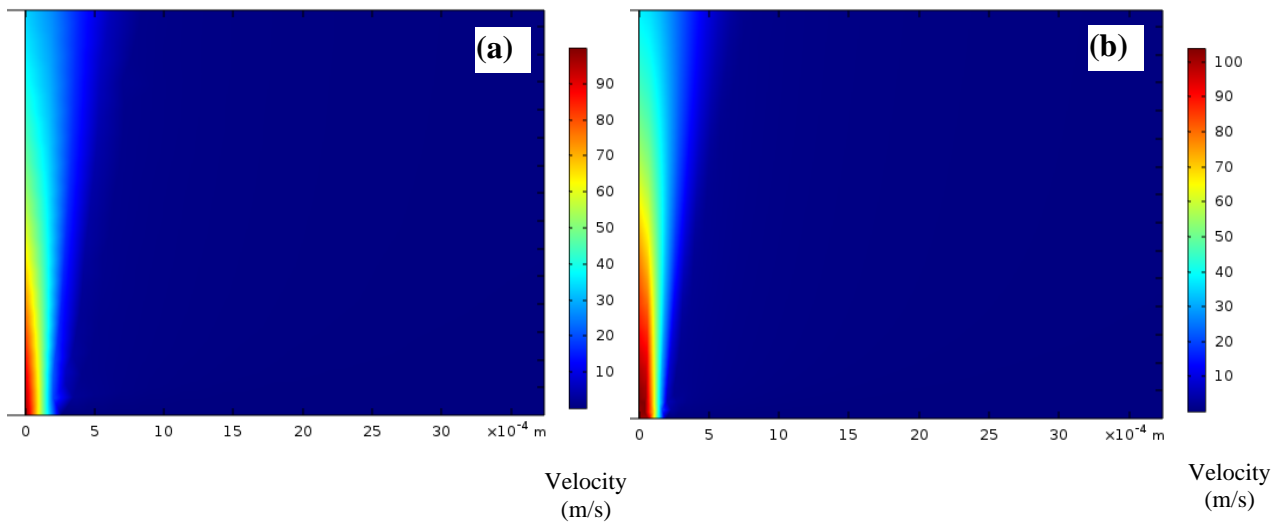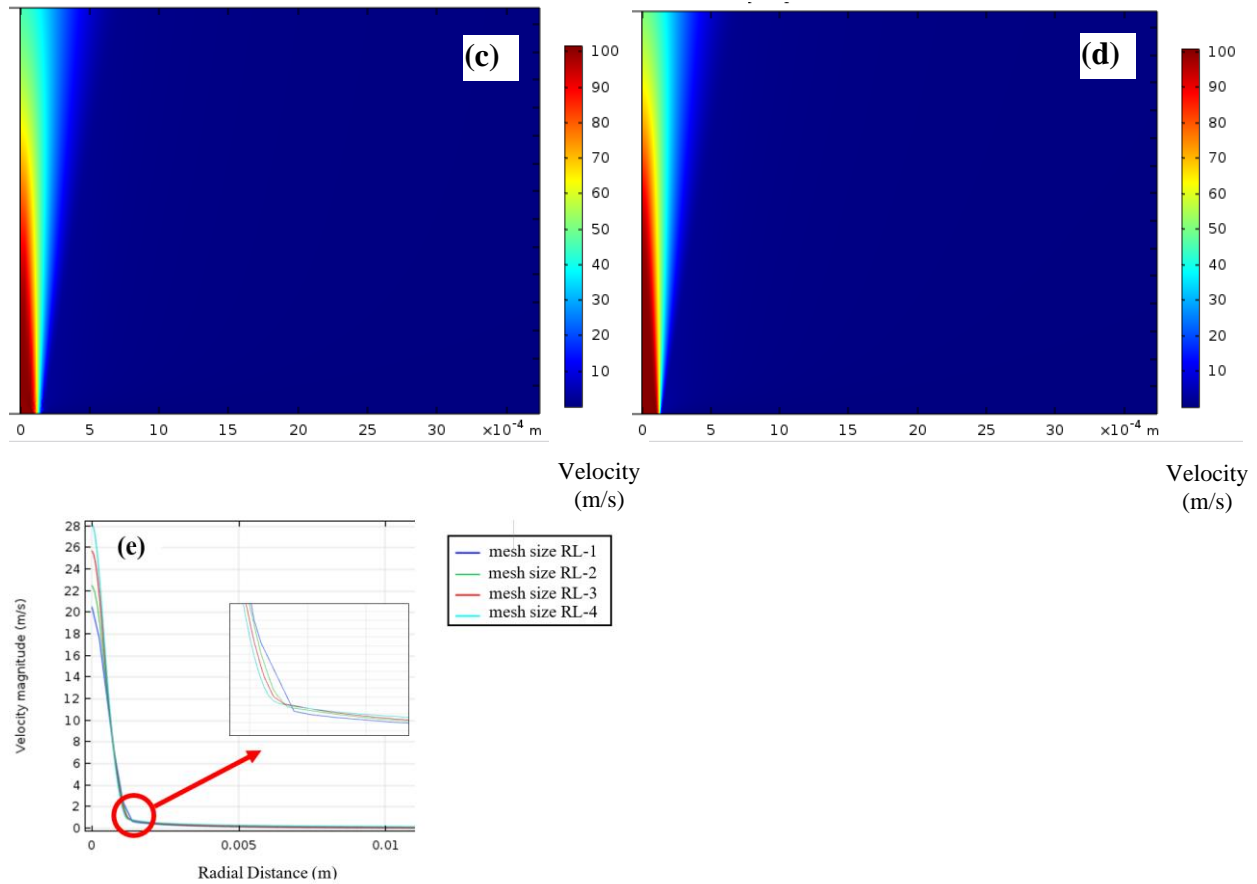
Figure 5.S4 2D velocity profile of the jet corresponding with mesh size of Figure S3 (jet velocity of 100 m s^{-1}) and (e) jet velocity profile perpendicular to the jet axis at y = 0.005 m above the tip

Fig. 5.S4e indicates by refining the mesh down to minimum element size of 15×10^{-6} m and increasing the number of elements up to 886,000, the variations in the velocity profiles become negligible. Therefore, the finest mesh was retained for the rest simulation.

After establishing the gas phase simulation parameters, a set of simulations was run for the purpose of particle study, considering the position of injected particulate samples. To do so, three injection lines were defined with length of R, 0.1R, and 0.01R, starting from the point where the boundary line of the jet ends (the radius of the bed R = 0.025 m). The initial velocity of particles was assumed to be equal to fluidizing gas (U_f = 2.5 cm s^{-1}) and particle size was selected as 70 μm. Maximum number of particles (1000) was injected rom each injection line. Fig. S5 shows velocity profiles of all particles, that were accelerated by the jet, along the jet axis for all three injection lines. The

squares show the apex of each profile. Comparing the peaks clearly shows that all maximum points occurs at the same axial distance from the jet tip, confirming the maximum velocity is independent of the injection point.
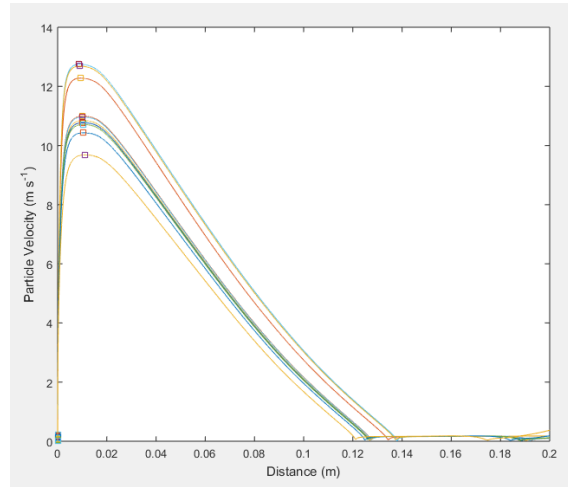
Figure 5.S5 Velocity profiles of particles injected from three injection lines with length of R, 0.1R, and 0.01R along the jet axis (for particle size 70 μm, $U_f = 2.5$ cm s^{-1}, and $U_j = 100$ m s^{-1}). Each color represents velocity profile of one single injected particle (286 overlaid profiles).

5.7.5 Calibration curve of force sensor
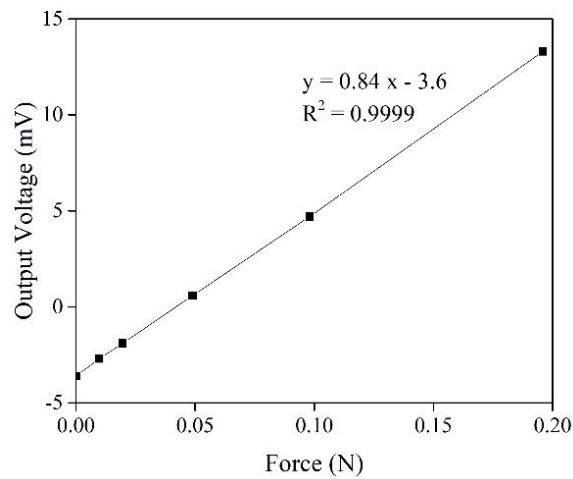
Figure 5.S6 Calibration curve of force sensor

5.8 Literature Cited

[1] S. Pradhan, J. Hedberg, E. Blomberg, S. Wold, I. Odnevall Wallinder, Effect of sonication on particle dispersion, administered dose and metal release of non-functionalized, non-inert metal nanoparticles, J. Nanopart. Res., 18 (2016) 285.

[2] V.S. Nguyen, D. Rouxel, R. Hadji, B. Vincent, Y. Fort, Effect of ultrasonication and dispersion stability on the cluster size of alumina nanoscale particles in aqueous solutions, Ultrason. Sonochem., 18 (2011) 382-388.

[3] H. Yoden, N. Itoh, Effect of Small Size Beads on Dispersion of Nanometer-Sized Silica Particle by Wet Beads Mill Process, Journal of the Society of Powder Technology, Japan, 41 (2004) 457-464.

[4] M. Inkyo, T. Tahara, Dispersion of Agglomerated Nanoparticles by Fine Beads Mill, Journal of the Society of Powder Technology, Japan, 41 (2004) 578-585.

[5] Y. Hwang, J.-K. Lee, J.-K. Lee, Y.-M. Jeong, S.-i. Cheong, Y.-C. Ahn, S.H. Kim, Production and dispersion stability of nanoparticles in nanofluids, Powder Technol., 186 (2008) 145-153.

[6] J.A. Kurkela, D.P. Brown, J. Raula, E.I. Kauppinen, New apparatus for studying powder deagglomeration, Powder Technol., 180 (2008) 164-171.

[7] M. Seipenbusch, P. Toneva, W. Peukert, A.P. Weber, Impact Fragmentation of Metal Nanoparticle Agglomerates, Particle & Particle Systems Characterization, 24 (2007) 193-200.

[8] W.H. Finlay, The mechanics of inhaled pharmaceutical aerosols: an introduction, Academic press2001.

[9] C.A. Dunber, A.J. Hickey, P. Holzner, Dispersion and Characterization of Pharmaceutical Dry Powder Aerosols, KONA Powder and Particle Journal, 16 (1998) 7-45.

[10] A. Gianfrancesco, C. Turchiuli, E. Dumoulin, Powder agglomeration during the spray-drying process: measurements of air properties, Dairy Science and Technology, 88 (2008) 53-64.

[11] Y. Ding, B. Stahlmecke, A.S. Jiménez, I.L. Tuinman, H. Kaminski, T.A.J. Kuhlbusch, M. van Tongeren, M. Riediker, Dustiness and Deagglomeration Testing: Interlaboratory Comparison of Systems for Nanoparticle Powders, Aerosol Sci. Technol., 49 (2015) 1222-1231.

[12] J.A. Quevedo, A. Omosebi, R. Pfeffer, Fluidization enhancement of agglomerates of metal oxide nanopowders by microjets, AlChE J., 56 (2010) 1456-1468.

[13] R. Hong, J. Ding, H. Li, Fluidization of fine powders in fluidized beds with an upward or a downward air jet, China Particuology, 3 (2005) 181-186.

[14] R.P.J.A.Q.J. Flesch, Fluidized bed systems and methods including micro-jet flow, in: UPPTO (Ed.)USA, 2008.

[15] J. McMillan, C. Briens, F. Berruti, E. Chan, High velocity attrition nozzles in fluidized beds, Powder Technol., 175 (2007) 133-141.

[16] L. Chen, H. Weinstein, Shape and extent of the void formed by a horizontal jet in a fluidized bed, AlChE J., 39 (1993) 1901-1909.

[17] H. Nasri Lari, J. Chaouki, J.R. Tavares, De-agglomeration of nanoparticles in a jet impactor-assisted fluidized bed, Powder Technol., 316 (2017) 455-461.

[18] R.P. J. Ruud van Ommen, Fluidization of nanopowders: experiments, modeling, and applications, (December 2010).

[19] Z. Shen, C.L. Briens, M. Kwauk, M.A. Bergougnou, Study of a downward gas jet in a two-dimensional fluidized bed, The Canadian Journal of Chemical Engineering, 68 (1990) 534-540.

[20] Z. Shen, C.L. Briens, M.A. Bergougnou, M. Kwauk, Study of a downward grid jet in a large two-dimensional gas-fluidized bed, Powder Technol., 62 (1990) 227-234.

[21] J.A. Quevedo, R. Pfeffer, In Situ Measurements of Gas Fluidized Nanoagglomerates, Industrial & Engineering Chemistry Research, 49 (2010) 5263-5269.

[22] D.M.K. J. Ruud van Ommen, Alan Weimer, Robert Pfeffer, Berend van Wachem, Experiments and modelling of micro-jet assisted fluidization of nanoparticles, (2010).

[23] B. Esmaeili, J. Chaouki, C. Dubois, An evaluation of the solid hold-up distribution in a fluidized bed of nanoparticles using radioactive densitometry and fibre optics, The Canadian Journal of Chemical Engineering, 86 (2008) 543-552.

[24] M. Rasouli, O. Dubé, F. Bertrand, J. Chaouki, Investigating the dynamics of cylindrical particles in a rotating drum using multiple radioactive particle tracking, AlChE J., 62 (2016) 2622-2634.

[25] R.F. Mudde, W.K. Harteveld, H.E.A.v.d. Akker, T.H.J.J.v.d. Hagen, H.v. Dam, Gamma radiation densitometry for studying the dynamics of fluidized beds, Chem. Eng. Sci., 54 (1999) 2047-2054.

[26] B. Koeninger, T. Hensler, S. Schug, W. Arlt, K.-E. Wirth, Horizontal secondary gas injection in fluidized beds: Solid concentration and velocity in multiphase jets, Powder Technol., 316 (2017) 49-58.

[27] A. Efhaima, M.H. Al-Dahhan, Local time-averaged gas holdup in fluidized bed reactor using gamma ray computed tomography technique (CT), International Journal of Industrial Chemistry, 6 (2015) 143-152.

[28] V. Jiradilok, D. Gidaspow, J. Kalra, S. Damronglerd, S. Nitivattananon, Explosive dissemination and flow of nanoparticles, Powder Technol., 164 (2006) 33-49.

[29] H. Nasri Lari, J. Chaouki, J.R. Tavares, Continuous aerosol photopolymerization to coat de-agglomerated nanoparticles, Chem. Eng. J., 390 (2020) 124526.

[30] G.F. Knoll, Radiation Detection and Measurement, Wiley, Hoboken, N.J., 2010.

[31] W.C. Yang, Handbook of Fluidization and Fluid-Particle Systems, Taylor & Francis2003.

[32] D.A.A.d. Vasconcelos;, M.M. Hamada;, C.H. Mesquita;, C.C. Dantas;, R. Narain;, S.B. Melo;, V.A.d. Santos, Collimator design for single beam gamma ray industrial tomography and fan beam geometry, International Nuclear Atlantic Conference - INAC 2011Belo Horizonte, MG, Brazil, 2011.

[33] C.C. Xu, J. Zhu, Prediction of the Minimum Fluidization Velocity for Fine Particles of Various Degrees of Cohesiveness, Chem. Eng. Commun., 196 (2008) 499-517.

[34] W. Yao, G. Guangsheng, W. Fei, W. Jun, Fluidization and agglomerate structure of SiO2 nanoparticles, Powder Technol., 124 (2002) 152-159.

[35] C. Zhu, Q. Yu, R.N. Dave, R. Pfeffer, Gas fluidization characteristics of nanoparticle agglomerates, AlChE J., 51 (2005) 426-439.

[36] I. Hirsan, C. Sishtla, T.M. Knowlton, Effect of bed and jet parameters on vertical jet penetration length in gas fluidized beds, 73. annual meeting of the American Institute of Chemical EngineersChicago, IL, USA, 1980.

[37] T.M. Knowlton, I. Hirsan, The Effect of Pressure on Jet Penetration in Semi-Cylindrical Gas-Fluidized Beds, (1980) 315-324.

[38] C.-h. Wang, Z.-p. Zhong, R. Li, J.-q. E, Prediction of jet penetration depth based on least square support vector machine, Powder Technol., 203 (2010) 404-411.

[39] C.S. Chyang, C.H. Chang, J.H. Chang, Gas discharge modes at a single horizontal nozzle in a two-dimensional fluidized bed, Powder Technol., 90 (1997) 71-77.

[40] B. Ettehadieh, D. Gidaspow, R.W. Lyczkowski, Hydrodynamics of fluidization in a semicircular bed with a jet, AlChE J., 30 (1984) 529-536.

[41] A. Efhaima, M.H. Al-Dahhan, Bed diameter effect on the hydrodynamics of gas-solid fluidized beds via radioactive particle tracking (RPT) technique, The Canadian Journal of Chemical Engineering, 95 (2017) 744-756.

CHAPTER 6   ARTICLE 3: CONTINUOUS AEROSOL PHOTOPOLYMERIZATION TO COAT DE-AGGLOMERATED NANOPARTICLES

Hamed Nasri Lari, Jamal Chaouki, Jason R. Tavares

Department of Chemical Engineering, École Polytechnique de Montréal, P.O. Box 6079, Station Centre-Ville, Montreal, Quebec, H3C 3A7, Canada

Graphical Abstract
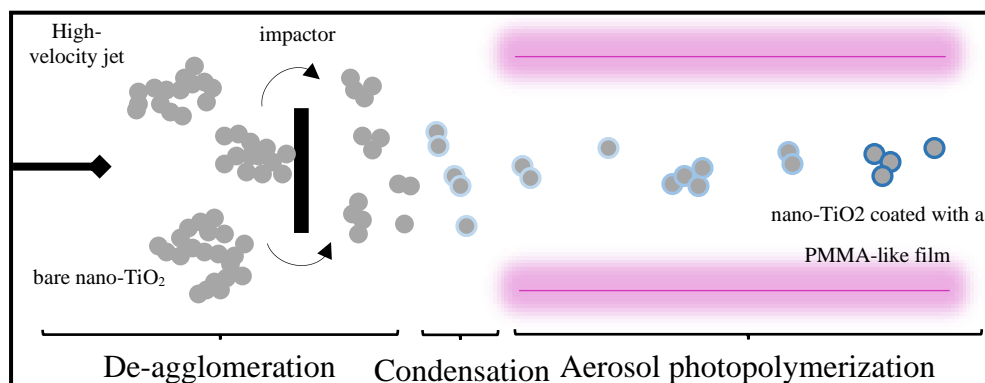
Highlights

- De-agglomerated nano-TiO$_2$ was coated with PMMA-like film using aerosol photopolymerization.
- Presence of a PMMA-like film was confirmed by TEM, TGA, FTIR and XPS.
- Jet impactor-assisted fluidized bed reduces the size of nano-TiO$_2$ agglomerates.
- Coated nano-TiO$_2$ showed an enhanced long-term dispersibility in non-polar media.

Abstract

A novel continuous aerosol photopolymerization technique to coat nanoparticles that have been previously de-agglomerated is presented. After de-agglomeration in a jet-impactor assisted fluidized bed, monomer vapors are condensed onto the surface of aerosol nanoparticles via heterogeneous condensation. Photopolymerization is initiated through exposure to UV light. To demonstrate the process, titanium dioxide (TiO$_2$) and methyl methacrylate (MMA) were selected as nanoparticle and organic monomer, respectively. We demonstrated this light-based technique, operated at ambient pressure and room temperature, is able to graft a PMMA-like film with a thickness of 1.5 nm on the surface of nanoparticles, confirmed by TEM and FTIR. XPS analysis confirmed formation of covalent bonds with the TiO$_2$ surface, indicating a surface-initiated photopolymerization. Particle size measurements in suspension state illustrated the efficiency of the de-agglomeration and subsequent coating process, as coated particles remained smaller than bare particles. UV-Vis absorbance spectra show that the coating facilitates dispersion in non-polar

solvents. Finally, long-term stability experiment confirmed the suspension stability is enhanced not only because of the reduction of agglomerate sizes, but also as a result of the organic coating which improves the interfacial interactions between particle-particle and particle-solvent. This technique can be easily combined with any continuous inorganic nanoparticle synthesis processes as a solvent-free post-synthesis process to impart a functional coating.

Keywords nanoparticle, coating, aerosol, photopolymerization, continuous, Photo-initiated Chemical Vapor Deposition (PICVD)

6.1 Introduction

Inorganic nanoparticles are among the most widely studied nanomaterials given their uses in a broad range of fields such as electronic, catalysis, drug delivery, sensors, cosmetics, pharmaceutical equipment, and air/water remediation. Tailoring nanoparticles for specific applications through their surface treatment has been the focus of vast research in the past two decades [1-7].

Bare metal and metal oxide nanoparticles tend to agglomerate or aggregate during their synthesis, storage or processing as a result of their high surface energy and exceedingly high interparticle forces (e.g. van der Waals forces). Traditionally, surfactants are used to prevent the agglomeration of nanoparticles and to improve their dispersibility through different mechanisms such as steric stabilization, electrostatic stabilization, or passivation. Despite the efficiency of surfactants, they suffer from poor thermal stability [8]. This inhibits their application in high temperature processes such as nanofluids, nanocomposites and thermoset polymers [9, 10]. To overcome this issue, coating or passivating nanoparticles is of key importance to facilitate their handling, whilst retaining their unique, size-driven properties. On top of reducing surface energy through passivation, coating allows us to tune surface properties for specific applications. For example, coating can enhance dispersion, which is a key factor in the production of nanocomposites. Poor performance in polymer nanocomposites has been directly related to weak polymer-nanoparticle interaction, as compared to strong particle-particle interactions that drive agglomeration [11].

Nanoparticle surface functionalization with chemical groups that have affinity to the host media (e.g. polymer matrix) has shown promise in multiple fields: encapsulation of iron oxide

nanoparticles with carbon chains enhances dispersion in non-polar media [1], encapsulating zirconia and alumina nanoparticles with high molecular weight polyethylene enhances the performance of nanocomposites [12], coating silver nanoparticle with polyacrylic acid improves the preparation of silver-polymer nanocomposites [13], functionalizing hydrophobic nanoparticles with amphiphilic polymers make them compatible with biological application [14], and chemical modification of graphite nanoplates with 1,3 dipolar cycloaddition enhanced the stability of dispersion and delayed re-agglomeration in polypropylene matrix [15], to name only a few.

Traditionally, nanoparticle coating methods are categorized into wet and dry techniques. Wet methods include sol-gel, emulsification, and solvent evaporation processes [16]. Dry methods consist of physical (physical vapor deposition) and chemical (plasma-enhanced [17], thermally-activated [18], and photo-initiated chemical vapor deposition [19-21]) approaches. Physical methods coat a surface without forming of covalent bonds with the substrate, whereas chemical approaches promote bonding with free sites on the nanoparticle surface via strong covalent bonds. While several solvent-free methods have been developed, few continuous processes are available [17, 22-27]:

- Wang et al. [22] used supercritical CO_2 as a solvent-free technique to physically encapsulate silica nanoparticles with Eudragit (polymethacrylate-based copolymers). Flashing the nanoparticle-polymer-supercritical CO_2 suspension from 32 °C and 8.27 MPa to ambient temperature and atmospheric pressure causes a heterogeneous polymer nucleation with the nanoparticles acting as nuclei and a subsequent growth of polymer on the surface of the nanoparticles.

- Poostforooshan et al. [23] achieved a carbon shell coating using aerosol polymerization via heterogenous condensation of both monomer and initiator on the surface of nanoparticles.

- Pfeiffer et al. [24] coated metal nanoparticles using a continuous PVD system. In this technique, an aerosol of freshly-generated core particles was passed through a metal vapor cloud, formed by spark ablation, followed by a quick quench. This causes a metal shell to quickly condense around the core particle and form a core-shell nanoparticle.

- Tavares et al [17, 25] synthesized cupper nanoparticles and functionalized their surfaces with hydrophilic and hydrophobic groups by changing the precursor gas using plasma.

- Munzer et al [26] synthesized silica nanoparticles using plasma, which were then coated via decomposition of an organic precursor (e.g. ethylene) on the surface in the afterglow heat of the plasma.
- Zhang et al [27] used photo-initiated chemical vapor deposition technique to physically coat aerosolized NaCl nanoparticles with different organic films.

Although these techniques serve as examples that solvent-free techniques can be applied for continuous, in-line processing of nanoparticles, they suffer from the use toxic materials, extreme operating conditions, complex infrastructure requirements, and high scaling costs.

To address these limitations, we built upon the principals of aerosol photopolymerization. Several studies have shown that irradiating sprayed monomer droplets with UV light leads to formation of micro- and nano-sized polymeric particles [28-30]. This technique was subsequently refined to produce micro-scale spherical nanoparticles loaded with inorganic nanoparticles such as zinc oxide [31, 32]. . However, to the best of our knowledge, no study has reported the use of aerosol photopolymerization specifically to coat nanoparticles.

Here, we introduce a novel and simple continuous aerosol photopolymerization technique, operated at normal conditions, for in-line coating of nanopowders. To demonstrate the process, titanium dioxide nanoparticles (nano-TiO_2) and methyl methacrylate (MMA) were selected as nanoparticle and organic monomer, respectively. Nano-TiO_2 are widely used materials in industrial applications mainly as photocatalysts and reinforcers owing to their photocatalytic behavior, mechanical performance, and thermal, and optical properties [33, 34]. However, their agglomeration behavior can dramatically lower their reactivity and dispersibility in those processes [35]. Those difficulties can be overcome by coating the nanoparticles with a polymer – their inherent photocatalytic activity can be exploited in this regard to form coatings such as poly(methyl methacrylate) (PMMA), polystyrene (PS), and poly(N-isopropylacrylamide) (PNIPAM) [36].

In our previous work [37], we demonstrated a jet-impactor assisted fluidized bed (JIAFB) can break up nanoparticle agglomerates in the gas phase. While the JIAFB allowed for the production of a stream of single, de-agglomerated nanoparticles from an initially agglomerated feedstock, it did not allow the stabilization of these particle to prevent re-agglomeration. In this work, we combine JIAFB with photo-initiated chemical vapor deposition (PICVD) [1, 38, 39]. The newly de-

agglomerated particles are pneumatically guided to a monomer vapor saturation zone, leading to heterogeneous condensation of the monomer onto the nanoparticles, which is subsequently photopolymerized under UV light to yield a organic coating. Processing parameters are key, as photopolymerization must occur quickly before the monomer evaporates away from the surface, or re-agglomeration of nanoparticles is triggered via random collisions or liquid-bridge forces.

6.2 Theory

6.2.1 Condensation of monomer vapor on nanoparticles surfaces

Condensing vapors on a particle surface is the mechanism employed by condensation particle counters (CPC), also known as a condensation nucleus counters (CNC) [40]. These are used to increase the size of fine airborne particles that are invisible to optical counters. In CPCs, fine particles pass through a saturation chamber, filled with vapors of typically lower alcohols. The vapor condenses onto the particles through heterogeneous nucleation, thereby increasing the apparent diameter of the particles as they advance through the chamber and can finally be detected by an optical counter. Here, aerosol particles act similarly as nuclei for heterogenous condensation of monomer vapors. The condensed layer grows as the particles progress through a continuous aerosol photo-reactor, and photopolymerized in flight. Thermodynamically, the probability of heterogenous condensation depends on the size of a particle, its wettability with respect to the condensing liquid, and the degree of saturation of the condensing vapor [41, 42]. If the particle is perfectly wettable, heterogenous condensation will occur for particles diameters equal or larger than the Kelvin diameter, d_k:

$$d_k = \frac{4M\sigma}{\rho RT \ln S} \qquad \text{Equation 6.1}$$

where σ is the surface tension of the liquid, M is its molecular weight, ρ is its density, R is the universal gas constant, and S is the supersaturation (defined as the ratio of actual vapor pressure P in the feed to the saturation vapor pressure P_{sat} at temperature T, $i.e.$ $S = P/P_{sat}(T)$). Accordingly, at a given S, only particles with diameters equal or larger than d_k can serve as nucleation sites for

condensation (and subsequent condensational growth). Whereas heterogenous condensation will not occur for particles smaller than d_k, increasing supersaturation decreases d_k, thereby increasing the probability of condensation onto smaller particles (and the condensational growth rate). Hence, controlling the degree of saturation is important in determining d_k as well as the ultimate size of particles.

If particles are not perfectly wettable, the surface energy of the condensation process will be affected by the interaction of solid-liquid-vapor interfaces. Hence, the contact angle between the solid particle and condensing liquid governs the rate of condensation, J, [43]:

$$J = \pi d_p^2 \, 10^{25} \, exp\left(\frac{-\Delta G}{kT}\right)$$ Equation 6.2

where k is the Boltzman constant, T is the temperature, dp is the particle diameter, and ΔG is the energy change resulting from condensation, which is itself a function of the contact angle, θ, [44]:

$$\Delta G = \frac{16\pi\sigma^3 M^2}{3\,(\rho RT \ln S)^2} f(\theta)$$ Equation 6.3

These equations highlight that the stronger the vapor-particle interaction, the larger the condensation rate. Further, aerosol particles with low affinity for the condensing liquid can serve as nucleation sites for if vapor supersaturation is sufficiently high. Affinity and supersaturation will dictate whether condensation occurs film-wise or drop-wise.

To evaluate the affinity of methyl methacrylate (MMA), a liquid monomer, with the surface of nano-TiO_2 particles, contact angle goniometry tests were carried out with the sessile drop method (supplementary Fig. 6.1). A fine layer of nano-TiO_2 was deposited on a glass microscope slide using a high-speed air jet. The contact angle was measured using an FDS tensiometer OCA DataPhysics TBU 90E. All contact angles were recorded after five seconds from when the drop reaches the surface. The contact angle of 0° indicates the surface of nanopowders are perfectly wettable with MMA, which makes it suitable candidate for this experiment. While roughness effects may explain this behavior in part, the very high surface energy of nano-TiO_2 (~ 1 J/m^2) [45] compared to MMA (0.028 J/m^2) [46] is in agreement with the experimental observations.

The high wettability of MMA towards TiO$_2$ also allows capillary condensation to come into play. In capillary condensation, vapor condenses on the neck between neighboring particles, which leads to bridging between the particles and thus agglomeration. However, Mavliev et al. [47] have previously shown that the effect of particle charge on heterogenous condensation is insignificant for particles greater than 3 nm in diameter.

6.2.2 Reaction Process

Photopolymerization of MMA initiated by semiconductors (e.g. TiO$_2$) has been well documented [36, 48-51]. According to the UV absorption spectra of MMA, it strongly absorbs UV light below 275 nm (largely transparent at higher wavelengths) [49]. Nevertheless, the rate of MMA self-photopolymerization is low because of low monomer decomposition and radical generation rates. TiO$_2$ under UV light promotes radical generation, which significantly boosts the polymerization rate [49, 51]. When a TiO$_2$ particle is irradiated by UV light, it generates a conduction-band electron and a valence-band hole on its surface [49]:

$$TiO_2 \overset{h\upsilon}{\rightarrow} e_{cb}^- + h_{vb}^+$$

Equation 6.4

Although the electrons are not strong enough to induce anionic initiation, the holes, as powerful oxidants, are capable of abstracting a hydrogen atom from the MMA monomers to generate MMA radicals. The MMA radicals, subsequently, attack other monomers and polymerization propagates through a radical polymerization:

Initiation : $\quad$ TiO$_2$ (e$^-$, h$^+$) + [MMA monomer] $\longrightarrow$ TiO$_2$ (e$^-$)H$^+$ + [MMA radical] $\qquad$ Equation 6.5

Propagation : [MMA radical] + [MMA monomer] $\longrightarrow$ [propagating chain] $\qquad$ Equation 6.6
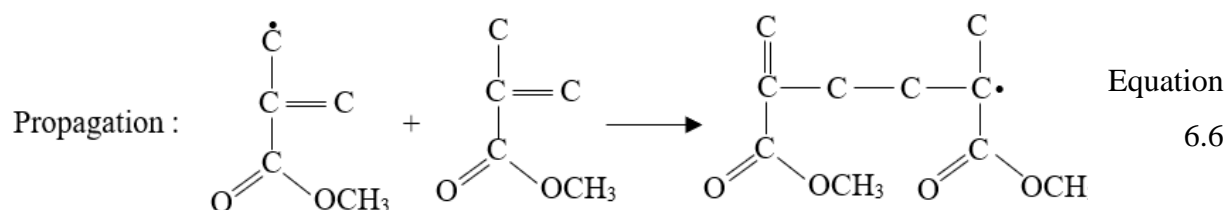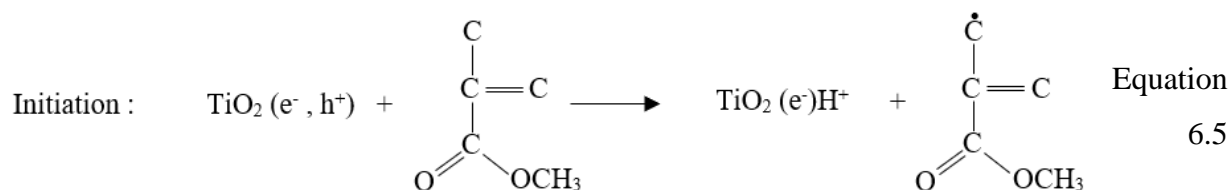
Since initiation originates from the surface of TiO_2, a higher particle specific surface area will lead to a faster reaction rate. TiO_2 nanoparticles lead to noticeably faster photopolymerization compared to self-polymerization of MMA [49], with the anatase phase showing a higher photoactivity than the rutile phase [52]. Akgun et al. [31] had earlier shown that MMA can be photopolymerized in the presence of nano-TiO_2 over reaction times on the order of one minute or less, in the context of polymer-matrix nanocomposite synthesis. Because the photopolymerization reaction is largely surface-initiated, this reaction scheme is pertinent to exploit in an aerosol system, given that the reaction will be selective to coating nanoparticles (no need for downstream purification to remove polymer particles). Further, a high dependency on UV radiation, as a source of energy, results in the fact that chain growth can be instantly started or stopped by turning the light on and off, respectively [53]. This offers more control on the reaction in the aerosol phase, and consequently the thickness of coating.

6.3 Experimental Section

6.3.1 Materials

Methyl methacrylate (MMA, Sigma-Aldrich, 99 % purity) was purified using a prepacked column of inhibitor remover (Sigma-Aldrich) to remove methyl hydroquinone. Titanium dioxide (anatase TiO_2, Nanostructured & Amorphous Materials, 99% purity) nanoparticles had a primary particle size of 30 nm with a specific surface area of 40-60 m^2/g and bulk density of 50 kg/m^3. Dry nitrogen (N_2, Air Liquide, 99.99% purity) was used for fluidization, jet, and carrier gas to prevent any humidity absorption by the nanopowders and undesired effects on the reaction.

6.3.2 Process

The experimental setup consists of three main components: a jet-impactor assisted fluidized bed (JIAFB), a monomer saturator, and a photo-reactor [Fig. 6.1]. The operation of the JIAFB has been fully described previously [37]. Briefly, it consists of an upward-facing micro-jet that directs fluidized nanoparticles towards an impaction plate positioned 5 mm downstream of the jet, within

an 8 mm ID fluidized bed, leading to nanoparticle de-agglomeration. A venturi pump, at the outlet of the system, guides the broken agglomerates to the saturation chamber and then the photo-reactor. In the saturation chamber, monomer vapor is provided by the saturator, in which pure monomer is partially evaporated at a given temperature using a water bath (below its boiling point) and carried to the chamber by an N_2 carrier gas flow. Monomer vapor condenses onto the transported aerosol nanoparticles, which are at room temperature, in the chamber. The now-monomer-covered nanoparticles move to the photo-reactor, where they are exposed to UVC irradiation for photopolymerization. The polymer coated particles are captured downstream using an in-line filter (Whatman® Anodisc inorganic filter membranes, pore size 0.020 µm, installed inside a 47 mm stainless steel filter holder), installed at the outlet of the photo-reactor before the venturi pump. The outlet gas flow also transits through a water trap to remove any remaining entrained particles before discharging to the ventilation system. When transmission electron microscopy (TEM) sampling is required, a rod is inserted into the photo-reactor from the top.

The photo-reactor is a cylindrical quartz tube (5 cm ID, 90 cm length) centered in a modified UV cabinet (Daavlin CO.). It is surrounded by 28 UVC fluorescent tubes (170 cm) emitting mainly at 253.7 nm with a light intensity of 0.012 W/cm^2 at a distance of 33 cm. The aerosol residence time in the saturation chamber and photo-reactor can be controlled by adjusting the inlet flows of the JIAFB (i.e. jet and fluidizing gas flows), carrier gas flow, and the pressure provided the venturi pump. In all experiments, the flow rates of jet and carrier gases were kept constant at 0.6 and 0.5 L/min of N_2, respectively. The fluidizing gas velocity was set to 1.5 cm/s (three times larger than minimum fluidization velocity for TiO_2 nanopowder), leading to a high bed expansion and uniform fluidization of nanopowders around the micro-jet [54, 55]. Accordingly, the average residence time of the aerosol particles in the photoreactor is approximately one minute (residence time distribution obtained from two-phase simulation) .

The temperature of the saturator was set at 50 °C. At this temperature, MMA can reach an equilibrium vapor pressure of 0.15 bar. Upon subsequent cooling to room temperature, where the saturation pressure is 0.036 bar, a saturation ratio of 4.5 is achieved. This supersaturation state guarantees MMA vapor will condense on the surfaces of room-temperature particles.
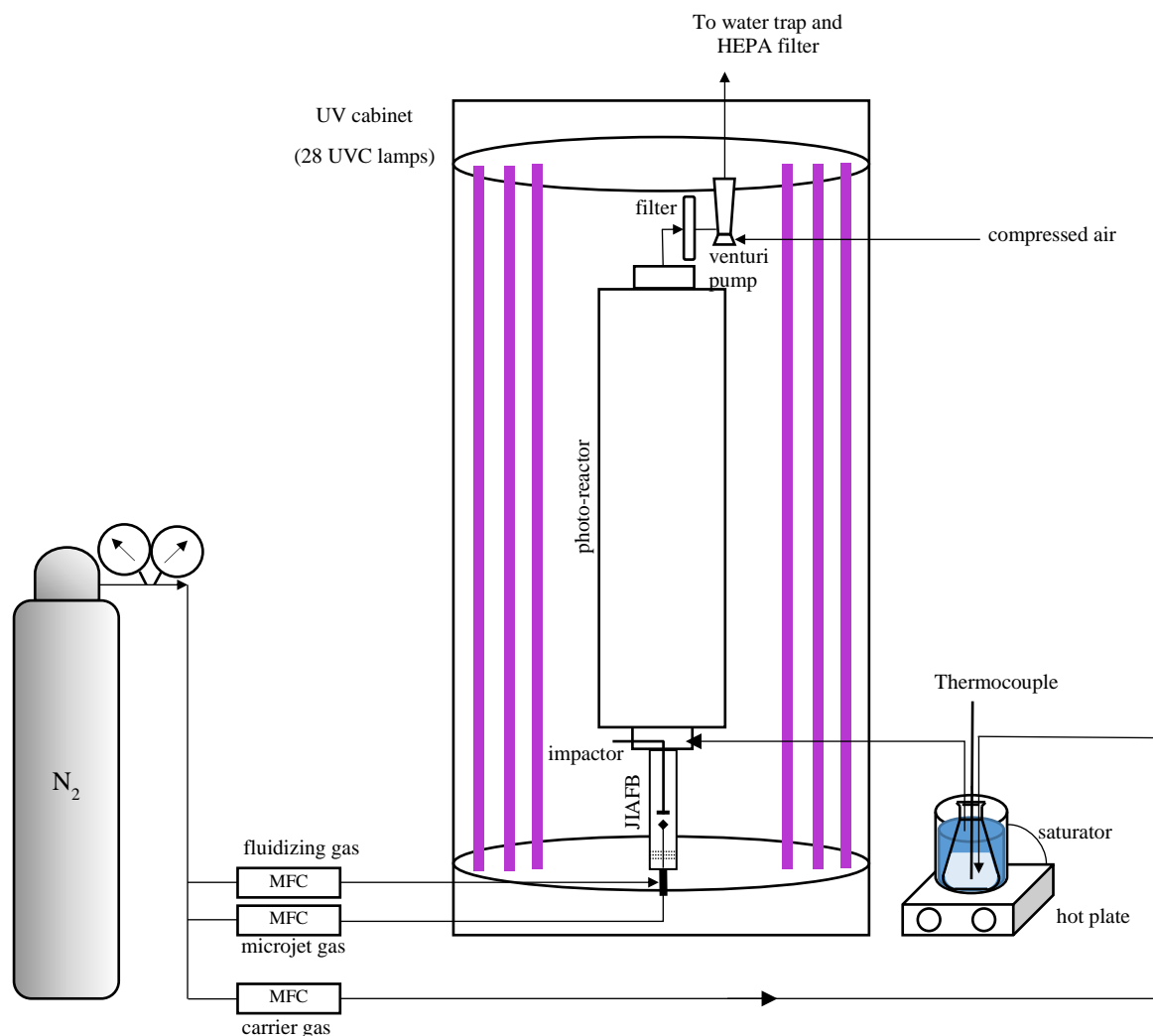
Figure 6.1 Schematic diagram of the JIAFB and the continuous aerosol photo-reactor experimental set up.

6.3.3 Characterization Methods

TEM was carried out on a JEOL JEM-2100F operated at 200 kV in bright-field mode to confirm the presence, thickness and uniformity of the coating. The particles were deposited gently on a TEM grid (Electron Microscopy Sciences, CF-400-Cu, carbon film on a 400 square mesh copper grid) directly from the aerosol phase. ImageJ software [56] was used to determine the average thickness of coating by analyzing the thickness in five TEM micrographs.

The chemical composition of the coating was identified by Attenuated total reflectance Fourier-transform infrared spectroscopy (ATR-FTIR, Thermo Scientific Nicolet iS5 with iD7 ATR). TGA was performed in a TA Instruments Q50 apparatus at a heating rate of 10 °C/min up to 600 °C under N_2 atmosphere. Two isotherms (30 minutes each) were defined before (at 120 °C) and after (at 600°C) the ramp to remove traces of humidity or remaining monomer. The sample size was approximately 10 mg. X-ray photoelectron spectroscopy (XPS) analysis of the samples was carried out using a VG ESCALAB 3 MKII apparatus with an Mg-Kα radiation source (15 kV, 20 mA) with an aperture size of 2×3 mm^2. The base pressure in the UHV analysis chamber was 5×10^{-9} Torr and the experiments were performed at room temperature. An X-ray incident angle of 15° with a corresponding penetration depth of ~10 nm was used for survey scans. Avantage™ XPS analysis software was used to deconvolute the peaks in the high-resolution spectra. For all spectra, a classical Shirley background subtraction was used before fitting the peaks with a symmetric 50% Gauss-Lorentz sum function (0%: pure Gauss, 100%: pure Lorentz).

Particle size was measured in suspension using an Eyetech^{TM} instrument (AmbiValue, Netherlands). This instrument measures particle size based on the theory of the Laser-Obscuration-Time, in which a single particle is scanned with a focused rotating laser beam [57]. For this purpose, a dilute suspension (0.5 g/L) of both bare and coated particles were dispersed using an ultrasonic homogenizer (Cole-Parmer, model CP505 500 W) operating at 100 W with an energy dose of 600,000 J/g$_{TiO2}$. The cuvette was filled with 3 cc of the sonicated sample immediately, followed by slow stirring to keep the particles suspended. Particle size distributions were obtained by averaging three distributions in three cycles, with each cycle lasting one minute (approximately equivalent to 5×10^6 particles measured). To quantify the dispersibility of nanopowders in different solvents, a UV-visible spectrometer (Ultrospec 1100 pro) was used to collect the absorbance spectra in the range of 200-900 nm from the same sonicated suspension.

6.4 Results and Discussion

6.4.1 Physical characterization

Bare and coated TiO$_2$ nanoparticles were collected directly from the aerosol phase. TEM images of the bare particles (Fig. 6.2.a) show agglomerated primary particles with diverse shapes in the

size range of 20-40 nm. The crystallographic orientation of anatase TiO_2 can be seen at the outermost layer of the particle that clearly reveals the sharp edge of the particles. On the other hand, TEM micrographs of coated particles display a conformal thin layer of rough coating around all surfaces. Image processing demonstrates a coating thickness in the range of 0.7-3.5 nm with an average of 1.5 nm (ImageJ software). Thicker coatings were seen on the neck with neighboring particles. This can be due to the capillary condensation that causes monomer vapor condenses more on the concave surfaces rather than convex surfaces. Despite using the JIAFB upstream of the coating step, agglomeration still occurs and can be attributed to the increasing the capillary forces when nanoparticles pass through the saturator chamber. However, the coated particle agglomerates are much smaller than those observed for untreated particles (refer to section 6.4.3).
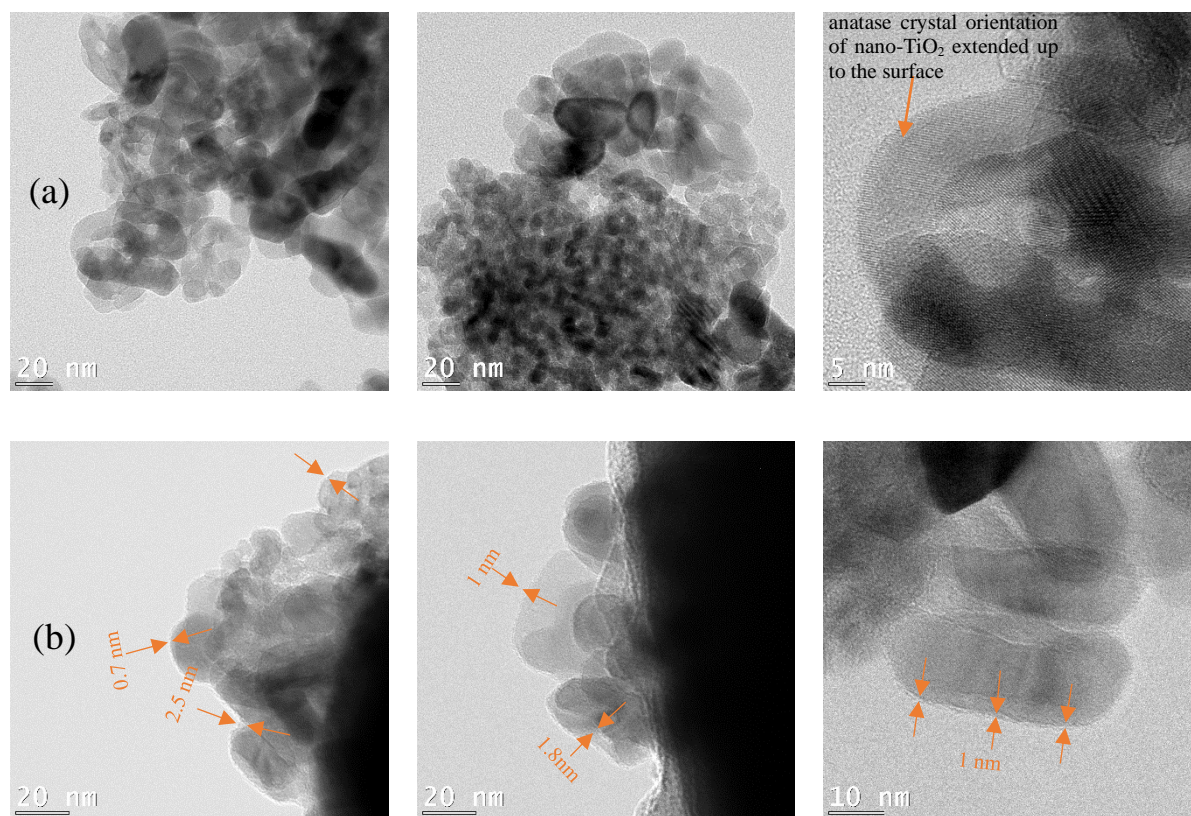
Figure 6.2 TEM micrographs of (a) bare TiO_2 nanoparticles and (b) coated TiO_2 nanoparticles

Thermogravimetric analysis (TGA) was carried out on the bare and coated nano-TiO_2 to determine the mass of the carbon film grown onto the particles (Fig. 6.3). Three weight loss steps can be discussed in the TGA curve: from 25 to 210 °C, both samples experience a weight loss of about

2.5% due to the adsorbed and chemisorbed humidity. This is attributed to the evaporation of non-polymerized volatile monomers that are trapped in the porosity of the coated particles. Over the 210-450 °C range, the bare particle lose 0.5% weight, while the coated particles lose approximately 3.5%. This rise in carbon content of the coated sample compared to the bare sample is ascribed to the initiation of MMA depolymerization that typically begins at around 200 °C [49, 58]. Assuming a uniform coating around nanosphere TiO_2, a 3% difference in weight loss is equivalent to a 1.1 nm coating around all particles, which is in agreement with the TEM results. This confirms the presence of photopolymerized MMA on the surface of nano-TiO_2. Above 450 °C, the bare nano-TiO_2 weight reduces by 1%, attributed to the loss of carbonaceous impurities from the liquid-phase TiO_2 synthesis process [59]. Over this same temperature range, no weight loss was observed for the coated samples.
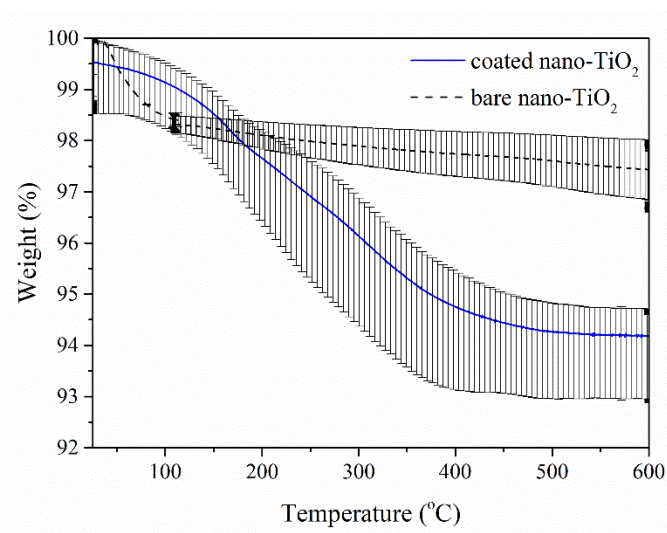
Figure 6.3 TGA curves of bare and coated nano-TiO_2. (error bars represent standard errors of three repetitions).

6.4.2 Chemical characterization

The ATR-FTIR spectra of coated nano-TiO_2 was different from that of the untreated control sample, indicating a clear change in its surface chemical structure (Fig. 6.4). The sharp peak at 632 cm^{-1} in both bare and coated samples shows the stretching vibration of the Ti-O bond. In the coated sample spectrum, multiple organic peaks appear, namely at 1728 and 2950 cm^{-1} (stretching vibration of carbonyl and ester methyl C-H groups, respectively) and at 1481/1453/1438 and 1271-

1063 cm^{-1} (C-H deformations and C-O stretching, respectively). Those group of peaks are a signature of PMMA [60, 61], and are in sharp contrast to the untreated sample with no such peaks present.
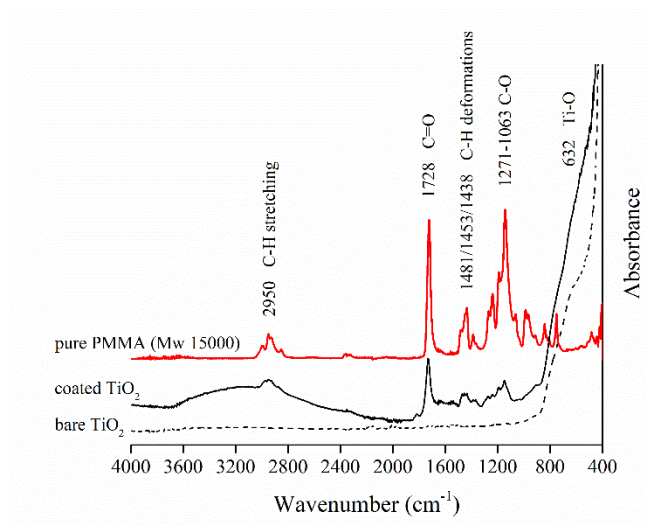
Figure 6.4 IR spectra of pure PMMA (Mw 15000), bare and coated nano-TiO$_2$.
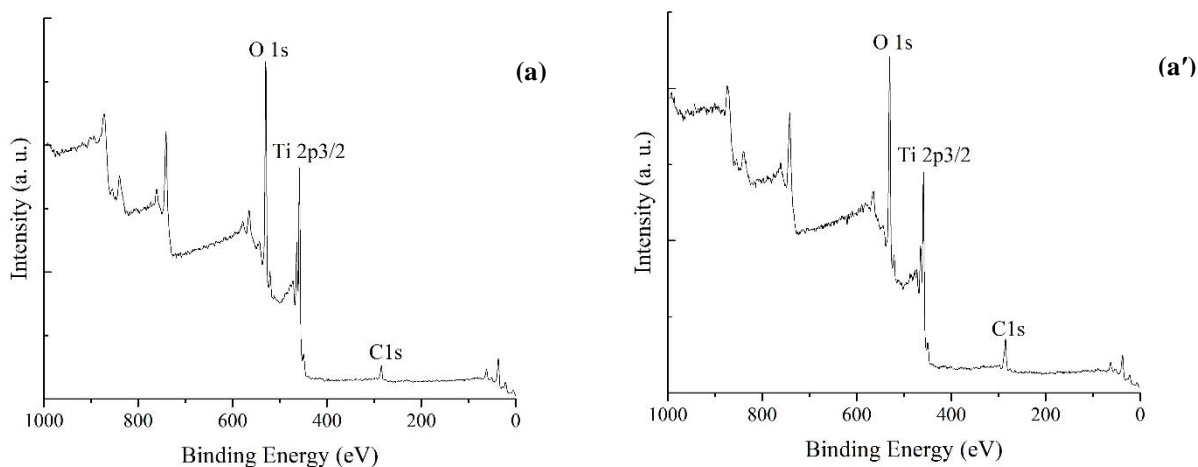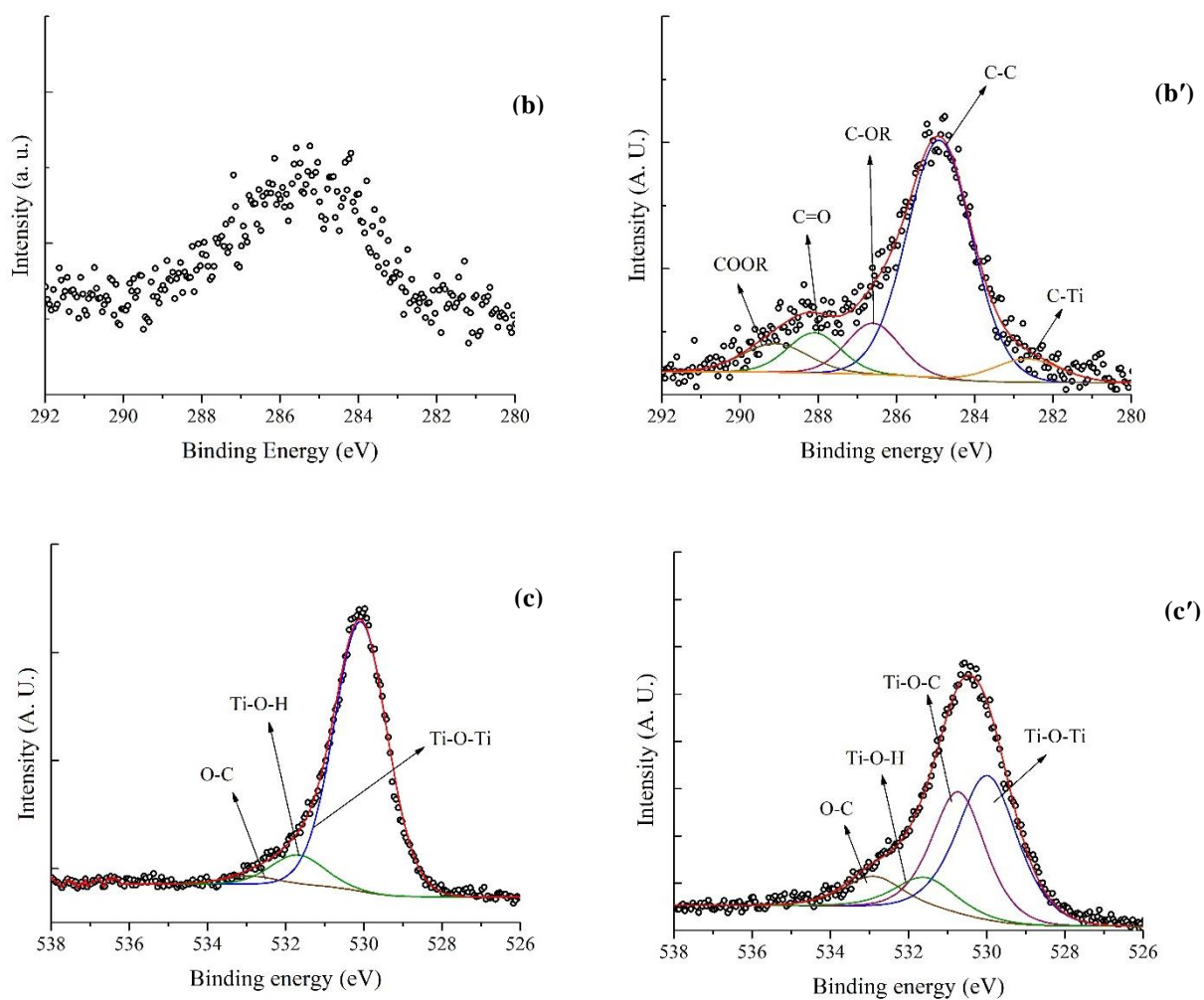
Figure 6.5 XPS survey spectra of (a) bare and (a′) coated nano-TiO₂; high-resolution of C 1s peak deconvolution for (b) bare and (b′) coated nano-TiO₂; high-resolution of O 1s peak deconvolution for (c) bare and (c′) coated nano-TiO₂.

Table 6.1 Location of binding energies and their relative atomic % provided by high-resolution XPS (source of BE obtained by comparison of ref. [62] and [63])

Peak Name	Binding Energy (eV)	Identification	Relative atomic (%)	
			Bare	Coated
C 1s	282.5 ± 0.2	C-Ti	NA	6.5
	285.0 ± 0.2	C-C/C-H	NA	65.1
	286.5 ± 0.2	C-OH/C-OR	NA	11.4
	288.0 ± 0.2	O-C-O/C=O	NA	9.0
	289.5 ± 0.2	COOH/COOR	NA	8.0
O 1s	530.1 ± 0.2	Ti-O-Ti	87.6	45.7
	530.9 ± 0.2	Ti-O-C	Not Detected	34.5
	531.6 ± 0.2	Ti-O-H	9.8	10.2
	532.9 ± 0.2	O-C	2.6	9.6

Quantitative XPS analysis was performed on the bare and coated samples to obtain further information of the coated film (Fig. 6.5, Table 6.1). Quantitative XPS analysis was performed on the bare and coated samples to obtain further information of the coated film (Fig. 6.5, Table 6.1), with binding energy assignments obtained from [62] and [63]. Both survey spectra show TiO_2's characteristic Ti 2p and O 1s peaks (Fig. 6.5. a and a'), as well as a C 1s peak centered at a binding energy of 285 eV. Comparing C 1s survey peaks shows the carbon content of the coated sample is more than double that of the untreated sample, which is in agreement with the TGA analyses (minor carbon contamination in bare TiO_2).

Deconvolution of the C 1s and O 1s high-resolution spectra provide more detailed information about the carbon film (Fig. 6.5.b and b′, Table 6.1). Unfortunately, the low signal-to-noise ratio of the bare nano-TiO_2 C 1s peak prohibited application of the deconvolution algorithm; this serves as additional indication that there is no carbon covalently bonded to the surface, rather it is adsorbed carbon derived from the synthesis of nanopowder. On the other hand, deconvolution of the coated sample's stronger C 1s peak showed a sub-peak centered at 282.5 eV (covalent bonding between Ti and C, 6.5 At%), and a series of sub-peaks from 285 to 289.5 eV (indicative of C-C, C-O-H, C=O, and COOH functionalities). A corresponding sub-peak in the O 1s spectrum (at 532.9 eV) confirms the presence of C-O functionalities, in-line with the previously shown IR spectrum's MMA signature [64]. The O 1s high-resolution spectrum further identifies a sub-peak at 530.9 eV, indicative of a Ti-O-C bond in the treated sample (Fig. 6.5.c and c′). These Ti-C and Ti-O-C covalent bonds not only shows the carbon film is grafted to the surface, but also aligns with the fact that photopolymerization is initiated from the surface of the TiO_2. Deconvolution of the Ti 2p peak is not presented, as the sub-peaks related to Ti-C or Ti-O-C bonds were significantly overshadowed by the peaks assigned to the substrate.

Finally, it is pertinent to note that, during XPS analysis of the coated sample, the pressure in the analysis chamber increased substantially up to 4.5×10^{-8} Torr upon irradiation. This typically occurs for powder samples, due to the desorption of trapped water or reagents in the porosities or adsorbed onto the surface during storage or processing [65]. This decreased to some extent the overall signal-to-noise ratio and thus the quality of the high-resolution spectra.

6.4.3 Particle Size Study

To examine the efficiency of de-agglomerating process, the sizes of bare and coated nano-TiO_2 were measured in n-dodecane (Fig. 6.6, the solvent choice is discussed further in section 6.4.4). Volume distribution shows a significant shift of the size of bare particles to lower sizes, despite of having an extra carbon layer on their surfaces. The average size of particles reduces from 18.25 to 1.84 μm and the particle concentrations rise from 2×10^6 to 8×10^6 #/mL. This demonstrates that the large complex agglomerates, generated during or after production, have been de-agglomerated into smaller clusters as a result of JIAFB process, and these remain small after coating and dispersion. This is mirrored by a shift of the number-based distribution average from 1.06 to 0.7 μm. It is worth

mentioning that measuring particle sizes as small as the primary particle size (0.03 μm) is limited by the lower bound for detection in the instrument used (0.1 μm).
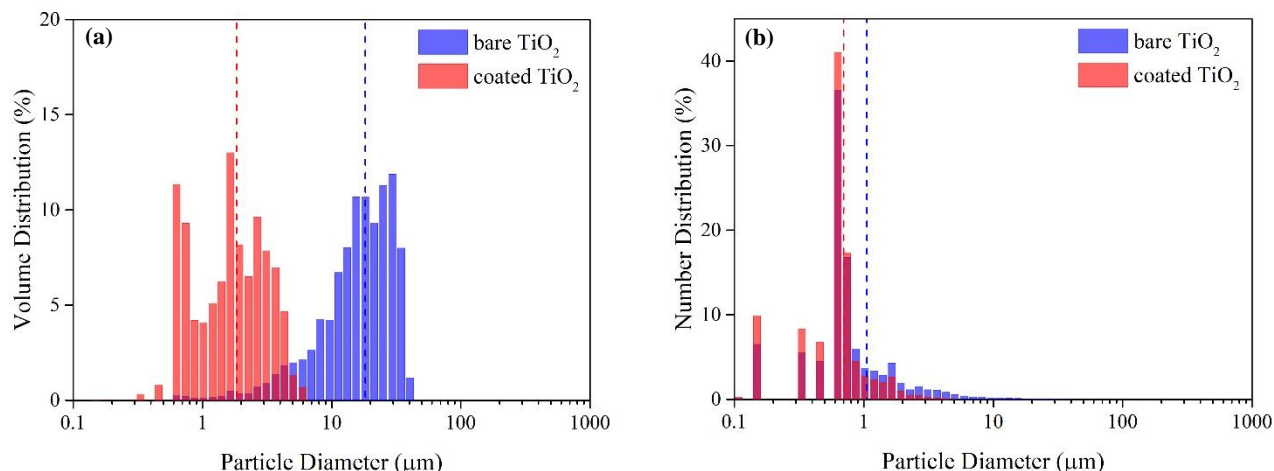
Figure 6.6 Comparing particle size distributions of bare and coated nano-TiO$_2$ in n-dodecane in volume-based (a) and number-based distribution (b). Volume- and number-weighted mean diameters were marked as dash line on the histograms, respectively.

6.4.4 Dispersibility

The dispersibility of bare and coated samples in several solvents with different dielectric constants (ε) was studied qualitatively and quantitively using UV-Vis spectroscopy (Fig. 6.7). For this purpose, dilute (0.1 g/L) suspensions of both samples were prepared in water (polar-protic, ε = 80, relative polarity = 1), acetone (polar-aprotic, ε = 21, relative polarity = 0.35), and n-dodecane (non-polar, ε = 2, relative polarity ≅ 0). Nano-TiO$_2$, before treatment, forms a uniform and stable aqueous dispersion resulting from the hydroxyl groups on their surfaces (Fig. 6.7.a), but the treated particles immediately settle out of suspension given the lack of affinity of the hydrophobic MMA-based coating for the water. UV-Vis spectra confirm this by showing a significant decrease in the absorbance of coated particle suspensions (Fig. 6.7.a′). Further, Christian et al. previously showed that the change of surface plasmon resonance (SPR) band can be interpreted as a change in the surface composition [66]. Accordingly, a noticeable shift of the maximum absorption wavelength

(λ_{max}) from 450 to 260 nm for aqueous suspension suggests a change in the surface composition of nano-TiO$_2$. A similar behavior was observed for acetone.

In contrast, the dispersibility of bare nano-TiO$_2$ in n-dodecane was very poor (particles aggregated and sedimented immediately once mixing stopped), whereas the coated nano-TiO$_2$ exhibited an enhanced dispersion (Fig. 6.7.c), confirmed by the increase in the UV-Vis absorbance spectrum. This indicates a successful conversion of a hydrophilic nanoparticle to a hydrophobic particle capable of dispersion in non-polar media following treatment in the continuous aerosol photopolymerization process.
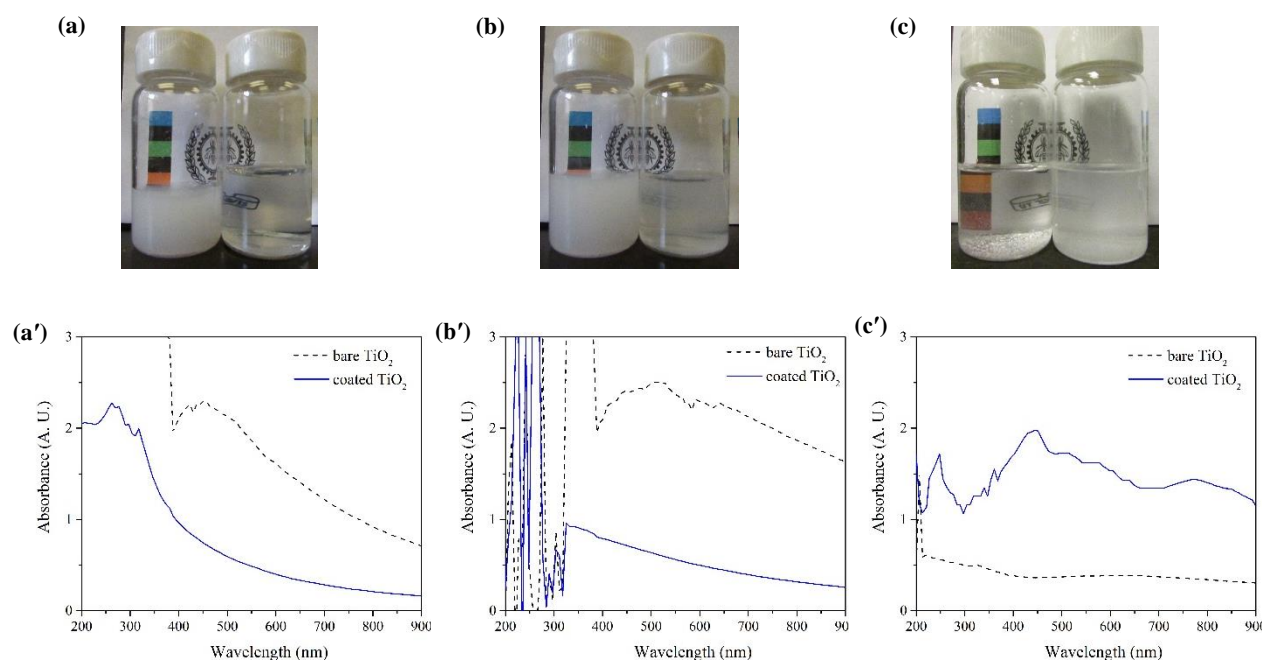
Figure 6.7 Photograph and UV-Vis spectra of bare (left) and coated (right) nano-TiO$_2$ dispersed in water (a), acetone (b), and n-dodecane (c).

To illustrate the colloidal stability of the treated particles in n-dodecane, their absorbance at 900 nm (maximum variation of light intensity) was monitored over time (every 5 min over 47 h). The treated particles show an enhanced stability of dispersion with a delayed re-agglomeration, whereas sedimentation occurs very rapidly for untreated particles (Fig. 6.8.a). Since the solvents are the same, the sedimentation rate of particles in the solvent depends on the physical properties (size and density) and surface-driven properties of particles (chemical affinity of particle-solvent and particle-particle). It was shown previously that the treated particles form smaller agglomerates than

the bare particles (Section 6.4.3), which limits their settling speed. Also, the density of treated particle reduces as a result of an organic coating. Assuming each individual particle has been coated uniformly with a 1.5 nm PMMA layer (Fig. 6.2), it reduces the density of bare particles by 10%. Therefore, bare particles sediment faster because they form larger and denser agglomerates compared to the treated particles, despite their lower number concentration in solution (the higher the number concentration, the higher the agglomeration rate). According to the Hansen dispersibility theory, whenever size enlargement of particles due to agglomeration becomes important, comparing the extinction rate with respect to the relative sedimentation time (RST) is a better measurement for their stability against agglomeration/flocculation [67, 68], as RST normalizes the sedimentation time with the physical properties of the solvent:

$$RST = \frac{t(\rho_p - \rho_s)g}{\eta_s}$$

Equation 6.7

where ρ_p and ρ_s are the density of the particle and the solvent, respectively, η_s is the intrinsic viscosity of the solvent, and g is the acceleration of gravity. This definition is valid when the stability of a single type of particle in various solvents is going to be investigated [69]. However, when the initial particle size becomes important, the RST equation can be modified according to Stokes' sedimentation time:

$$RST = \frac{t(\rho_p - \rho_L)gr^2}{\eta_L h}$$

Equation 6.8

where r is the radius of the particle and h is the settling height. The RST excludes the dependency of sedimentation rate to the physical properties of the particle (e.g. particle size and density) and provides a pure measure of chemical stability of the suspension. Accordingly, the extinction profiles as a function of RST were plotted for both bare and treated particles (Fig 6.8.b), demonstrating that the chemical surface coating plays an important role in the suspension stability. The covalent attachment of a polymer to the particle surface enhances the stability by improving interfacial interactions [15]. Fig 6.8 shows the carbon coated particle not only has a lower sedimentation rate, but also causes a delayed re-agglomeration. This coating technique can be used for applications that require a good dispersibility and long-term storage in target non-polar solvents,

as most of the techniques suffering from detachment of ligands from the particle surface. In addition, re-sonicating the suspension of treated particles with the same energy dose repeats this sedimentation pattern, meaning the de-agglomeration/re-agglomeration phenomenon is reversible. Also, a wide range of applications can benefit from coated nanoparticles with enhanced dispersibility in non-polar media such as reinforcing fillers in polymer matrices [70], nanofluids [71], or in high-tech electronic devices [2].
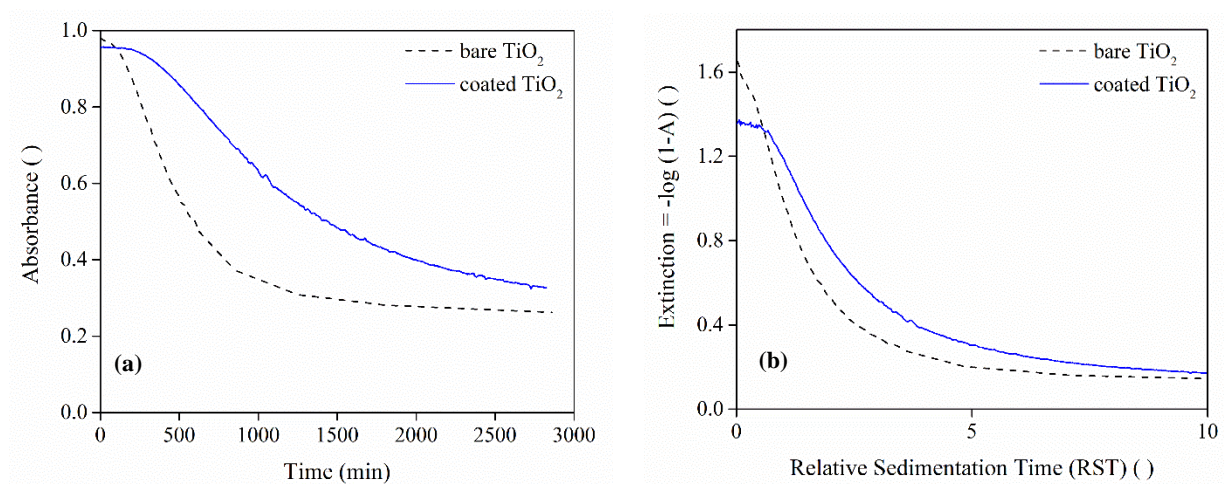
Figure 6.8 (a) Absorbance of bare and coated nano-TiO$_2$ in n-dodecane suspension. Absorbance of 0 represent a pure n-dodecane solvent. (b) Extinction profiles of bare and coated nano-TiO$_2$ in n-dodecane as a function of RST.

6.4.5 Predicting Polymer Quantity at Different Residence Times

Before reacting, the monomer condenses on the surface through heterogeneous condensation. Hence, the particles grow by diffusion of monomer molecules from the vapor onto their surfaces. The particle growth rate at a given temperature can be estimated by using the following equation [72]:

$$r\frac{dr}{dt} = \frac{S-1}{F_k + F_d}$$

Equation 6.9

where, $\frac{dr}{dt}$ is the rate of increase of the radius, $F_k = \frac{L^2 \rho_l}{RKT^2}$ is a thermodynamic heat-conduction term and $F_d = \frac{\rho_l RT}{D P_s(T)}$ is a vapor diffusion term. Plotting this equation for our system (Fig. 6.9.a) shows that, at a saturation ratio S of 4.5, the condensation rate will be so fast that particles as small as 0.01 μm will grow to 1 μm over the first five seconds, and reach 3.5 μm after one minute. Since the final particle size distribution (Fig. 6.6) shows a peak particle size less than 1 μm, this means the evaporation rate is also quite fast. Given these fast evaporation and condensation rates, the reaction rate would be the limiting step that controls the final thickness of the film. MMA follows the typical kinetic rate of a free radical photopolymerization reaction [48, 49, 51, 73, 74]. Blake [73] showed that, in the absence of oxygen, the polymerization rate of MMA is first order with respect to monomer concentration and half order with respect to initiator concentration:

$$R_p = K\sqrt{C_i}\, C_M \qquad\qquad \text{Equation 6.10}$$

where, C_i is the initiator concentration, C_M is the MMA monomer concentration, and K is the rate constant and defined by:

$$K = \sqrt{\frac{2\phi k_d}{k_t}}\, k_p \qquad\qquad \text{Equation 6.11}$$

in which K depends on the quantum yield of chain initiation (ϕ), and the rate constants of dissociation, polymerization, and termination reactions (k_d, k_p, k_t). At room temperature, K was evaluated as 1×10^{-4} (lit/mol)$^{0.5}$.s^{-1} for MMA free radical polymerization [73]. Assuming a reaction-limited regime (compared to condensational growth rate) allows us to predict the amount of PMMA produced during the polymerization at different residence times. In Fig. 6.9.b, the circular data points were measured by Fan et al. [74] for high conversions of MMA over extended periods (several hours), and show good agreement with calculations based on Equation 6.10. However, in the case of aerosol photopolymerization occurring over short residence times (as short as one minute, our measurement marked as square), Equation 6.10 significantly underestimates our experimental data. This can be due to the fact that, in aerosol photopolymerization, unlike bulk polymerization, the reaction occurs on the surface of particles. Hence, the dissociation rate, and

consequently polymerization rate, in aerosol photopolymerization is significantly higher than those of bulk polymerization. Accordingly, modifying the K value to 1×10^{-2} $(lit/mol)^{0.5}.s^{-1}$ to account for the increased probability of radical production and collision, Equation 6.10 accurately predicts the presence of PMMA (3.6%, which is comparable to the 3.5% value we reported in the TGA section, previously) (Fig 6.9.c). A similar approach was used by Esmaeili et al. [12] to predict the polymerization rate of ethylene when the monomer and catalysts are combined on a bed of nanopowders via condensation. In their case, the rate constant was modified by a factor of 1000.
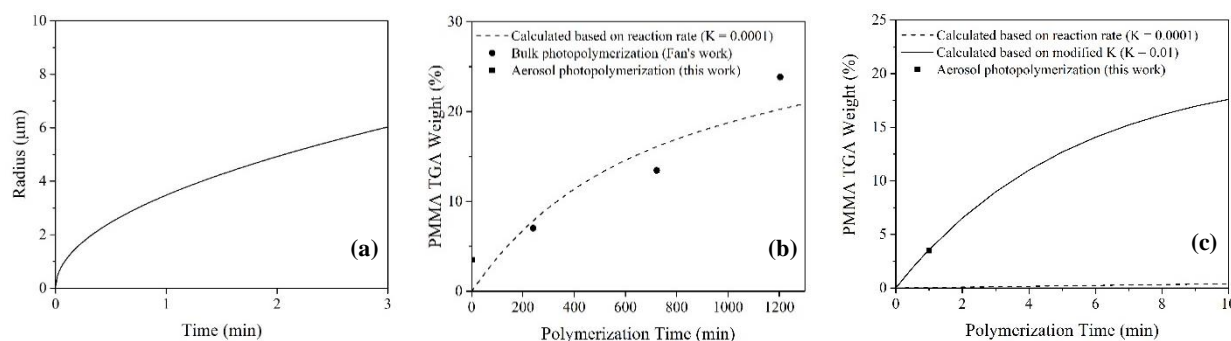
Figure 6.9 (a) growth rate of 0.01 μm-particles in saturation ratio of 4.5 ,(b) profile of PMMA production over time considering a first order free radical polymerization and comparing to bulk photopolymerization (measured by Fan et al [74], circles), aerosol coating (estimated from Zhang et al [27], white squares) and this work (black square), (c) Profile of PMMA production over time with modified K

6.5 Conclusions

We developed a continuous aerosol photopolymerization technique to both de-agglomerate and subsequently coat TiO$_2$ nanoparticle with a carbon film. The MMA monomer, after heterogenous condensation on the surfaces of nanoparticles, is photopolymerized and covers the nanoparticles with a thin film. TEM images confirmed the presence of organic coating around the nanoparticles and agglomerates in the order of 0.7 to 3.5 nm, in agreement with TGA and FTIR results. According to XPS, the film is grafted to the nano-TiO$_2$ surface, corroborating the fact that photopolymerization is initiated from the surface of particles. This guarantees the formation of

carbon film can only happen around the particles, so that no secondary carbon-only particles can be formed during the coating process (thus maintaining sample purity).

After mixing in various solvents, UV-Vis spectroscopy illustrated the improved dispersibility of coated nano-TiO_2 in non-polar media like n-dodecane, and prevents dispersion in polar media like water or acetone. Particle size measurement confirmed that settling velocity reduces for treated particles because of lower density and smaller size of agglomerates. Further, studying the extinction rate over relative sedimentation time revealed that the polymer coating also plays an important role in stability of the suspension by providing a strong steric stabilization that results in longer term colloidal stability and delayed re-agglomeration. To control the thickness of the film, the heterogeneous condensation step will need to be refined further. Moreover, the extension of this process to other nanoparticles and polymers focus of on-going work. Although the nanoparticles were coated herein by exploiting their photo-activity, the technique can be applied to other nanopowders by using photo-active monomers, photo-initiators, or photo-sensitizers. Also, the affinity of nanopowders to polar/non-polar media can be tuned by selecting monomers that provide compatible surface groups. Coating integrity could potentially be improved by employing multifunctional acrylate monomers or adding cross-linking agents – these could increase reactivity and lead to a cross-linked outer layer. The versatility of this continuous technique, combined with the fact that it operates at ambient temperature and atmospheric pressure, is solvent-free and has low scaling costs, makes it an efficient candidate as a unit operation to be integrated into continuous aerosol nanopowders synthesis processes.

6.6 Acknowledgements

6.7 Supplementary Materials

Supplementary Fig 6.1. Sessile drop measurement of an MMA monomer droplet with a glass microscope slide (left) and thin layer of TiO_2 nanopowder deposited on a glass microscope slide (right) soon after the contact with the surfaces.

6.7.1 Further XPS Evidence

Further evidence of the change in substrate surface composition is obtained by comparing peak widths. Indeed, the full-widths-at-half-maximum (FWHM) values of bare and coated samples elucidate a change in the surface elemental composition (supplementary Fig. 2. a and a′). Both samples show sharp peaks at 529.5 eV and 458.5 eV representing O 1s and Ti 2p, respectively. However, the coated samples indicated extra shoulders located toward the side of higher binding energies. The increase of FWHM values from 1.6 eV to 2.4 eV and 1.4 eV to 2.0 eV for O 1s and Ti 2p peaks, respectively, is attributed to the formation of new surface bonds.
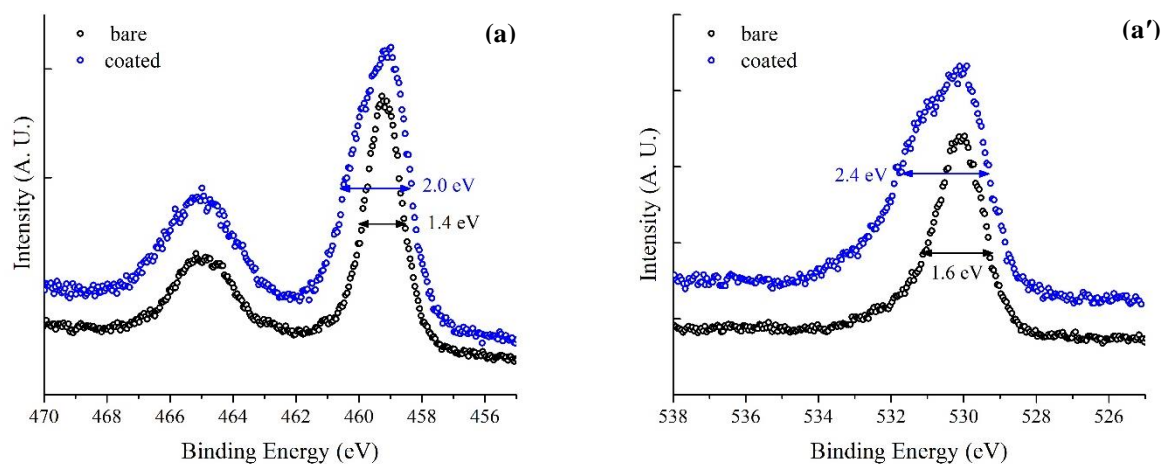
Supplementary Fig.6.2. comparing the high-resolution spectra of Ti 2p (a) and O 1s (a′) peaks for bare and coated samples. The full-widths-at-half-maximum (FWHM) values were depicted on the graphs.

6.8 References

[1] D. Farhanian, G. De Crescenzo, J.R. Tavares, Large-Scale Encapsulation of Magnetic Iron Oxide Nanoparticles via Syngas Photo-Initiated Chemical Vapor Deposition, Sci Rep 8 (2018) 12223.

[2] B.J. Park, J.H. Sung, K.S. Kim, I. Chin, H.J. Choi, Preparation and Characterization of Poly(Methyl Methacrylate) Coated TiO_2 Nanoparticles, J MACROMOL SCI B. 45 (2007) 53-60.

[3] V. Martín, R. Romero-Díez, S. Rodríguez-Rojo, M.J. Cocero, Titanium dioxide nanoparticle coating in fluidized bed via supercritical anti-solvent process (SAS), Chem. Eng. J. 279 (2015) 425-432.

[4] M. Sansotera, S. Geran Malek Kheyli, A. Baggioli, C.L. Bianchi, M.P. Pedeferri, M.V. Diamanti, W. Navarrini, Absorption and photocatalytic degradation of VOCs by perfluorinated ionomeric coating with TiO_2 nanopowders for air purification, Chem. Eng. J. 361 (2019) 885-896.

[5] YupengLi, C. Zeng, C. Wang, L. Zhang, Preparation of C@silica core/shell nanoparticles from ZIF-8 for efficient ciprofloxacin adsorption, Chem. Eng. J. 343 (2018) 645-653.

[6] S. Hosseininasab, N. Faucheux, G. Soucy, J.R. Tavares, Full range of wettability through surface modification of single-wall carbon nanotubes by photo-initiated chemical vapour deposition, Chem. Eng. J. 325 (2017) 101-113.

[7] J.A.H. Lalinde, J. Jiang, G. Jai, J. Kopyscinski, Preparation and characterization of Ni/Al2O3 catalyst coatings on FeCrAl-loy plates used in a catalytic channel reactor with in-situ spatial profiling to study CO2 methanation, Chem. Eng. J. 357 (2019) 435-446.

[8] C.A. Dorval Dion, J.R. Tavares, Photo-initiated chemical vapor deposition as a scalable particle functionalization technology (a practical review), Powder Technol. 239 (2013) 484-491.

[9] V. Mirjalili, M. Yourdkhani, P. Hubert, Dispersion stability in carbon nanotube modified polymers and its effect on the fracture toughness, Nanotechnology 23 (2012) 315701.

[10] D. Wen, Y. Ding, Experimental investigation into convective heat transfer of nanofluids at the entrance region under laminar flow conditions, Int. J. Heat Mass Transfer 47 (2004) 5181-5188.

[11] J. Liu, Y. Gao, D. Cao, L. Zhang, Z. Guo, Nanoparticle dispersion and aggregation in polymer nanocomposites: insights from molecular dynamics simulation, Langmuir 27 (2011) 7926-7933.

[12] B. Esmaeili, J. Chaouki, C. Dubois, Encapsulation of nanoparticles by polymerization compounding in a gas/solid fluidized bed reactor, AlChE J. 55 (2009) 2271-2278.

[13] J. Ellison, G. Wykoff, A. Paul, R. Mohseni, A. Vasiliev, Efficient dispersion of coated silver nanoparticles in the polymer matrix, Colloids and Surfaces A: Physicochemical and Engineering Aspects 447 (2014) 67-70.

[14] F. Zhang, E. Lees, F. Amin, P. Rivera Gil, F. Yang, P. Mulvaney, W.J. Parak, Polymer-coated nanoparticles: a universal tool for biolabelling experiments, Small 7 (2011) 3113-3127.

[15] R.M. Santos, C. Vilaverde, E. Cunha, M.C. Paiva, J.A. Covas, Probing dispersion and re-agglomeration phenomena upon melt-mixing of polymer-functionalized graphite nanoplates, Soft Matter 12 (2016) 77-86.

[16] P. Rivero, J. Garcia, I. Quintana, R. Rodriguez, Design of Nanostructured Functional Coatings by Using Wet-Chemistry Methods, Coatings 8 (2018) 76.

[17] J. Tavares, E.J. Swanson, S. Coulombe, Plasma Synthesis of Coated Metal Nanoparticles with Surface Properties Tailored for Dispersion, Plasma Processes and Polymers 5 (2008) 759-769.

[18] S. Habibzadeh, O. Zabeida, A. Argoitia, R. Sargent, J. Klemberg-Sapieha, J. Chaouki, L. Martinu, Conformal Multilayer Photocatalytic Thin Films on Fine Particles by Atmospheric Pressure Fluidized Bed Chemical Vapor Deposition, Industrial & Engineering Chemistry Research 57 (2018) 10345-10353.

[19] A. Berard, G.S. Patience, G. Chouinard, J.R. Tavares, Photo Initiated Chemical Vapour Deposition To Increase Polymer Hydrophobicity, Sci Rep 6 (2016) 31574.

[20] D. Farhanian, G. De Crescenzo, J.R. Tavares, Kinetics, Chemistry, and Morphology of Syngas Photoinitiated Chemical Vapor Deposition, Langmuir 33 (2017) 1780-1791.

[21] H. Nasri Lari, D. Farhanian, D.C. Boffito, G.S. Patience, G. De Crescenzo, J. Chaouki, J.R. Tavares, Shedding light on iron pentacarbonyl photochemistry through a CVD case study, Catal. Commun. 100 (2017) 19-23.

[22] Y. Wang, R.N. Dave, R. Pfeffer, Polymer coating/encapsulation of nanoparticles using a supercritical anti-solvent process, The Journal of Supercritical Fluids 28 (2004) 85-99.

[23] J. Poostforooshan, S. Rennecke, M. Gensch, S. Beuermann, G.-P. Brunotte, G. Ziegmann, A.P. Weber, Aerosol Process for theIn SituCoating of Nanoparticles with a Polymer Shell, Aerosol Sci. Technol. 48 (2014) 1111-1122.

[24] T.V. Pfeiffer, P. Kedia, M.E. Messing, M. Valvo, A. Schmidt-Ott, Precursor-Less Coating of Nanoparticles in the Gas Phase, Materials (Basel) 8 (2015) 1027-1042.

[25] J. Tavares, S. Coulombe, Dual plasma synthesis and characterization of a stable copper–ethylene glycol nanofluid, Powder Technol. 210 (2011) 132-142.

[26] A. Münzer, J. Sellmann, P. Fortugno, A. Kempf, C. Schulz, H. Wiggers, Inline coating of silicon nanoparticles in a plasma reactor: Reactor design, simulation and experiment, Materials Today: Proceedings 4 (2017) S118-S127.

[27] B. Zhang, Y.-C. Liao, S.L. Girshick, J.T. Roberts, Growth of coatings on nanoparticles by photoinduced chemical vapor deposition, J. Nanopart. Res. 10 (2007) 173-178.

[28] R. Partch, E. Matijević, A.W. Hodgson, B.E. Aiken, Preparation of polymer colloids by chemical reactions in aerosols. I. Poly(p-tertiarybutylstyrene), Journal of Polymer Science: Polymer Chemistry Edition 21 (1983) 961-967.

[29] M. Bazzano, D. Latorre, R. Pisano, M. Sangermano, M. Woerner, Nano-structured polymeric microparticles produced via cationic aerosol photopolymerization, Journal of Photochemistry and Photobiology A: Chemistry 346 (2017) 364-371.

[30] M. Bazzano, D. Marchisio, M. Sangermano, M. Wörner, R. Pisano, A molecular dynamics approach to nanostructuring of particles produced via aerosol cationic photopolymerization, Chem. Eng. Sci. 195 (2019) 1021-1027.

[31] E. Akgün, J. Hubbuch, M. Wörner, Perspectives of aerosol-photopolymerization: organic-inorganic hybrid nanoparticles, Colloid. Polym. Sci. 292 (2014) 1241-1247.

[32] E. Akgün, A. Muntean, J. Hubbuch, M. Wörner, M. Sangermano, Cationic Aerosol Photopolymerization, Macromolecular Materials and Engineering 300 (2015) 136-139.

[33] M. Tsega, F.B. Dejene, Morphological, thermal and optical properties of TiO_2 nanoparticles: The effect of titania precursor, Materials Research Express 6 (2019) 065041.

[34] Y. Zhao, C. Li, X. Liu, F. Gu, H. Jiang, W. Shao, L. Zhang, Y. He, Synthesis and optical properties of TiO_2 nanoparticles, Mater. Lett. 61 (2007) 79-83.

[35] K. Suttiponparnit, J. Jiang, M. Sahu, S. Suvachittanont, T. Charinpanitkul, P. Biswas, Role of Surface Area, Primary Particle Size, and Crystal Phase on Titanium Dioxide Nanoparticle Dispersion Properties, Nanoscale Res Lett 6 (2011) 27.

[36] X. Wang, Q. Lu, X. Wang, J. Joo, M. Dahl, B. Liu, C. Gao, Y. Yin, Photocatalytic Surface-Initiated Polymerization on TiO_2 toward Well-Defined Composite Nanostructures, ACS Appl Mater Interfaces 8 (2016) 538-546.

[37] H. Nasri Lari, J. Chaouki, J.R. Tavares, De-agglomeration of nanoparticles in a jet impactor-assisted fluidized bed, Powder Technol. 316 (2017) 455-461.

[38] K. Chan, K.K. Gleason, Photoinitiated chemical vapor deposition of polymeric thin films using a volatile photoinitiator, Langmuir 21 (2005) 11773-11779.

[39] C.A. Dorval Dion, W. Raphael, E. Tong, J.R. Tavares, Photo-initiated chemical vapor deposition of thin films using syngas for the functionalization of surfaces at room temperature and near-atmospheric pressure, Surf. Coat. Technol. 244 (2014) 98-108.

[40] H.G. Merkus, Particle Size Measurements : Fundamentals, Practice, Quality, Springer Netherlands2009.

[41] C.-C. Chen, C.-J. Tao, Condensation of supersaturated water vapor on submicrometer particles of SiO2 and TiO_2, The Journal of Chemical Physics 112 (2000) 9967-9977.

[42] V. Abdelsayed, M. Samy El-Shall, Vapor phase nucleation on neutral and charged nanoparticles: Condensation of supersaturated trifluoroethanol on Mg nanoparticles, The Journal of Chemical Physics 126 (2007) 024706.

[43] N.H. Fletcher, Size Effect in Heterogeneous Nucleation, The Journal of Chemical Physics 29 (1958) 572-576.

[44] J. Porstendörfer, H.G. Scheibel, F.G. Pohl, O. Preining, G. Reischl, P.E. Wagner, Heterogeneous Nucleation of Water Vapor on Monodispersed Ag and NaCl Particles with Diameters Between 6 and 18 nm, Aerosol Sci. Technol. 4 (2007) 65-79.

[45] P.A. Bhatt, S. Mishra, P.K. Jha, A. Pratap, Size-dependent surface energy and Tolman length of TiO2 and SnO2 nanoparticles, Physica B: Condensed Matter 461 (2015) 101-105.

[46] C. Bruel, S. Queffeulou, T. Darlow, N. Virgilio, J.R. Tavares, G.S. Patience, Experimental methods in chemical engineering: Contact angles, The Canadian Journal of Chemical Engineering 97 (2019) 832-842.

[47] R. Mavliev, P.K. Hopke, H.-C. Wang, D.-W. Lee, A Transition from Heterogeneous to Homogeneous Nucleation in the Turbulent Mixing CNC, Aerosol Sci. Technol. 35 (2001) 586-595.

[48] A.J. Hoffman, H. Yee, G. Mills, M.R. Hoffmann, Photoinitiated polymerization of methyl methacrylate using Q-sized zinc oxide colloids, The Journal of Physical Chemistry 96 (1992) 5540-5546.

[49] C. Dong, X.Y. Ni, The photopolymerization and characterization of methyl methacrylate initiated by nanosized titanium dioxide, Journal of Macromolecular Science-Pure and Applied Chemistry A41 (2004) 547-563.

[50] C.G. I. Sideridou-Karayannidou , O. Orfanou , G. Seretoudi & A. Varvoglis, Photopolymerization of Methyl Methacrylate and other Acrylates with the Use of [Hydroxy(tosyloxy)iodo]benzene as Photoinitiator, Journal of Macromolecular Science-Pure and Applied Chemistry 30 (1993) 781-788.

[51] B. Kraeutler, H. Reiche, A.J. Bard, R.G. Hocker, Initiation of free radical polymerization by heterogeneous photocatalysis at semiconductor powders, Journal of Polymer Science: Polymer Letters Edition 17 (1979) 535-538.

[52] T. Luttrell, S. Halpegamage, J. Tao, A. Kramer, E. Sutter, M. Batzill, Why is anatase a better photocatalyst than rutile?--Model studies on epitaxial TiO_2 films, Sci Rep 4 (2014) 4043.

[53] M. Chen, M. Zhong, J.A. Johnson, Light-Controlled Radical Polymerization: Mechanisms, Methods, and Applications, Chem. Rev. 116 (2016) 10167-10211.

[54] D.M.K. J. Ruud van Ommen, Alan Weimer, Robert Pfeffer, Berend van Wachem, Experiments and modelling of micro-jet assisted fluidization of nanoparticles, (2010).

[55] R.P.J.A.Q.J. Flesch, Fluidized bed systems and methods including micro-jet flow, in: U. Patent (Ed.), Orion Engineered Carbons GmbH New Jersey Institute of Technology, US, 2012.

[56] C.A. Schneider, W.S. Rasband, K.W. Eliceiri, NIH Image to ImageJ: 25 years of image analysis, Nature Methods 9 (2012) 671-675.

[57] EyeTech™ Application Note 2017.01: Particle size analysis related to dissolution and crystallisation studies, February 2020.

[58] J.R. MacCallum, The thermal degradation of poly(methyl methacrylate), Die Makromolekulare Chemie 83 (1965) 137-147.

[59] S. Gupta, M. Tripathi, A review on the synthesis of TiO_2 nanoparticles by solution route, Open Chemistry 10 (2012).

[60] www.webbook.nist.gov, 2019.

[61] M. Penescu, Diffusion of cyclic versus linear poly(oxyethylene) oligomers in poly(methyl methacrylate) by atr - ftir spectroscopy, Chemistry and Biochemistry, Georgia Institute of Technology, Georgia Institute of Technology, August 2009.

[62] J.F. Moulder, Handbook of X-ray Photoelectron Spectroscopy: A Reference Book of Standard Spectra for Identification and Interpretation of XPS Data, illustrated ed., Physical Electronics Division, Perkin-Elmer Corporation, 19921992.

[63] S. Umrao, S. Abraham, F. Theil, S. Pandey, V. Ciobota, P.K. Shukla, C.J. Rupp, S. Chakraborty, R. Ahuja, J. Popp, B. Dietzek, A. Srivastava, A possible mechanism for the emergence of an additional band gap due to a Ti–O–C bond in the TiO2–graphene hybrid system for enhanced photodegradation of methylene blue under visible light, RSC Adv. 4 (2014) 59890-59901.

[64] G. Beamson, A. Bunn, D. Briggs, High-resolution monochromated XPS of poly(methyl methacrylate) thin films on a conducting substrate, Surf. Interface Anal. 17 (1991) 105-115.

[65] P. Krishnan, M. Liu, P.A. Itty, Z. Liu, V. Rheinheimer, M.H. Zhang, P.J. Monteiro, L.E. Yu, Characterization of photocatalytic TiO_2 powder under varied environments using near ambient pressure X-ray photoelectron spectroscopy, Sci Rep 7 (2017) 43298.

[66] P. Christian, M. Bromfield, Preparation of small silver, gold and coppernanoparticles which disperse in both polar and non-polar solvents, J. Mater. Chem. 20 (2010) 1135-1139.

[67] C.M. Hansen, Hansen Solubility Parameters: A User's Handbook, CRC Press, Boca Raton, Fla, 2000.

[68] C. Bruel, J.R. Tavares, P.J. Carreau, M.C. Heuzey, The structural amphiphilicity of cellulose nanocrystals characterized from their cohesion parameters, Carbohydr. Polym. 205 (2019) 184-191.

[69] S. Süß, T. Sobisch, W. Peukert, D. Lerche, D. Segets, Determination of Hansen parameters for particles: A standardized routine based on analytical centrifugation, Adv. Powder Technol. 29 (2018) 1550-1561.

[70] G.W.B.E. T. J. Pinnavaia (Editor), Polymer-Clay Nanocomposites, Chichester: Wiley.2001.

[71] R. Taylor, S. Coulombe, T. Otanicar, P. Phelan, A. Gunawan, W. Lv, G. Rosengarten, R. Prasher, H. Tyagi, Small particles, big impacts: A review of the diverse applications of nanofluids, J. Appl. Phys. 113 (2013) 011301.

[72] C.D. O'Dowd, P.E. Wagner, Nucleation and Atmospheric Aerosols: 17th International Conference, Galway, Ireland, 2007, Springer2007.

[73] S.T. BALKE, The free radical polymerization of methyl methacrylate to high conversions, Faculty of Graduate Studies, McMaster University, 1972.

[74] X. Fan, L. Lin, P.B. Messersmith, Surface-initiated polymerization from TiO_2 nanoparticle surfaces through a biomimetic initiator: A new route toward polymer–matrix nanocomposites, Compos. Sci. Technol. 66 (2006) 1198-1204.

CHAPTER 7   GENERAL DISCUSSION

Our literature review showed there is a demand for a new gas phase process for producing de-agglomerated stable NPs, ideally in the form of individual NPs, that can preserve their size distribution from batch to batch and during their storage. Considering the potential of fluidized bed as a well-known technique for processing powders, and the affordability and scalability of PICVD technique, those were selected for de-agglomerating and coating metal oxide nanopowders. Metal oxide nanopowders are among the most widely studied nanomaterials given their uses in a broad range of fields such as electronic, catalysis, drug delivery, sensors, cosmetics, pharmaceutical equipment, and air/water remediation. In this thesis, we developed a novel continuous technique to de-agglomerate and coat metal oxide NP agglomerates and studied the dynamic of solid particles in the system for optimization and upscaling purposes.

Accordingly, the first objective was to build a JIAFB, as a continuous de-agglomerator that can solve the problem of dynamic agglomeration in batch and semi-batch processes. We demonstrated its applicability by studying the de-agglomeration of silica nanoparticle (article 1, Chapter 4). To complete the process, as the second objective, a novel light-based continuous technique was developed for coating de-agglomerated NPs produced by the JIAFB (article 2, Chapter 5). Studying the particle size distribution and colloidal behavior of coated NPs was essential to understand the physico-chemical properties and stability of de-agglomerated coated NPs. After demonstrating the applicability and feasibility of the process, for the third objective, we investigated the particle velocity and concentration profiles in the vicinity of the jet-impactor as well as through the bed (article 3, Chapter 6). This improves our understanding of the mechanisms responsible for de-agglomeration and determine the key parameters in upscaling the process.

7.1 Studying Deagglomeration in the JIAFB

To de-agglomerate NPs in the gas phase, we developed a novel aerosol device by merging a jet-impactor system within a fluidized bed. The JIAFB breaks up the NP agglomerates by accelerating the fluidized agglomerates onto the impaction plate. Two mechanisms are primarily involved in de-agglomeration of NP agglomerates: shear (resulted by the fluid velocity gradient perpendicular to the direction of flow) and impact breakage (resulted by impaction of high momentum agglomerates upon the impaction plate). The former mechanism has been used in jet-assisted

fluidized beds for years [94, 153], causing breakage of NP agglomerates through providing turbulent shear flow. Also, laminar shear flow has been identified as dominant mechanism of breakage in high pressure homogenizers, orifices, and Mixer-type dispersers [81, 85, 154].

Although shear-based breakage mechanisms can efficiently break up NP agglomerates, there is no control and reproducibility on their process. To address this defect, we added an impactor to the system and used a turbulent gas jet. Adding the impactor brings up the second mechanism, i.e. impaction, allowing controllable breakage of agglomerates through adjusting the kinetic energy of impaction. Gas jet momentum, that is transferred to the particles, accelerates the fluidized agglomerates, which eventually hits upon an impactor. The higher transferred momentum to the agglomerates, the higher kinetic energy for breakage. Therefore, a lower momentum dissipation rate would be favorable since the impact momentum is primarily responsible for breakage of agglomerates. Using complicated designs such as single-stage-single-orifice-impactors (equipped with accelerating nozzles) can lower the dissipation rate and further enhance the impact momentum. On the negative side, a lower dissipation rate diminishes the Venturi zone, which serves as a selective mechanism for separating broken from nonbroken agglomerates.

In the first step of this study, to minimize the re-agglomeration of dispersed particles, a venturi pump provides a vacuum to quickly entrain out broken particles as well as dilute the outlet flow and send it to the particle sizer. In the first step, to ascertain that the jet length and applied kinetic energy are sufficient for de-agglomeration, a single-phase computational fluid dynamics (CFD) simulation in the vicinity of the jet and plate was performed. The result indicated the jet penetration length, even at the lowest velocity, is sufficient to touch the impaction plate which was placed in 5 mm far from the tip of the jet (the jet-to-plate distance was investigated more in our third objective). Also, the jet lengths obtained from simulation were compared with jet lengths calculated by available correlations in the literature. The jet lengths from simulation overestimated the values calculated from the theories since the interaction of solid-gas was overlooked in the simulation. Moreover, the simulation results showed at a jet velocity of 100 m/s, the gas velocity at the impactor is on the order of 48 m/s, corresponding to the kinetic energy per unit mass of 1.2×10^3 m^2/s^2. Froeschke et al. [41] had previously shown that the energy required to break up large fractals (with a fractal dimension of 1.7–2.7) of air-borne metal oxide nanoparticles with primary particle sizes on the order of 6 to 95 nm lay in the range of 1 to 10×10^3 m^2/s^2. This confirms that the onset jet velocity for significant breakage of in-flight large fractal agglomerates

will be at 100 m/s. This was, later, experimentally confirmed for silica NP (primary particle size of 20 nm) using an online size measurement method. Continuous de-agglomeration of aerosolized silica NP was performed at two fluidization velocities (U/U_{mf} = 5.5, 6.2 for the given initial height of the bed and jet-impactor level) and six jet velocities. Figure 7.1, previously presented in table format, shows the average mode size at different jet velocities and at two fluidizing gas velocities. This result was in good agreement with the theory, indicating particle sizes begins to drop after jet velocity of 100 m/s for both fluidization regime.

It is worth mentioning that choosing an appropriate fluidization regime depends on the initial height of the bed and jet-impactor level in the bed. The superficial gas velocity must be high enough that the bed can reach the impactor system level (i.e. higher than the jet outlet), but not too high that it leads to a high entrainment of particles without engaging in the jet-impactor system.
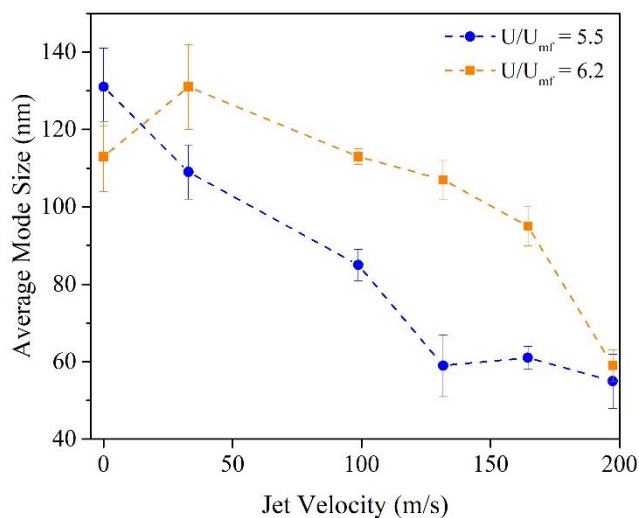
Figure 7.1 average mode size of de-agglomerated silica NPs at different jet velocities and at two fluidizing gas velocities

Finally, TEM images and geometric particle size distribution obtained from them confirmed the effect of impaction on dispersion of dry agglomerates. While non-impacted samples showed dendritic structures with high fractal-like dimensions, impacted particles were dispersed into small clusters down to sub-100 nm particle sizes at jet velocity of 100 m/s. The TEM analysis was impossible at higher jet velocities because the energy from the jet was damaging the TEM grid (Figure 7.2).
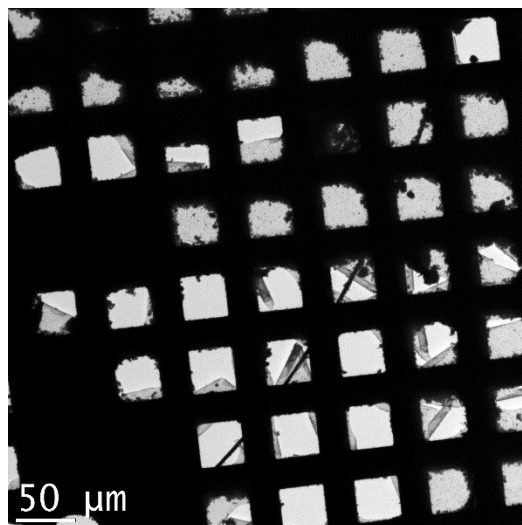
Figure 7.2 TEM micrograph of a damaged carbon lacey Cu 400 TEM grids exposed at jet velocity of 150 m/s.

After publishing the first article, we extended the one phase simulation to two-phase simulation (one-way coupling) by injecting solid particles to the constant gas phase profile matrix (enclosed movie). The one-way coupling simulation, which is valid for two-phase flow with mass fraction less than 10% [155]; predicts the discrete phase patterns based on a fixed continuous phase flow field without considering the interaction of solid phase on the gas phase. A polydisperse particle size distribution was selected for the injected sample to be able to follow the trajectory of particles with sizes in different order of magnitude from 20 nm (resembling individual NPs) up to 200 μm (resembling complex agglomerates). The particle trajectory of spherical particle shown in Figure 7.3 (the bar shape was just selected here to present the pattern of the flow). Studying the particle trajectory of particles illustrated that particles in the order of magnitude of 20 μm and larger cannot be entrained out of the bed at this range of fluidization and jet velocity, even though they were capture by the jet due to the jet cavity. However, particles in the order of magnitude of 2 μm and smaller not only were easily engaged in the jet stream, but also after impaction follows the gas streamlines and be entrained out of the bed. This highlights the cavity effect of the jet as an important mechanism that was not foreseen in the beginning. Due to this effect complex fluidized agglomerates are captured in the jet stream and accelerated to the impaction plate. Further, the agglomerates in the size order of 2 μm cannot escape the system unless they are broken to smaller sizes than that. Hence, higher jet velocities can provide higher level of energies helping breaking up agglomerates, as well as providing higher level of negative pressure around the jet-impactor

system avoiding entraining larger agglomerates. This guarantees by adjusting a proper fluidization velocity we can control the size of the particles at the outflow.
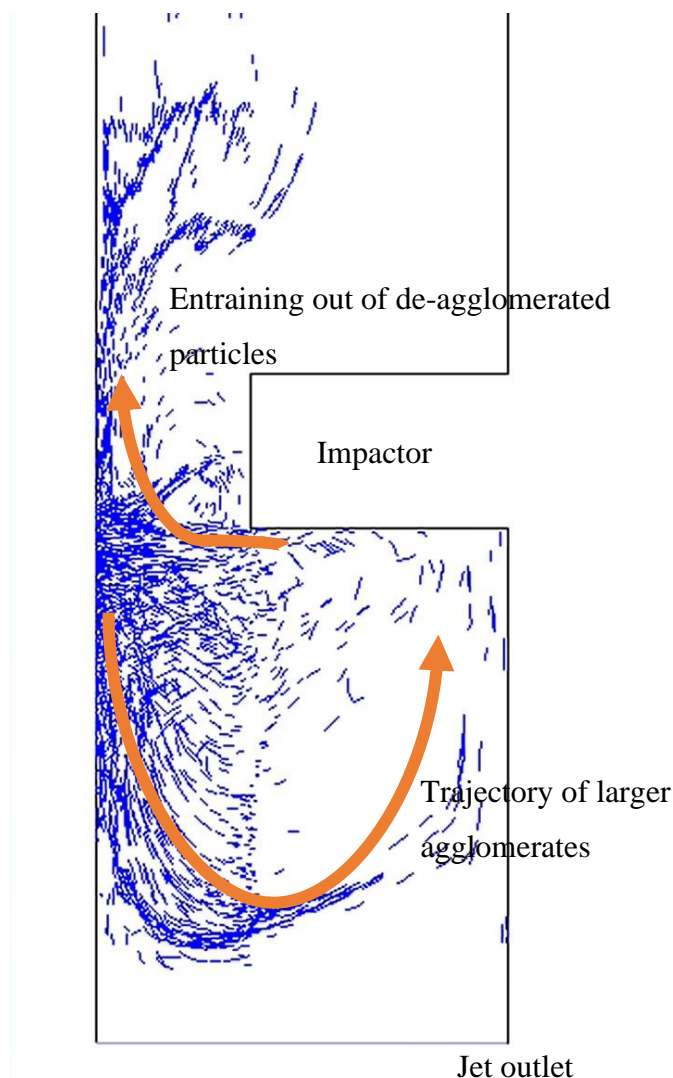
Figure 7.3   Trajectory of de-agglomerated NPs and large agglomerates in the vicinity of JIAFB, simulated by one-way Fluent 6.3 CFD software

7.2 Studying dynamic of solid particle in the vicinity of the jet-impactor

In the second part of this project, we investigated the hydrodynamics of gas jet in fluidization of nanoparticles in order to optimize the jet-to-impactor distance to maximize impact momentum of

agglomerates. This study improved our knowledge about the particle velocity and concentration in the vicinity of the jet-impactor system as well as particle concentration throughout the bed in three configurations including conventional fluidized bed, jet-assisted fluidized bed, and jet-impactor assisted fluidized bed. This provides essential information on scaling up the de-agglomeration process. Also, this is the first report on measuring solid hold-up in a jet-assisted fluidized bed of NPs. Adding a secondary gas injection into a fluidized bed is important in many industrial applications for the purpose of controlling particle size or injecting an additional gaseous reactant locally into the system. Further, as another key outcome of this research, a methodology was developed for reducing random errors and consequently improving the precision of gamma densitometry measurement technique.

In the first part of this section, we performed a parametric study to minimize the random errors coming from the gamma-ray measurement. These random errors originate from the random nature of the radioactive decay, converting gamma-ray to electrical pulses through scintillation detectors, and recording counts in data acquisition system. After adjusting the measurement parameters (discussed in detail in section 6.4.1), we evaluated solid concentration along the jet axis in the vicinity of the jet and far from the jet. The jet velocity of 100 m/s was selected because it is the onset velocity at which breakage of agglomerates begin. Also, MIONP were selected for this set of experiments because:

1) They have stable long-term fluidization which makes it suitable for gamma-densitometry measurements.

2) They possess a high attenuation coefficient with respect to gamma-rays

3) Of their high density and lower voidage comparing to other metal oxide NPs (e.g. silica and titania that offer voidage values as high as 95-98% in fixed bed)

The results showed solid concentration increases along the jet axis from the dilute zone close to the tip of the jet (0.2 cm above the jet) and eventually reaches to almost a constant value far from the jet (2.3 cm above the jet), indicating a uniform fluidization of nanopowders (Figure 6.12).

On the other hand, to evaluate the velocity of agglomerates in the jet, a two-way coupling simulation were conducted using Fluent 6.3 CFD software. Mesh and particle study results were discussed in detail in Appendix A. An average agglomerate size of 70 μm was estimated according

to the minimum fluidization velocity of MIONP using Ergun equation. Accordingly, the velocity profiles were obtained for several particle samples injected to the system (Figure 6.12), indicated the agglomerates reach to their maximum velocity at 1 cm far from the tip of the jet.

Multiplying the solid concentration and velocity profiles will provide the momentum profile of the particle, which shows a maximum value at 1 cm above the tip of the jet. In other words, this is a point at which agglomerates reach their highest concentration in the jet stream and maximum velocities at the same time.

To verify this result, we used a piezoresistive force sensor to measure the forces applied from the air jet as well as accelerated MIONPs to the impaction plate. The experimental results (Figure 6.13) confirmed the theoretical estimations, showing a maximum force at 1-1.2 cm above the tip of the jet at jet velocity of 100 m/s. These theoretical and experimental results are, also, in well agreement with jet length penetration predictions previously obtained by the Hirsan correlation (Table 4.2). Thus, if the impaction plate is placed at this distance, the maximum de-agglomeration rate will be reached for the given particle. As a general rule of thumb, the optimum place of the impaction plate is where the agglomerates reach to their maximum velocities provided that it happens in the range of jet penetration length. Otherwise, the jet penetration length would be the optimum position.

Other general results, obtained through the course of this objective, include:

- The solid hold-up profile showed that rising the microjet velocity locally reduces the solid hold-up near the jet, whereas increases the axial solid distribution and uniformity. Unlikely, adding an impactor causes an asymmetric radial solid hold-up profile due to the asymmetric reflection of the jet gas from the impactor (it is nearly impossible to place and maintain the impactor at an exact 90° angle from the jet).

- A line-decomposition approach was proposed to reconstruct the 3-D local solid hold-up profile based on the radial solid hold-up values. The results show at minimum fluidization regime, the solid hold-up is not well distributed axially, while it becomes more homogeneous when we transit to bubbling regime. Further, turning the jet on leads to formation a dilute zone or permanent jet zone close to the tip.

- Rising the jet velocity increases the jet penetration length, which then results in both reducing the local solid hold-up at higher levels in the bed center as well as increasing the axial solid diffusivity.

7.3 Continuous coating of NPs as stabilization step

In this contribution, the NP coating technique is founded on the aerosol photopolymerization technique combined with heterogeneous/capillary condensation. This process has been used for producing micro- and nano-scale polymeric particles [156] for many years as well as sub-micron polymer-matrix nanocomposites [157]. As a novel method, we employed this technique to coat aerosolized nanopowder with a nanolayer organic film continuously in the order of a minute. In addition to the UV absorption cross-section of reactants, the affinity between particles and condensed precursor as well as a quick photo-reaction rate is required. The aerosol photopolymerization allows incorporation of numerous reactants or photoactive materials into the formulation of precursor. This expands the range of materials and potential functionalities that can be brought on the surface of NPs, besides operation at ambient pressure and temperature. Accordingly, the photochemistry of reaction varies depending on the type of NP and precursor. If NP is more photoactive than the gaseous precursor (i.e. generated radicals are more concentrated on the particle surface than in the gas phase), the reaction mostly occurs on the surface without formation of secondary product in the gas phase. However, if NP has no photoactivity and precursor is enriched with photo-active agents, the formation of secondary product might be possible in the gas phase. In this case, the surface reaction still occurs on the surface leads to the formation of coating, due to the heterogeneous condensation followed by condensational growth mechanism. The optimization of photo-reaction is possible by tuning the initiation rate through the variation of photoinitiator concentration, physicochemical properties of photoinitiator, and photon energy.

It is worth mentioning that aerosol photopolymerization may not always lead to a covalent bond between particle and coated layer (e.g. grafting of PMMA-like film to the surface of nano-TiO_2). However, the coated layer always forms through a chemical reaction.

In the course of first objective, dilution was selected as a temporary solution for minimizing re-agglomeration of broken agglomerates. However, to avoid re-agglomeration and end up with stable

NPs there was a need for a continuous technique that quickly encapsulate de-agglomerated NPs to reduce the interparticle forces and avoid re-agglomeration.

Previously, continuous coating techniques were performed based on high-energy methods such as plasma, supercritical fluids and spark ablation followed by quenching. One of the key outcomes of this research was developing a simple, continuous, low-energy coating technique based on aersol photopolymerization, operated at room temperature and atmospheric pressure. This is the first report about continuous aerosol photopolymerization technique for coating aerosolized metal oxide nanopowders. This allowed us to graft an MMA-base polymer to the de-agglomerated titania NPs.

In the first section of this objective, we demonstrated the deposition of organic coating on the particles and in the second section, we examined the size distribution, dispersibility, and colloidal stability of coated particles in order to study their de-agglomeration and stability performance. TEM micrographs (Fig 5.2) demonstrated deposition of a carbon layer around the particles with an average thickness of 1.5 nm, later on confirmed by TGA. IR spectra of the coated titania proved the chemical structure is a low molecular weight PMMA. More importantly, the XPS results confirmed the presence of a Ti-C bonds, indicating the polymer film is chemically grafted to the surface of nanoparticles. This covalence bond guarantees the organic coating, unlike physical coatings, will not be detached from the surface of the particles. Further, this organic coating reduces interparticle forces such as van der Waals and electrostatic force for dried nanopowder. This leads more stability of nanoparticles in terms of agglomeration due to their storage or pressure from their stacking.

After proving the feasibility of the coating process, the size of collected coated nanopowder was measured using DLS (Malvern Mastersizer 3000, Figure 7.4) and laser obscuration (Eye Tech particle size and shape analyzer, Figure 5.6). Although the particle size distribution obtained from those techniques are different, both techniques showed the size of treated particles, even after coating, is smaller than the untreated particle. The reason of different particle size distribution can be explained by different solvents and different sonication processes. In the case of DLS, the particles were mixed in water (without further sonication), while in laser obscuration, nanopowders were sonicated in n-dodecane (detail of sonication were explained in section 5.3.3).
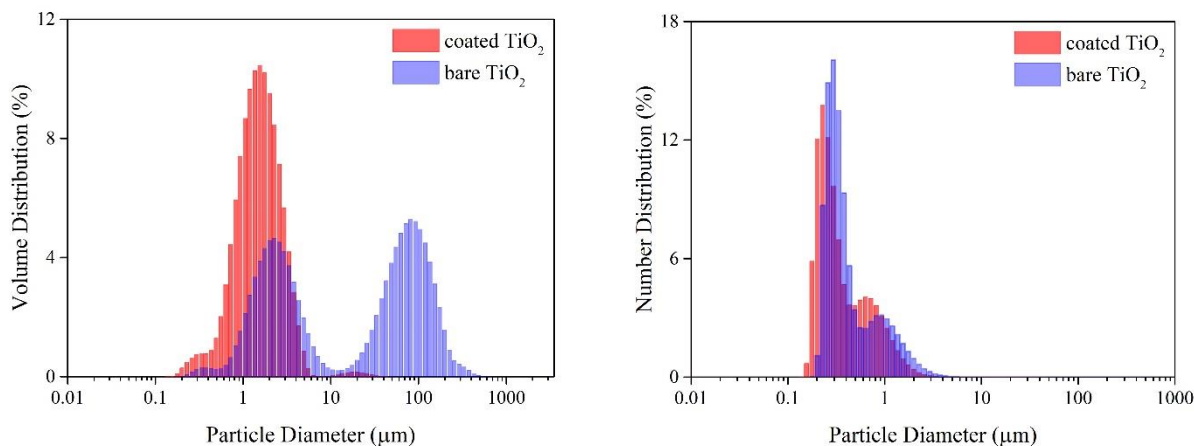
Figure 7.4 Volume (left) and number (right) particle size distribution, measured using DLS technique (MALVERN Mastersizer 3000)

It is worth mentioning that the particle size distribution was measured in the liquid phase due to the nature of those techniques. Unfortunately, an online particle size measurement of dried particle was not possible after coating because the very low concentration of particles made the measurement unreliable. Also, sending reactants to the particle sizer had the risk of damaging the instrument.

To examine the applicability of de-agglomerated coated NP, dispersibility and colloidal stability of powders was examined in polar and non-polar solvents. The dispersibility test showed coating facilitates dispersion of NP in non-polar solvents (like n-dodecane). This was confirmed qualitatively by observation and quantitatively by UV-Vis spectroscopy (Figure 5.7). Moreover, a two-day sedimentation test, after sonication of nanopowders, showed the coated NP are more stable than the bare NP in non-polar medium. This happened as a result of change in physical (particle size) and chemical (chemistry of surface) properties. According to the Stokes sedimentation law, the sedimentation rates of a particle is inversely proportional to its square radius. Thus, the smaller particle size, the lower sedimentation rate. More importantly, by excluding the Stokes parameters from the sedimentation rate, we showed the chemistry of the surface was also playing an important role in stability of colloid by offering a delayed re-agglomeration. Comparing the sedimentation rates of treated and untreated NPs (Figure 5.8.a) showed chemical coating improves the stability of the suspension by providing a strong steric stabilization (stems from PMMA chains) that results in longer term colloidal stability and delayed re-agglomeration.

Although the coating technique was used here to reduce interparticle forces and stabilize the nanopowder, its versatility, scalability, being solvent-free, and low scaling costs, makes it an efficient candidate as a unit operation to be integrated into continuous aerosol nanopowders synthesis processes. Also, this technique can be applied to other nanopowders (without photo-activity) by using photo-active monomers, photoinitiators (PIs), or photosensitizers (PSs). Besides, the affinity of nanopowders to polar/non-polar media can be tuned by selecting monomers that provide compatible surface groups.

CHAPTER 8   CONCLUSION AND RECOMMENDATIONS

8.1 Summary and conclusions

In this research, we have opened up new possibilities for producing stable nano-sized powders by providing solutions to the current challenges in continuous scalable dry de-agglomeration and dry coating of nanopowders. Those techniques reduce the limitations of previous methods in the field on account of the need for complex setup (e.g. the need for vacuum systems), hindrance to scalability, uncontrollability, high energy consumption, and the use of toxic reagents. As a further step, we have provided insights by deep studying of those processes, determining the involved dominant mechanisms, and proposing a methodology for optimization. Besides, a scientific methodology was developed for increasing the accuracy and precision of gamma densitometry measurements, which leads to a reproducible solid hold-up measurement.

In this contribution, a two-stage technique was introduced to continuously de-agglomerate and coat nanoparticles. This work presents a scalable and affordable technique for producing stable homogeneous nanoparticles with smaller particle size distribution. The JIAFB is a low energy continuous de-agglomerator that can solve the problem of upscaling aerosol generators and nanoparticle feeders. Also, the continuous aerosol photopolymerization process, that developed in the course of this research, can be easily combined with any continuous inorganic nanoparticle synthesis processes as a solvent-free post-synthesis process to impart a functional coating. Combining these two techniques can address the issue of heterogeneity in manufacturing nanoparticles.

In the first part of this thesis, we developed the JIAFB and theoretically and experimentally demonstrated that the provided energy via jet-impactor is sufficient to break up NP agglomerates. Some important results of this part:

- The results of CFD simulation reveal that the jet penetration length and kinetic energy of particles upon impaction is high enough to break up the agglomerates, which is confirmed by online particle size measurement via SMPS.

- Both SMPS and TEM measurements imply that at a certain fluidization velocity, increasing the jet velocity shifts the particle size distribution towards smaller diameters, and at higher velocities the mode value reduced from 130 to 55–60 nm.

- The geometric standard deviation or degree of polydispersity rises from 1.5 to 2.0 by increasing the jet velocity up to 197 m/s, as it will increase the total superficial velocity and consequently entrainment of larger particles from the bed.

- The TEM results indicate that the range of individual particle sizes in the supplied nanopowder is wide; hence, increasing the geometric standard deviation can be an indicator of a higher level of agglomerate dispersion.

The second part of this thesis focused on "developing a continuous light-based technique", as a stabilization step, to avoid re-agglomeration of NPs. In the first part section of this part, we confirmed an MMA-like film coat the particles through heterogenous condensation of monomer on the particle surface and exposure to UV. In the second part, we compare the physico-chemical properties of the bare and coated NPs by studying their particle size distribution and their dispersibility and colloidal stability in polar/non-polar solvents. The important results of this part are highlighted below:

- TEM images confirmed the presence of organic coating around the nanoparticles and agglomerates in the order of 0.7 to 3.5 nm, in agreement with TGA and FTIR results.

- According to XPS, the film is grafted to the nano-TiO_2 surface, corroborating the fact that photopolymerization is initiated from the surface of particles. This guarantees the formation of carbon film can only happen around the particles, so that no secondary carbon-only particles can be formed during the coating process (thus maintaining sample purity).

- Particle size measurements in suspension state illustrated the efficiency of the de-agglomeration and subsequent coating process, as coated particles remained smaller than bare particles.

- UV-Vis absorbance spectra show that the MMA-base film deposited around the particles facilitates their dispersion in non-polar solvents.

- Long-term stability experiment confirmed the suspension stability is enhanced not only because of the reduction of agglomerate sizes, but also as a result of the organic coating which improves the interfacial interactions between particle-particle and particle-solvent.

In the final part of this thesis, we focused on the particle concentration and velocity study in the vicinity of jet-impactor system theoretically and experimentally. In the first section of this part, we

provided solid profile map through the bed in three configurations: conventional fluidized bed, jet-assisted fluidized bed, and jet-impactor assisted fluidized bed. Understanding the hydrodynamics of fluidized bed is key to their effective scale-up, efficient operation, and proper design. In the second part, we combined the particle velocity profile (from two-phase simulation) and particle concentration profile (from gamma densitometry measurement) in the jet stream to determine the best position for placing impactor; i.e. where the maximum momentum of NP agglomerates occur. This position which later confirmed experimentally through force measurements. The other main results are as follows:

- Solid hold up profile showed rising the microjet velocity locally reduces the solid hold-up near the jet, whereas increases the axial solid distribution and uniformity. Unlikely, adding an impactor causes an asymmetric radial solid hold-up profile due to the asymmetric reflection of the jet gas from the impactor.

- A line-decomposition approach was proposed to reconstruct the 3-D local solid hold-up profile based on the radial solid hold-up values. The results show at minimum fluidization regime, the solid hold-up is not well distributed axially, while it becomes more homogeneous when we transit to bubbling regime. Further, turning the jet on leads to formation a dilute zone or permanent jet zone close to the tip.

- Rising the jet velocity, increases the jet penetration length which then results in both reducing the local solid hold-up at higher levels in the bed center as well as increasing the axial solid diffusivity.

- The maximum momentum of MIONP agglomerates (agglomerate size of 70 μm) occurred at 10 mm above the tip of the jet, where the velocity and concentration of agglomerates reaches to its maximum. This was confirmed by force measurement which showed the measured force from the NP agglomerates to the sensor reaches to its maximum at 10-12 mm above the tip of the jet.

8.2 Original contributions

Although throughout these achievements we were indebted to "pure science" by using fundamental laws that reveals us the root causes of phenomena, we have mutually contributed to the "pure science". Developing new processes provides the opportunity of producing new materials, which,

in turn, opens up the opportunity for "pure science" to study new field of sciences. This becomes even more important in the field of nanomaterials, in which pure science is still in growing stage. In addition, studying new processes which results in practical problems has been always a source of inspirations and root of ideas for pure science. Therefore, the original contributions of this research are:

- Developing a novel continuous technique for de-agglomerating NP agglomerates in the gas phase, called JIAFB

- Developing a novel continuous light-based technique for coating NPs, called continuous aerosol photopolymerization

- Combining the above processes to continuously de-agglomerate and coat NP agglomerates in the gas phase

- Customizing a force sensor for measuring forces from the high-speed air jet and accelerated in-flight solid particles

- Developing a methodology for improving the gamma densitometry technique for measuring solid hold up in fluidization of nanopowders

- Developing a line-decomposition approach for evaluating local solid hold-up in a jet-impactor assisted fluidized bed and using this technique for mapping solid hold-up distribution in a jet-assisted fluidized bed of nanopowder

8.3 Recommendations

The following subjects are recommended for future work:

- Developing and documenting a standard protocol for measuring particle size distribution of NPs in both on-line and off-line methods; it is essential in comparing particle size distributions of two samples;

- Using the optimized condition (developed in article 3) for de-agglomeration at fluidized bed scale;

- Studying the coating thickness and morphology as well as coated NP size at different relative humidity values (by changing temperature/pressure in saturator or condensation

zone); What will be the effect of humidity (i.e. liquid bridge forces) on the re-agglomeration of NPs?;

- Investigate the flowability (i.e. stickiness), durability, crystallinity, as well as mechanical and optical (e.g. band gap) properties of coated nanopowder;

- Using photoinitiators (PIs), photosensitizers (PSs) and cross-linkers to improve the monomer formulation and extend it for other types of NPs with no photo-activity;

- Online monitoring the evolution of NPs during coating by an online particle sizer. (If SMPS is going to be used, make sure avoiding reactants from introducing to the SMPS);

- Study the photoreaction of monomer in the aerosol phase and suggesting a kinetic rate;

- Design a cleaning procedure for the quartz reactor considering the fact that reactor wall would become opaque which limits light intensity over the course of treatment;

- Combining the continuous aerosol photopolymerization technique with a continuous gas phase nanopowder synthesis method (e.g. spark discharge) and compare the results with the process introduced in this research;

REFERENCES

[1] M. Weller, T. Overton, J. Rourke, F. Armstrong, Inorganic Chemistry, OUP Oxford 2014.

[2] P. J. Krusic, ESR study of paramagnetic iron carbonyl hydrides, Journal of the American Chemical Society, 103 (1981) 2131-2133.

[3] www.iso.org, Source: ISO/TS 80004-2:2015, 4.4, access date: December 2019.

[4] C. Kittel, Introduction to Solid State Physics, Wiley 2004.

[5] M. C. Daniel, D. Astruc, Gold nanoparticles: assembly, supramolecular chemistry, quantum-size-related properties, and applications toward biology, catalysis, and nanotechnology, Chem Rev, 104 (2004) 293-346.

[6] S. Horikoshi, N. Serpone, Microwaves in Nanoparticle Synthesis: Fundamentals and Applications, Chapter 1 - Introduction to Nanoparticles, Wiley 2013.

[7] M. Loos, Carbon Nanotube Reinforced Composites, Chapter 1 - Nanoscience and Nanotechnology, CNR Polymer Science and Technology 2015.

[8] F. Antonii, Panacea Aurea-Auro Potabile, Hamburg: Ex Bibliopolio Frobeniano 1618.

[9] L. A. Dykman, N. G. Khlebtsov, Gold nanoparticles in biology and medicine: recent advances and prospects, Acta naturae, 3 (2011) 34-55.

[10] K. Chang, Tiny Is Beautiful: Translating 'Nano' Into Practical, The New York Times, (Feb 22, 2005).

[11] T. Appenzeller, The man who dared to think small, Science, 254 (1991) 1300.

[12] R. Moreno, B. Ferrari, Nanoparticles Dispersion and the Effect of Related Parameters in the EPD Kinetics, (2012) 73-128.

[13] R. Konwar, A. B. Ahmed, Nanoparticle: An Overview of Preparation, Characterization and Application, International Research Journal of Pharmacy, 4 (2013) 47-57.

[14] A. E. Kestell, Nanoparticles: Properties, Classification, Characterization, and Fabrication, Nova Science Publishers, Inc. 2010.

[15] National Historic Chemical Landmark, Discovery of Fullerenes, American Chemical Society at the Richard E. Smalley Institute for Nanoscale Science and Technology at Rice University in Houston, Texas, Designated October 11, 2010, .

[16] D. R. Larson, W. R. Zipfel, R. M. Williams, S. W. Clark, M. P. Bruchez, F. W. Wise, W. W. Webb, Water-soluble quantum dots for multiphoton fluorescence imaging in vivo, Science, 300 (2003) 1434-1436.

[17] T. Chakraborty, Chapter 2 - Quantum dots, in: T. Chakraborty (Ed.) Quantum Dots, North-Holland, Amsterdam, 1999, pp. 7-108.

[18] J. Drbohlavova, V. Adam, R. Kizek, J. Hubalek, Quantum dots - characterization, preparation and usage in biological systems, Int J Mol Sci, 10 (2009) 656-673.

[19] J. P. Rao, K. E. Geckeler, Polymer nanoparticles: Preparation techniques and size-control parameters, Progress in Polymer Science, 36 (2011) 887-913.

[20] H. K. S. Y. Nagavarma B V N, Ayaz a, Vasudha L.S, Shivakumar H.G Different Techniques for Preparation of Polymeric Nanoparticles-A Review, Asian Journal of Pharmaceutical and Clinical Research, 5 (2012) 16-23.

[21] L. Cismaru, M. Popa, ChemInform Abstract: Polymeric Nanoparticles with Biomedical Applications, ChemInform, 42 (2011) no-no.

[22] U. Gupta, H. B. Agashe, A. Asthana, N. K. Jain, A review of in vitro-in vivo investigations on dendrimers: the novel nanoscopic drug carriers, Nanomedicine, 2 (2006) 66-73.

[23] M. Jedrych, K. Borowska, R. Galus, B. Jodlowska-Jedrych, The evaluation of the biomedical effectiveness of poly(amido)amine dendrimers generation 4.0 as a drug and as drug carriers: a systematic review and meta-analysis, Int J Pharm, 462 (2014) 38-43.

[24] V. V. Mody, R. Siwale, A. Singh, H. R. Mody, Introduction to metallic nanoparticles, J Pharm Bioallied Sci, 2 (2010) 282-289.

[25] Y. S. Kang, S. Risbud, J. F. Rabolt, P. Stroeve, Synthesis and Characterization of Nanometer-Size Fe3O4and γ-Fe2O3Particles, Chemistry of Materials, 8 (1996) 2209-2211.

[26] S. Rudge, C. Peterson, C. Vessely, J. Koda, S. Stevens, L. Catterall, Adsorption and desorption of chemotherapeutic drugs from a magnetically targeted carrier (MTC), Journal of Controlled Release, 74 (2001) 335-340.

[27] D. Vollath, D. V. Szabó, J. Hauβelt, Synthesis and properties of ceramic nanoparticles and nanocomposites, Journal of the European Ceramic Society, 17 (1997) 1317-1324.

[28] A.-I. Moreno-Vega, T. Gómez-Quintero, R.-E. Nuñez-Anita, L.-S. Acosta-Torres, V. Castaño, Polymeric and Ceramic Nanoparticles in Biomedical Applications, Journal of Nanotechnology, 2012 (2012) 1-10.

[29] D. Farhanian, G. De Crescenzo, J. R. Tavares, Large-Scale Encapsulation of Magnetic Iron Oxide Nanoparticles via Syngas Photo-Initiated Chemical Vapor Deposition, Sci Rep, 8 (2018) 12223.

[30] B. J. Park, J. H. Sung, K. S. Kim, I. Chin, H. J. Choi, Preparation and Characterization of Poly(Methyl Methacrylate) Coated TiO2 Nanoparticles, Journal of Macromolecular Science, Part B, 45 (2007) 53-60.

[31] V. Martín, R. Romero-Díez, S. Rodríguez-Rojo, M. J. Cocero, Titanium dioxide nanoparticle coating in fluidized bed via supercritical anti-solvent process (SAS), Chemical Engineering Journal, 279 (2015) 425-432.

[32] M. Sansotera, S. Geran Malek Kheyli, A. Baggioli, C. L. Bianchi, M. P. Pedeferri, M. V. Diamanti, W. Navarrini, Absorption and photocatalytic degradation of VOCs by perfluorinated ionomeric coating with TiO2 nanopowders for air purification, Chemical Engineering Journal, 361 (2019) 885-896.

[33] Yupengli, C. Zeng, C. Wang, L. Zhang, Preparation of C@silica core/shell nanoparticles from ZIF-8 for efficient ciprofloxacin adsorption, Chemical Engineering Journal, 343 (2018) 645-653.

[34] S. Hosseininasab, N. Faucheux, G. Soucy, J. R. Tavares, Full range of wettability through surface modification of single-wall carbon nanotubes by photo-initiated chemical vapour deposition, Chemical Engineering Journal, 325 (2017) 101-113.

[35] J. a. H. Lalinde, J. Jiang, G. Jai, J. Kopyscinski, Preparation and characterization of Ni/Al2O3 catalyst coatings on FeCrAl-loy plates used in a catalytic channel reactor with in-situ spatial profiling to study CO2 methanation, Chemical Engineering Journal, 357 (2019) 435-446.

[36] G. Nichols, S. Byard, M. J. Bloxham, J. Botterill, N. J. Dawson, A. Dennis, V. Diart, N. C. North, J. D. Sherwood, A review of the terms agglomerate and aggregate with a recommendation for nomenclature used in powder and particle characterization, Journal of Pharmaceutical Sciences, 91 (2002) 2103-2109.

[37] M. Seipenbusch, P. Toneva, W. Peukert, A. P. Weber, Impact Fragmentation of Metal Nanoparticle Agglomerates, Particle & Particle Systems Characterization, 24 (2007) 193-200.

[38] D. Walter, Primary Particles - Agglomerates - Aggregates, (2013) 9-24.

[39] O. E. Oberdörster G, Oberdörster J Nanotoxicology: An emerging discipline evolving from studies of ultrafine particles, Environ Health Perspect, 113 (2005) 823–839.

[40] E. Bae, B.-C. Lee, Y. Kim, K. Choi, J. Yi, Effect of agglomeration of silver nanoparticle on nanotoxicity depression, Korean Journal of Chemical Engineering, 30 (2012) 364-368.

[41] S. Froeschke, S. Kohler, A. P. Weber, G. Kasper, Impact fragmentation of nanoparticle agglomerates, Journal of Aerosol Science, 34 (2003) 275-287.

[42] J. Shabanian, R. Jafari, J. Chaouki, Fluidization of Ultrafine Powders-Review, International Review of Chemical Engineering, 4 (2012) 16-50.

[43] J. Visser, Van der Waals and other cohesive forces affecting powder fluidization, Powder Technology, 58 (1989) 1-10.

[44] H. C. Hamaker, The London—van der Waals attraction between spherical particles, Physica, 4 (1937) 1058-1072.

[45] I. E. Dzyaloshinskii, E. M. Lifshitz, L. P. Pitaevskii, General Theory of Van Der Waals' Forces, Soviet Physics Uspekhi, 4 (1961) 153-176.

[46] Particle adhesion theory and experiment, Advances in Colloid and Interface Science, 1 (1967) 111-239.

[47] J. R. Van Ommen, J. M. Valverde, R. Pfeffer, Fluidization of nanopowders: a review, J Nanopart Res, 14 (2012) 737.

[48] G. Calvert, M. Ghadiri, R. Tweedie, Aerodynamic dispersion of cohesive powders: A review of understanding and technology, Advanced Powder Technology, 20 (2009) 4-16.

[49] M. Corn, C. N. Davis, Aerosol Science, Academic Press, London, 1966.

[50] J. P. K. Seville, C. D. Willett, P. C. Knight, Interparticle forces in fluidisation: a review, Powder Technology, 113 (2000) 261-268.

[51] M. Naito, T. Yokoyama, K. Hosokawa, K. Nogi, Nanoparticle Technology Handbook (3rd Edition), Chapter 3, Elsevier 2018.

[52] R. J. Dry, I. N. Christensen, G. C. Thomas, The effect of naturally-occurring interparticle forces on the fluidisation characteristics of fine iron oxide powders, Chemical Engineering Science, 43 (1988) 1033-1038.

[53] H. Krupp, Particle adhesion theory and experiment, Advances in Colloid and Interface Science, 1 (1967) 111-239.

[54] B. H. Kaye, A Random Walk Through Fractal Dimensions, VCH, Weinheim 1989.

[55] A. P. Weber, S. K. Friedlander, In situ determination of the activation energy for restructuring of nanometer aerosol agglomerates, Journal of Aerosol Science, 28 (1997) 179-192.

[56] D. W. Schaefer, A. J. Hurd, Growth and Structure of Combustion Aerosols: Fumed Silica, Aerosol Science and Technology, 12 (1990) 876-890.

[57] J. D. T. Alfred P. Webera, Sheldon K. Friedlandera, Microstructure of Agglomerates of Nanometer Particles, MRS Proceedings, 380 (1995) 87.

[58] A. Zahradnicek, Untersuchungen zur Dispergierung von Quarz- und Kalkstein Fraktionen im Korngroßenbereich 0.5 –10 um in stromenden Gasen, University of Karlsruhe, Institute for Mechanical Engineering, 1976.

[59] H. Rumpf, Grundlagen und Methoden des Granulierens, Chemie Ingenieur Technik - CIT, 30 (1958) 144-158.

[60] C. Weiler, M. Wolkenhauer, M. Trunk, P. Langguth, New model describing the total dispersion of dry powder agglomerates, Powder Technology, 203 (2010) 248-253.

[61] M. Seipenbusch, S. Rothenbacher, M. Kirchhoff, H. J. Schmid, G. Kasper, A. P. Weber, Interparticle forces in silica nanoparticle agglomerates, Journal of Nanoparticle Research, 12 (2009) 2037-2044.

[62] S. Niedballa, Dispergierung von feinen Partikelfraktionen in Gasströmungen Einfluss von Dispergierbeanspruchung und oberflächenmodifizierenden Zusätzen, Von der Fakultät für Maschinenbau, Verfahrens- und Energietechnik, Universität Bergakademie Freiberg genehmigte, 1999.

[63] E. Yoshiyuki, H. Shinji, K. Yasuo, Dispersion of aggregates of fine powder by acceleration in an air stream and its application to the evaluation of adhesion between particles, Powder Technology, 91 (1997) 25-30.

[64] K. L. Johnson, K. Kendall, A. D. Roberts, Surface Energy and the Contact of Elastic Solids, Proceedings of the Royal Society A: Mathematical, Physical and Engineering Sciences, 324 (1971) 301-313.

[65] B. V. Derjaguin, V. M. Muller, Y. P. Toporov, Effect of contact deformations on the adhesion of particles, Journal of Colloid and Interface Science, 53 (1975) 314-326.

[66] V. M. Muller, V. S. Yushchenko, B. V. Derjaguin, On the influence of molecular forces on the deformation of an elastic sphere and its sticking to a rigid plane, Journal of Colloid and Interface Science, 77 (1980) 91-101.

[67] H. Schubert, Principles of agglomeration, Int. Chem. Eng., 21 (1981) 363-377.

[68] H. Schubert, Handbuch der Mechanischen Verfahrenstechnik, (2003).

[69] C. Weiler, Generierung leicht dispergierbarer Inhalationspulver mittels Sprühtrocknung, Johannes Gutenberg-Universität, Mainz, 2009.

[70] D. Geldart, Types of gas fluidization, Powder Technology, 7 (1973) 285-292.

[71] R. Saidur, K. Y. Leong, H. A. Mohammad, A review on applications and challenges of nanofluids, Renewable and Sustainable Energy Reviews, 15 (2011) 1646-1668.

[72] G. Gréhan, G. Gouesbet, A. Naqwi, F. Durst, Particle Trajectory Effects in Phase Doppler Systems: Computations and experiments, Particle & Particle Systems Characterization, 10 (1993) 332-338.

[73] J. H. Fendler, Colloid chemical approach to nanotechnology, Korean Journal of Chemical Engineering, 18 (2001) 1-13.

[74] L. Chen, H. Xie, Y. Li, W. Yu, Nanofluids containing carbon nanotubes treated by mechanochemical reaction, Thermochimica Acta, 477 (2008) 21-24.

[75] W. Yu, H. Xie, A Review on Nanofluids: Preparation, Stability Mechanisms, and Applications, Journal of Nanomaterials, 2012 (2012) 1-17.

[76] S. Pradhan, J. Hedberg, E. Blomberg, S. Wold, I. Odnevall Wallinder, Effect of sonication on particle dispersion, administered dose and metal release of non-functionalized, non-inert metal nanoparticles, Journal of Nanoparticle Research, 18 (2016) 285.

[77] V. S. Nguyen, D. Rouxel, R. Hadji, B. Vincent, Y. Fort, Effect of ultrasonication and dispersion stability on the cluster size of alumina nanoscale particles in aqueous solutions, Ultrason Sonochem, 18 (2011) 382-388.

[78] N. I. Hiroyoshi Yoden, Effect of Small Size Beads on Dispersion of Nanometer-Sized Silica Particle by Wet Beads Mill Process Journal of the Society of Powder Technology, Japan, 41 (2004) 457-464.

[79] T. T. Mitsugi Inkyo, Dispersion of Agglomerated Nanoparticles by Fine Beads Mill Journal of the Society of Powder Technology, Japan, 41 (2004) 578-585.

[80] B. R. Munson, D. F. Young, T. H. Okiishi, Fundamentals of Fluid Mechanics (3rd Ed.) with Student Solutions Manual, John Wiley & Sons, Incorporated 1997.

[81] Y. Hwang, J.-K. Lee, J.-K. Lee, Y.-M. Jeong, S.-I. Cheong, Y.-C. Ahn, S. H. Kim, Production and dispersion stability of nanoparticles in nanofluids, Powder Technology, 186 (2008) 145-153.

[82] A. M. Davies Cn, Leacey D., Impingement of dust from air jets, Archives of Industrial Hygiene and Occupational Medicine, 4 (1951) 354-397.

[83] Y. Kousaka, K. Okuyama, A. Shimizu, T. Yoshida, Dispersion Mechanism of Aggregate Particles in Air, Journal of Chemical Engineering of Japan, 12 (1979) 152-159.

[84] A. S. H. Yamamoto, D. Kunii, Dispersion of airborne aggregates by high speed air stream, Kagaku Kogaku Ronbunshu, 6 (1980) 103-105.

[85] W. C. Hinds, Aerosol Technology: Properties, Behavior, and Measurement of Airborne Particles, Wiley 2012.

[86] Y. Yamada, S. Doi, M. Yasuguchi, Powder disperser, United States Patent and Trademark Office (USPTO), Nisshin Engineering Co Ltd, Nisshin Seifun Group Inc, 1983.

[87] K. Gotoh, M. Takahashi, H. Masuda, The Dispersion Mechanism of a Mixer-type Disperser, Journal of the Society of Powder Technology, Japan, 29 (1992) 11-17.

[88] P. Tang, D. F. Fletcher, H. K. Chan, J. A. Raper, Simple and cost-effective powder disperser for aerosol particle size measurement, Powder Technology, 187 (2008) 27-36.

[89] R. Rathbone, Fluidization Engineering (Second Edition), Gas Separation & Purification, 7 (1993) 63.

[90] C. Zhu, G. Liu, Q. Yu, R. Pfeffer, R. N. Dave, C. H. Nam, Sound assisted fluidization of nanoparticle agglomerates, Powder Technology, 141 (2004) 119-123.

[91] J. M. Valverde, M. J. Espin, M. a. S. Quintanilla, A. Castellanos, Electrofluidized bed of silica nanoparticles, Journal of Electrostatics, 67 (2009) 439-444.

[92] Q. Yu, R. N. Dave, C. Zhu, J. A. Quevedo, R. Pfeffer, Enhanced fluidization of nanoparticles in an oscillating magnetic field, AIChE Journal, 51 (2005) 1971-1979.

[93] J. Yang, T. Zhou, L. Song, Agglomerating vibro-fluidization behavior of nano-particles, Advanced Powder Technology, 20 (2009) 158-163.

[94] J. A. Quevedo, A. Omosebi, R. Pfeffer, Fluidization enhancement of agglomerates of metal oxide nanopowders by microjets, AIChE Journal, 56 (2010) 1456-1468.

[95] J. Fernández De La Mora, N. Rao, P. H. Mcmurry, Inertial impaction of fine particles at moderate reynolds numbers and in the transonic regime with a thin-plate orifice nozzle, Journal of Aerosol Science, 21 (1990) 889-909.

[96] S. Rennecke, A. P. Weber, A novel model for the determination of nanoparticle impact velocity in low pressure impactors, Journal of Aerosol Science, 55 (2013) 89-103.

[97] W. John, V. Sethi, Breakup of Latex Doublets by Impaction, Aerosol Science and Technology, 19 (1993) 57-68.

[98] M. Seipenbusch, A. Heel, A. P. Weber, G. Kasper, Determination of Coating Thickness of DEHS on Submicron Particles by Means of Low Pressure Impaction, Chemical Engineering & Technology, 25 (2002) 77.

[99] M. Ihalainen, T. Lind, T. Torvela, K. E. J. Lehtinen, J. Jokiniemi, A Method to Study Agglomerate Breakup and Bounce During Impaction, Aerosol Science and Technology, 46 (2012) 990-1001.

[100] S. Adi, H. Adi, H.-K. Chan, Z. Tong, R. Yang, A. Yu, Effects of mechanical impaction on aerosol performance of particles with different surface roughness, Powder Technology, 236 (2013) 164-170.

[101] M. Ihalainen, T. Lind, A. Arffman, T. Torvela, J. Jokiniemi, Break-Up and Bounce of TiO2Agglomerates by Impaction, Aerosol Science and Technology, 48 (2013) 31-41.

[102] J. W. Kwek, D. Heng, S. H. Lee, W. K. Ng, H. K. Chan, S. Adi, J. Heng, R. B. H. Tan, High speed imaging with electrostatic charge monitoring to track powder deagglomeration upon impact, Journal of Aerosol Science, 65 (2013) 77-87.

[103] X. Guo, M. Wagner, A. Gutsche, J. Meyer, M. Seipenbusch, H. Nirschl, Laboratory SWAXS combined with a low-pressure impactor for quasi-online analysis of nanoparticles generated by spark discharge, Journal of Aerosol Science, 85 (2015) 17-29.

[104] B. Kongsombut, A. Tsutsumi, N. Suankaew, T. Charinpanitkul, Encapsulation of SiO2and TiO2Fine Powders with Poly(dl-lactic-co-glycolic acid) by Rapid Expansion of Supercritical

CO2Incorporated with Ethanol Cosolvent, Industrial & Engineering Chemistry Research, 48 (2009) 11230-11235.

[105] B. Esmaeili, J. Chaouki, C. Dubois, Encapsulation of nanoparticles by polymerization compounding in a gas/solid fluidized bed reactor, AIChE Journal, 55 (2009) 2271-2278.

[106] M. Cao, Q. Liu, M. Chen, P. Yang, Y. Xu, H. Wu, J. Yu, L. He, X.-H. Zhang, Q. Zhang, Dispersing hydrophilic nanoparticles in nonaqueous solvents with superior long-term stability, RSC Advances, 7 (2017) 25535-25541.

[107] K. Meyer, I. Zimmermann, Effect of glidants in binary powder mixtures, Powder Technology, 139 (2004) 40-54.

[108] N. Y. K. Chew, H. K. Chan, Pharmaceutical Research, 18 (2001) 1570-1577.

[109] X. M. Zeng, G. P. Martin, S.-K. Tee, C. Marriott, The role of fine particle lactose on the dispersion and deaggregation of salbutamol sulphate in an air stream in vitro, International Journal of Pharmaceutics, 176 (1998) 99-110.

[110] S. T. Tedeschi, N. I. Stevens, K. Powers, A. Ranade, B. M. Moudgil, H. El-Shall, Improving Aerosol Dispersion through Processing and Dissemination Techniques, KONA Powder and Particle Journal, 27 (2009) 217-227.

[111] M. D. Louey, P. J. Stewart, Particle interactions involved in aerosol dispersion of ternary interactive mixtures, Pharmaceutical Research, 19 (2002) 1524-1531.

[112] H. Skaff, T. Emrick, Reversible addition fragmentation chain transfer (RAFT) polymerization from unprotected cadmium selenide nanoparticles, Angew Chem Int Ed Engl, 43 (2004) 5383-5386.

[113] U. Bilati, E. Allemann, E. Doelker, Development of a nanoprecipitation method intended for the entrapment of hydrophilic drugs into nanoparticles, Eur J Pharm Sci, 24 (2005) 67-75.

[114] T. Govender, PLGA nanoparticles prepared by nanoprecipitation: drug loading and release studies of a water soluble drug, Journal of Controlled Release, 57 (1999) 171-185.

[115] S. Laurent, D. Forge, M. Port, A. Roch, C. Robic, L. Vander Elst, R. N. Muller, Magnetic iron oxide nanoparticles: synthesis, stabilization, vectorization, physicochemical characterizations, and biological applications, Chemical Reviews, 108 (2008) 2064-2110.

[116] Y. Lu, Y. Yin, B. T. Mayers, Y. Xia, Modifying the Surface Properties of Superparamagnetic Iron Oxide Nanoparticles through A Sol−Gel Approach, Nano Letters, 2 (2002) 183-186.

[117] C. Liu, B. Zou, A. J. Rondinone, Z. J. Zhang, Sol-gel synthesis of free-standing ferroelectric lead zirconate titanate nanoparticles, Journal of the American Chemical Society, 123 (2001) 4344-4345.

[118] J. H. Bang, K. S. Suslick, Applications of ultrasound to the synthesis of nanostructured materials, Advanced Materials, 22 (2010) 1039-1059.

[119] L. Sun, J. Li, C. Wang, S. Li, Y. Lai, H. Chen, C. Lin, Ultrasound aided photochemical synthesis of Ag loaded TiO2 nanotube arrays to enhance photocatalytic activity, Journal of Hazardous materials, 171 (2009) 1045-1050.

[120] S. Santra, R. Tapec, N. Theodoropoulou, J. Dobson, A. Hebard, W. Tan, Synthesis and Characterization of Silica-Coated Iron Oxide Nanoparticles in Microemulsion: The Effect of Nonionic Surfactants, Langmuir, 17 (2001) 2900-2906.

[121] M. A. López-Quintela, Synthesis of nanomaterials in microemulsions: formation mechanisms and growth control, Current Opinion in Colloid & Interface Science, 8 (2003) 137-144.

[122] Z. S. Pillai, P. V. Kamat, What Factors Control the Size and Shape of Silver Nanoparticles in the Citrate Ion Reduction Method?, The Journal of Physical Chemistry B, 108 (2004) 945-951.

[123] Y. Lee, J. R. Choi, K. J. Lee, N. E. Stott, D. Kim, Large-scale synthesis of copper nanoparticles by chemically controlled reduction for applications of inkjet-printed electronics, Nanotechnology, 19 (2008) 415604.

[124] K. Sato, S. Kondo, M. Tsukada, T. Ishigaki, H. Kamiya, Influence of Solid Fraction on the Optimum Molecular Weight of Polymer Dispersants in Aqueous TiO2Nanoparticle Suspensions, Journal of the American Ceramic Society, 90 (2007) 3401-3406.

[125] L. Palmqvist, K. Holmberg, Dispersant adsorption and viscoelasticity of alumina suspensions measured by quartz crystal microbalance with dissipation monitoring and in situ dynamic rheology, Langmuir, 24 (2008) 9989-9996.

[126] F. Nsib, N. Ayed, Y. Chevalier, Dispersion of hematite suspensions with sodium polymethacrylate dispersants in alkaline medium, Colloids and Surfaces A: Physicochemical and Engineering Aspects, 286 (2006) 17-26.

[127] S. Marre, K. F. Jensen, Synthesis of micro and nanostructures in microfluidic systems, Chemical Society Reviews, 39 (2010) 1183-1202.

[128] A. Abou-Hassan, O. Sandre, V. Cabuil, Microfluidics in inorganic chemistry, Angewandte Chemie, International Edition in English, 49 (2010) 6268-6286.

[129] D. Wen, Y. Ding, Effective Thermal Conductivity of Aqueous Suspensions of Carbon Nanotubes (Carbon Nanotube Nanofluids), Journal of Thermophysics and Heat Transfer, 18 (2004) 481-485.

[130] B. Wang, W. Zhang, W. Zhang, C. Yu, G. Wang, L. Huang, A. S. Mujumdar, Influence of Drying Processes on Agglomeration and Grain Diameters of Magnesium Oxide Nanoparticles, Drying Technology, 25 (2007) 715-721.

[131] E. Teunou, D. Poncelet, Batch and continuous fluid bed coating – review and state of the art, Journal of Food Engineering, 53 (2002) 325-340.

[132] J. Flesch, D. Kerner, H. Riemenschneider, R. Reimert, Experiments and modeling on the deacidification of agglomerates of nanoparticles in a fluidized bed, Powder Technology, 183 (2008) 467-479.

[133] M. Voll, P. Kleinschmit, Carbon, 6. Carbon Black, Ullmann's encyclopedia of industrial chemistry, Wiley-VCH Verlag GmbH and Co. KGaA 2010.

[134] S. Habibzadeh, O. Zabeida, A. Argoitia, R. Sargent, J. Klemberg-Sapieha, J. Chaouki, L. Martinu, Conformal Multilayer Photocatalytic Thin Films on Fine Particles by Atmospheric Pressure Fluidized Bed Chemical Vapor Deposition, Industrial & Engineering Chemistry Research, 57 (2018) 10345-10353.

[135] J. R. V. Ommen;, E. Abadjieva;, Y. L. M. Creyghton, Plasma-enhanced chemical vapour deposition on particles in an atmospheric circulating fluidized bed, The 13th International Conference on Fluidization, 2010.

[136] J. L. P. Luis F. Hakim, Michelle D. Casper, Alan W. Weimer, Fluidization Behavior and Conformal Coating of Nanoparticles in Fluidized Beds by ALD, AIChE, (2004).

[137] J. C. Park, D. A. Gilbert, K. Liu, A. Y. Louie, Microwave enhanced silica encapsulation of magnetic nanoparticles, Journal of Materials Chemistry, 22 (2012) 8449.

[138] C. Vahlas, B. Caussat, P. Serp, G. N. Angelopoulos, Principles and applications of CVD powder technology, Materials Science and Engineering: R: Reports, 53 (2006) 1-72.

[139] Y. Wang, R. N. Dave, R. Pfeffer, Polymer coating/encapsulation of nanoparticles using a supercritical anti-solvent process, The Journal of Supercritical Fluids, 28 (2004) 85-99.

[140] J. Poostforooshan, S. Rennecke, M. Gensch, S. Beuermann, G.-P. Brunotte, G. Ziegmann, A. P. Weber, Aerosol Process for theIn SituCoating of Nanoparticles with a Polymer Shell, Aerosol Science and Technology, 48 (2014) 1111-1122.

[141] T. V. Pfeiffer, P. Kedia, M. E. Messing, M. Valvo, A. Schmidt-Ott, Precursor-Less Coating of Nanoparticles in the Gas Phase, Materials (Basel), 8 (2015) 1027-1042.

[142] J. Tavares, E. J. Swanson, S. Coulombe, Plasma Synthesis of Coated Metal Nanoparticles with Surface Properties Tailored for Dispersion, Plasma Processes and Polymers, 5 (2008) 759-769.

[143] J. Tavares, S. Coulombe, Dual plasma synthesis and characterization of a stable copper–ethylene glycol nanofluid, Powder Technology, 210 (2011) 132-142.

[144] A. Münzer, J. Sellmann, P. Fortugno, A. Kempf, C. Schulz, H. Wiggers, Inline coating of silicon nanoparticles in a plasma reactor: Reactor design, simulation and experiment, Materials Today: Proceedings, 4 (2017) S118-S127.

[145] B. Zhang, Y.-C. Liao, S. L. Girshick, J. T. Roberts, Growth of coatings on nanoparticles by photoinduced chemical vapor deposition, Journal of Nanoparticle Research, 10 (2007) 173-178.

[146] M. Horio, H. Kuroki, Three-dimensional flow visualization of dilutely dispersed solids in bubbling and circulating fluidized beds, Chemical Engineering Science, 49 (1994) 2413-2421.

[147] U. Lackermeier, C. Rudnick, J. Werther, A. Bredebusch, H. Burkhardt, Visualization of flow structures inside a circulating fluidized bed by means of laser sheet and image processing, Powder Technology, 114 (2001) 71-83.

[148] K. S. Lim, P. K. Agarwal, B. K. O'neill, Measurement and modelling of bubble parameters in a two-dimensional gas-fluidized bed using image analysis, Powder Technology, 60 (1990) 159-171.

[149] R. F. Mudde, H. B. M. Schulte, H. E. A. Van Den Akker, Analysis of a bubbling 2-D gas-fluidized bed using image processing, Powder Technology, 81 (1994) 149-159.

[150] J. R. Van Ommen, R. F. Mudde, Measuring the Gas-Solids Distribution in Fluidized Beds -- A Review, International Journal of Chemical Reactor Engineering, 6 (2008).

[151] J. Werther, B. Hage, C. Rudnick, A comparison of laser Doppler and single-fibre reflection probes for the measurement of the velocity of solids in a gas-solid circulating fluidized bed, Chemical Engineering and Processing: Process Intensification, 35 (1996) 381-391.

[152] B. Esmaeili, J. Chaouki, C. Dubois, An evaluation of the solid hold-up distribution in a fluidized bed of nanoparticles using radioactive densitometry and fibre optics, The Canadian Journal of Chemical Engineering, 86 (2008) 543-552.

[153] D. M. K. J. Ruud Van Ommen, Alan Weimer, Robert Pfeffer, Berend Van Wachem, Experiments and modelling of micro-jet assisted fluidization of nanoparticles, (2010).

[154] Y. Ding, B. Stahlmecke, H. Kaminski, Y. Jiang, T. a. J. Kuhlbusch, M. Riediker, Deagglomeration testing of airborne nanoparticle agglomerates: Stability analysis under varied aerodynamic shear and relative humidity conditions, Aerosol Science and Technology, 50 (2016) 1253-1263.

[155] C. T. Crowe, Review—Numerical Models for Dilute Gas-Particle Flows, Journal of Fluids Engineering, 104 (1982) 297-303.

[156] E. Akgün, J. Hubbuch, M. Wörner, Perspectives of aerosol-photopolymerization: Nanoscale polymer particles, Chemical Engineering Science, 101 (2013) 248-252.

[157] E. Akgün, J. Hubbuch, M. Wörner, Perspectives of aerosol-photopolymerization: organic-inorganic hybrid nanoparticles, Colloid and Polymer Science, 292 (2014) 1241-1247.

[158] K. L. Dreher, Health and Environmental Impact of Nanotechnology: Toxicological Assessment of Manufactured Nanoparticles, Toxicological Sciences, 77 (2003) 3-5.

[159] R. Gupta, H. Xie, Nanoparticles in Daily Life: Applications, Toxicity and Regulations, J Environ Pathol Toxicol Oncol, 37 (2018) 209-230.

[160] G. H. Amoabediny, A. Naderi, J. Malakootikhah, M. K. Koohi, S. A. Mortazavi, M. Naderi, H. Rashedi, Guidelines for safe handling, use and disposal of nanoparticles, Journal of Physics: Conference Series, 170 (2009) 012037.

[161] M. Auffan, J. Rose, J. Y. Bottero, G. V. Lowry, J. P. Jolivet, M. R. Wiesner, Towards a definition of inorganic nanoparticles from an environmental, health and safety perspective, Nat Nanotechnol, 4 (2009) 634-641.

APPENDIX A   TWO-PHASE SIMULATION: MESH AND PARTICLE STUDY

In order to minimize the influence of mesh size and injected particle samples on the final results of a simulation, mesh study and particle study is required to be done. As such, in the first part the effect of mesh refinement around the jet zone was studied (Figure A-1). For this purpose, a box with 1.5 cm height and 0.5 cm width was selected around the jet zone and the primary defined triangular mesh was locally refined in this box up to level 3. The statistics of the mesh is tabulated in Table A-1. The jet velocity profiles with different mesh sizes were calculated and compared to each other. Comparing profiles shows although refining the mesh size near the jet zone change the jet velocity profile, mesh sizes less than 20 micron no longer affect the velocity profile, while dramatically increasing the calculation time. Therefore, this size and configuration of the mesh was considered for the rest of simulation.

Table A-1 Statistics of the mesh

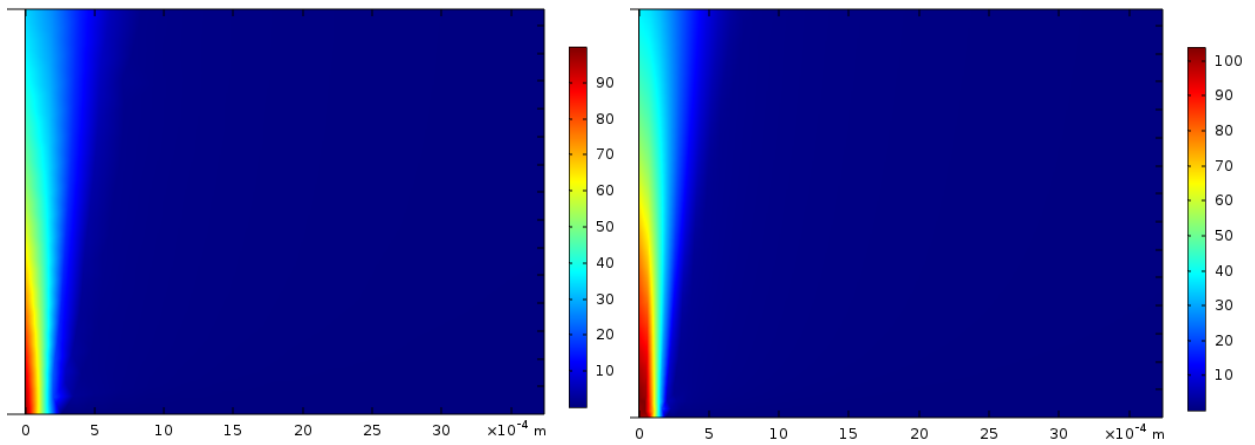| Mesh #	No. of elements	Minimum element size (μm)
Mesh 1 (Physics-controlled)	43,158	120
Mesh 2 (refine 1)	335,036	60
Mesh 3 (refine 2)	423,958	30
Mesh 4 (refine 3)	886,037	15
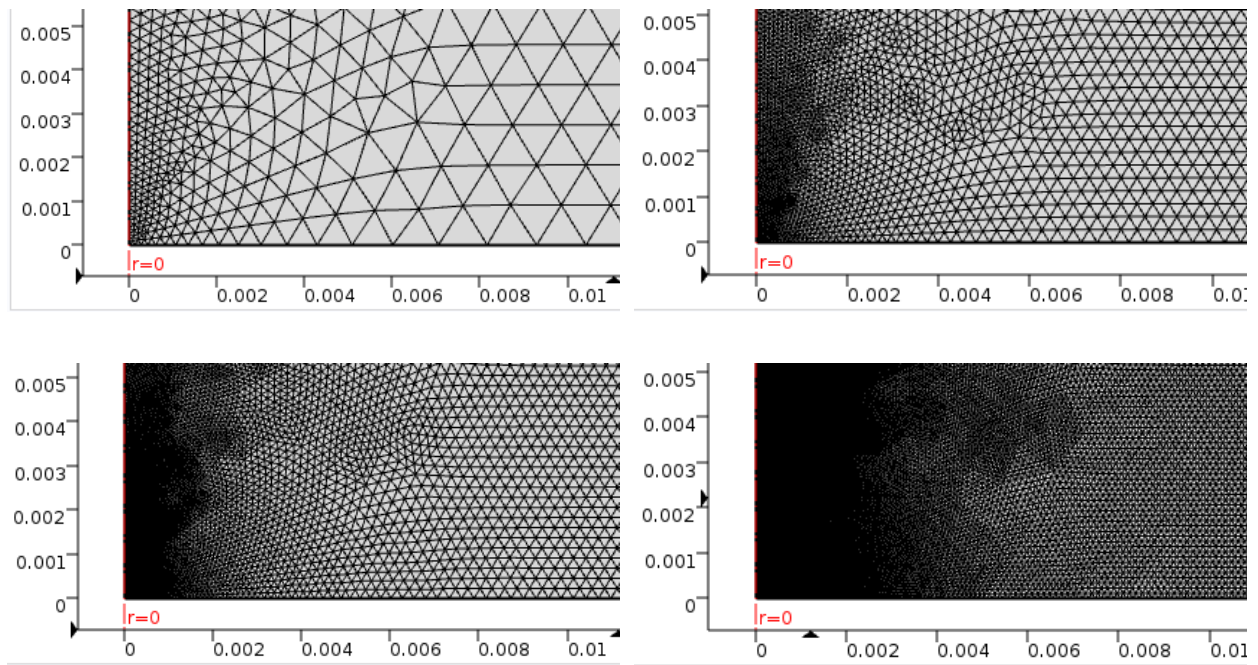
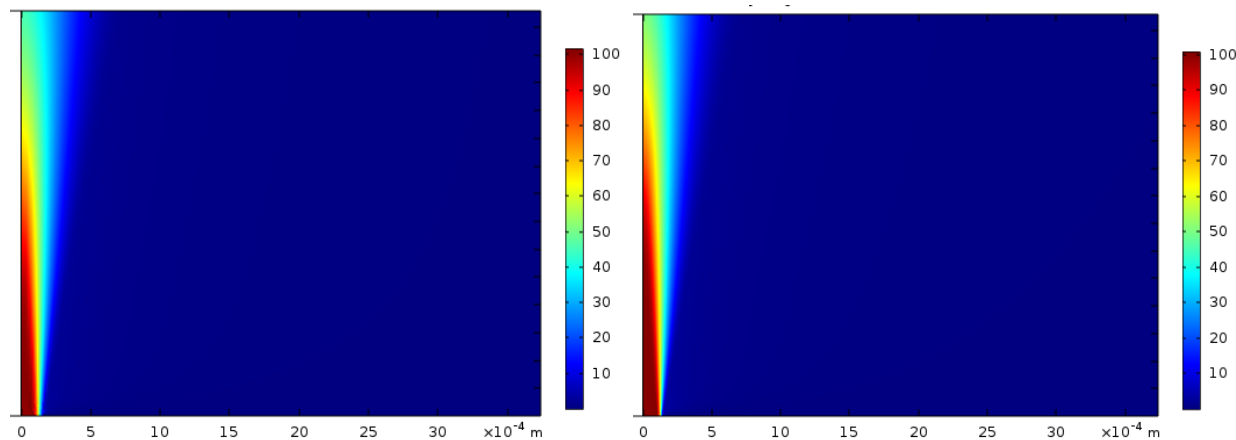Figure A-2 Locally refining mesh size using COMSOL Multiphysics software 4.4

Figure A-3 2D velocity profile of the jet (a-d) corresponding with mesh size of Figure A-2 (a-d) (jet velocity of 100 m/s)

After studying the mesh size in COMSOL Multiphysics 4.4, the single-phase simulation result was taken to Fluent 6.3 for studying the particle trajectory. Before studying the gas phase velocity profile along the jet axis was compared (Figure A-4). Both profile follow an exact same trend.
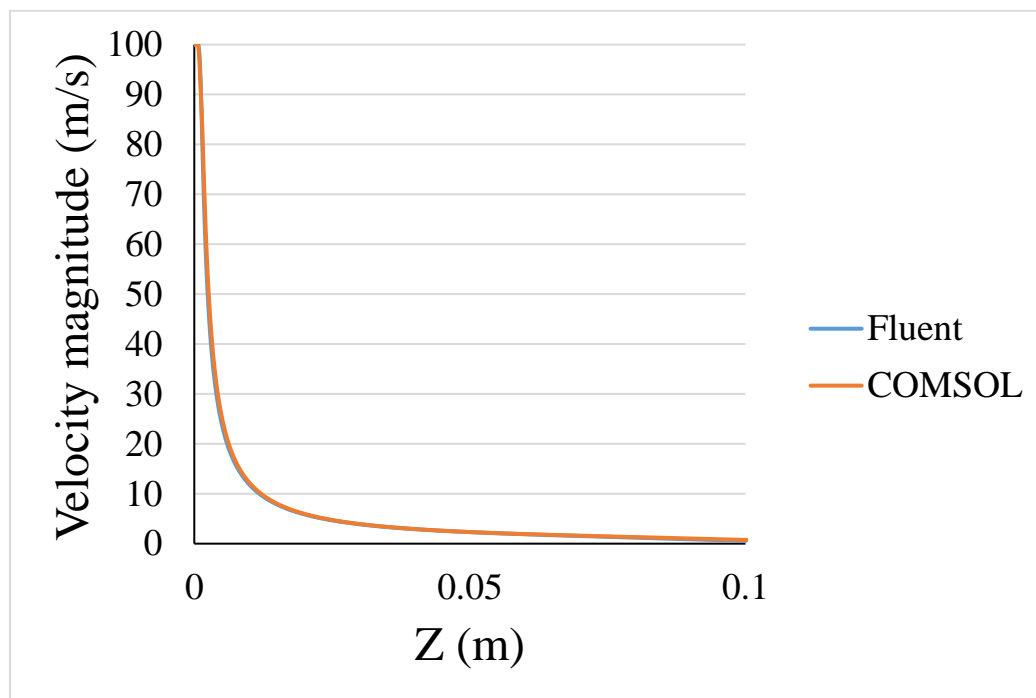

Figure A-4 Comparing gas phase profiles along the jet axis obtained from COMOSL and Fluent simulations

After establishing the gas phase matrix, a set of simulation was run for the purpose of particle study, considering the position and size of injected particulate samples. To do so, the following parameters were selected according to the radius of fluidized bed column (2.5 cm) and average size of fluidized agglomerates (70 µm).

Table A-2 Parameters selected for the particle study

Particle release position (cm)	Particle size (µm)
0.025 (1 R)	0.7
0.0025 (0.1 R)	7
0.00025 (0.01 R)	70
	700

Figure A-5 depicts two particle sizes of 7 and 70 µm with population of 1000 and their trajectories when are injected through a line width of 0.0025 cm close to the tip of the jet. Results shows particle is the order of 7 µm can easily captured by the jet and eventually entrained out f the bed, while particles as large as 70 µm even though those were engaged in the jet stream, eventually fall back to the bed when gravity force is dominated to the hydrodynamic forces.
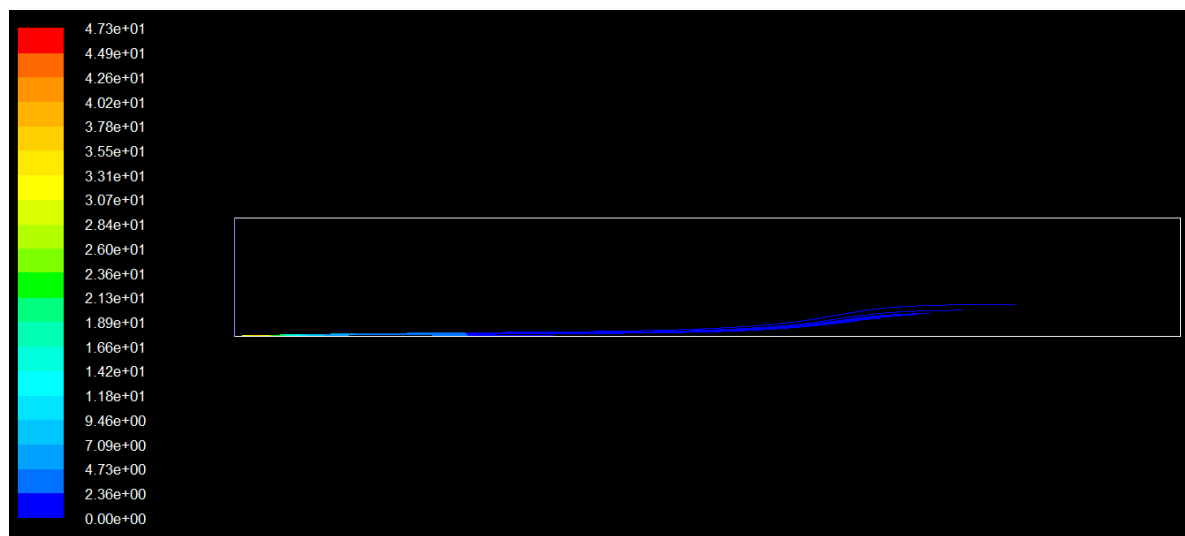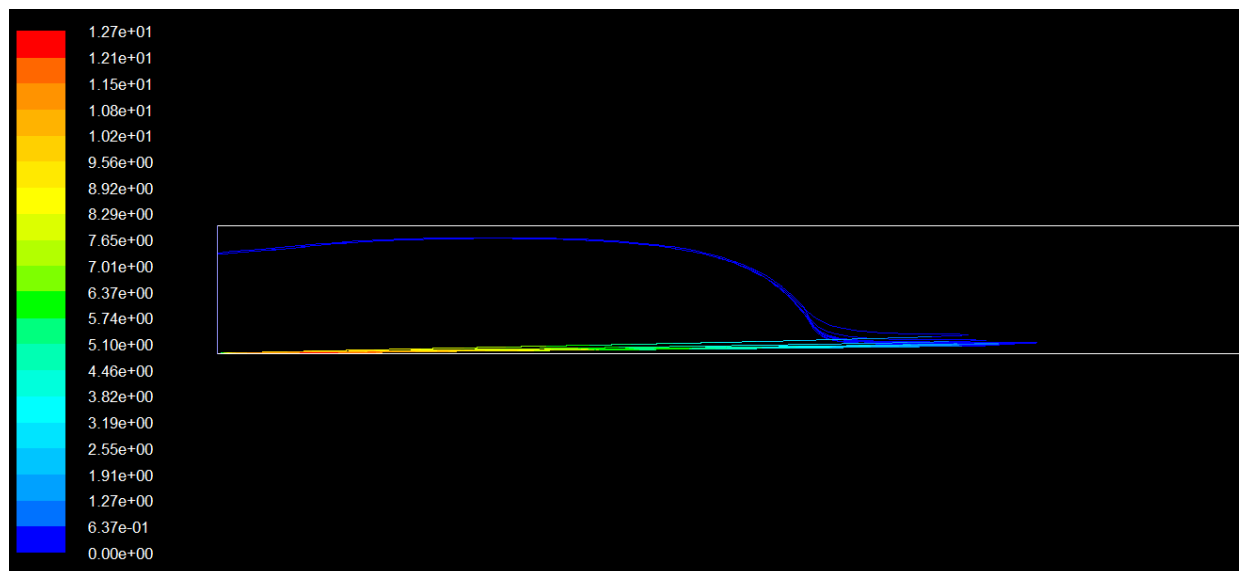
Figure A-5 particle trajectories for 7 µm (top) and 70 µm (bottom) injectected at 0.01R
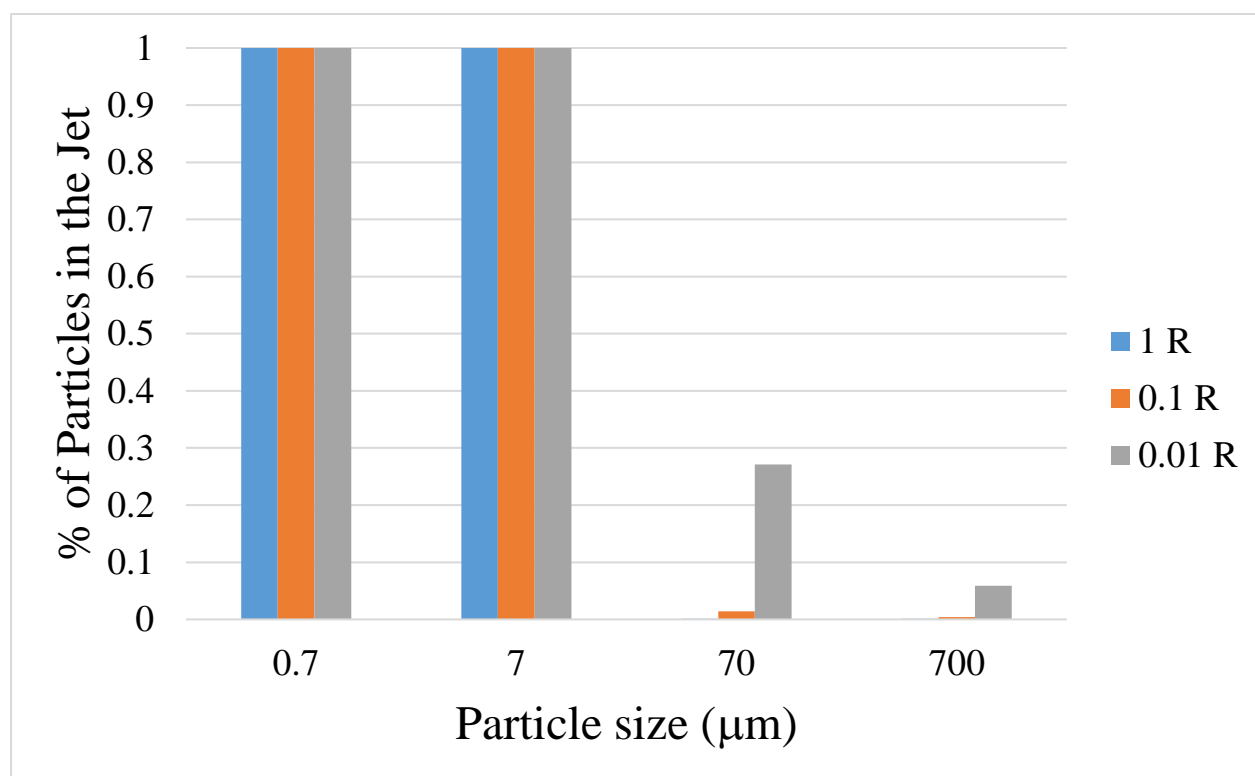

Figure A-6 Percentages of the particle population that were engaged with the jet due to the cavity effect (injected particle population in each sample was 1000).

Figure A-6, again corroborates particles smaller than 7 μm can be engaged even when the particle injection line expands to the width of the column, indicating jet cavity effect is able to capture the particles at far distance as 2.5 cm close to the wall and bring them to the jet stream. The numbers will reduce for particle size of 70 μm and finally particle with diameter of 700 μm are too large to be captured by the jet even when the injection line width was as small as 0.00025 cm near the jet.

The particle velocity distribution (average marked as square) and distance from the tip of the jet where the maximum velocity occurs (average marked as square) was shown in Figure A-7.
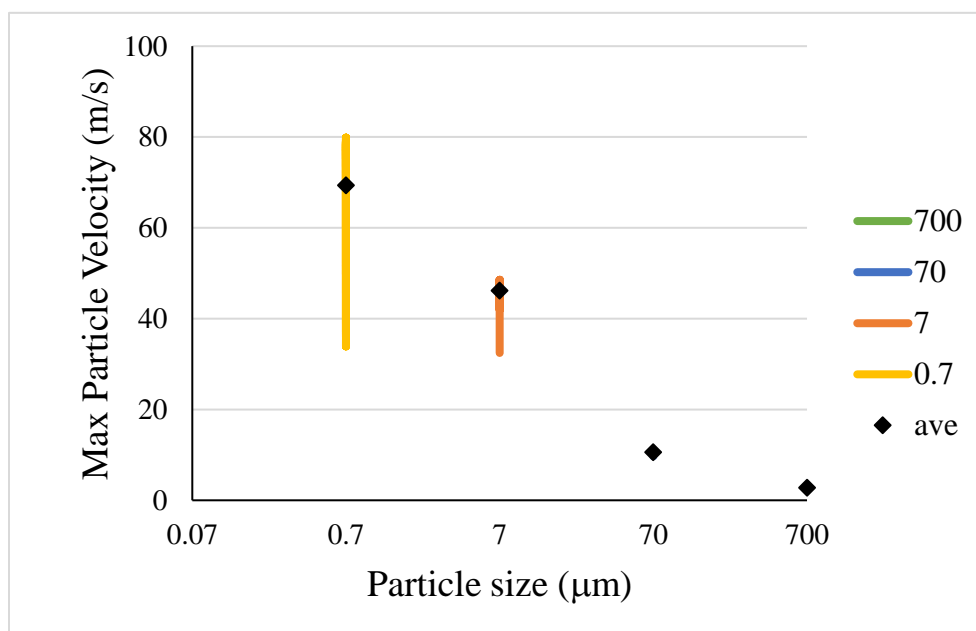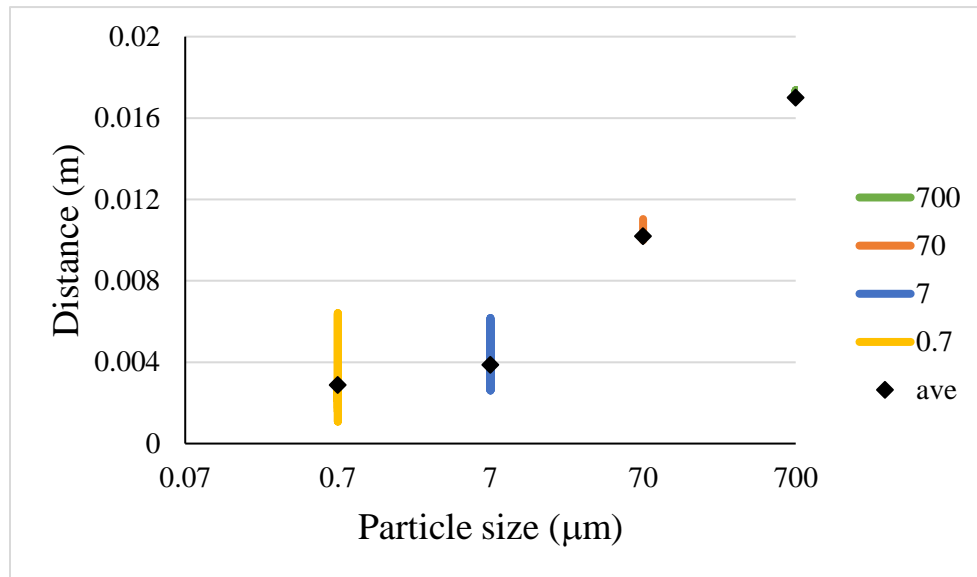
Figure A-7 maximum velocity distribution and the distances distribution at which maximum volocity occurs for particle sizes of different order of magnitude (average of the distribution was marked with black diamonds)

Finally the one-way and two-way coupling of particles were compared to each other (Figure A-8). The trajectory of particles showed a significant change; however, the maximum values and velocity profiles of particles did not change.
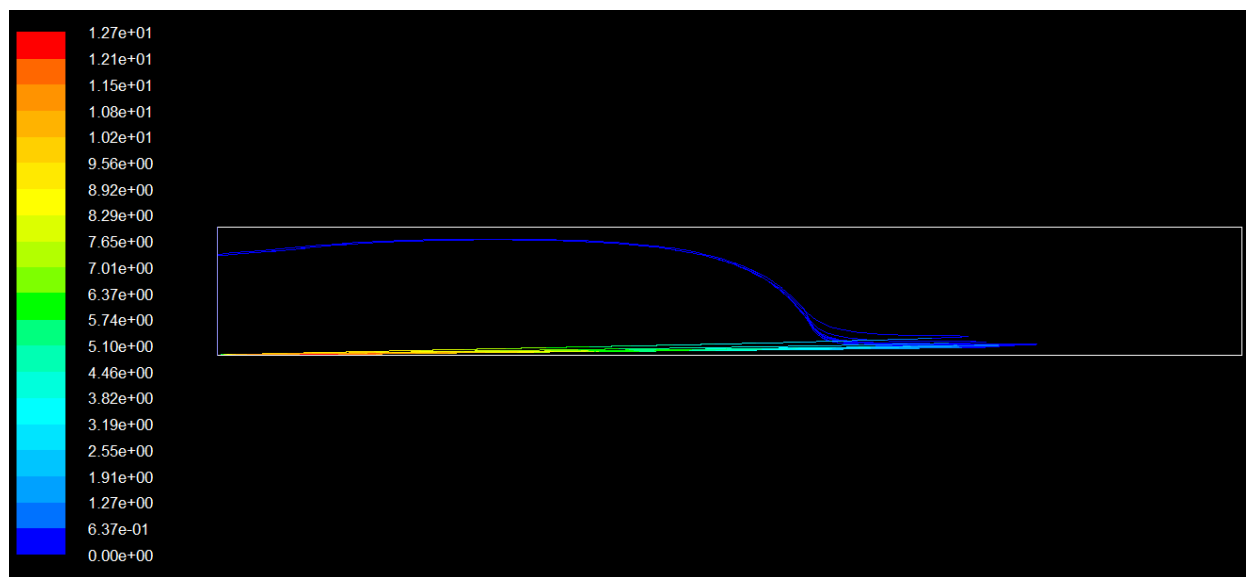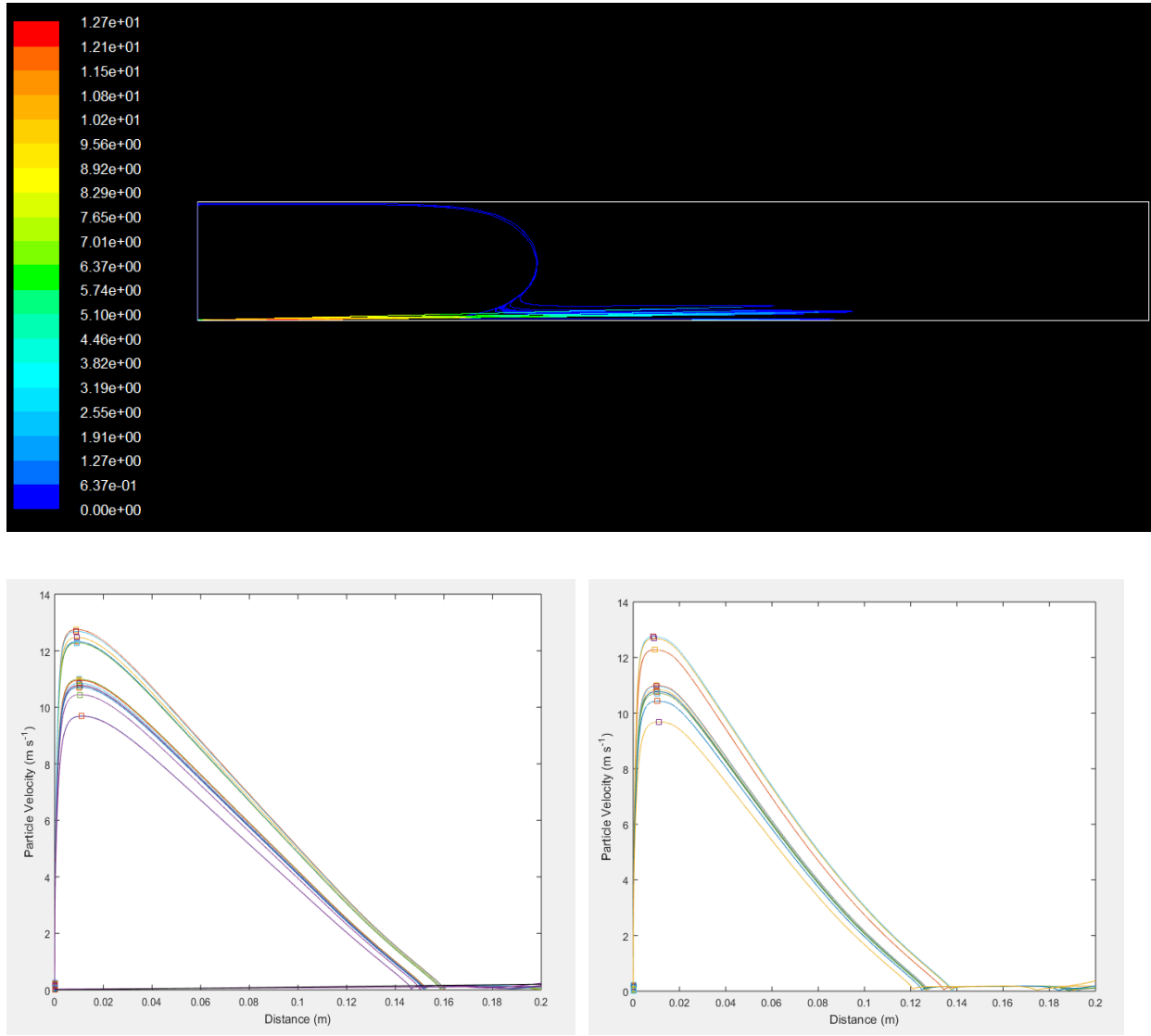
Figure A-8 Comparing particle trajectories and particle velocity profile of 1000 particles with the size of 70 μm injected from an injection line width of 0.01 R in one-way and two-way coupling simulation.

According to the final result, since the one-way and two-way coupling results were the same in terms of the maximum velocity values, the one-way simulation was selected for the purpose of particle velocity profiles since it requires much less time than two-way coupling simulation.

APPENDIX B   SAFETY OF NANOPARTICLES

Producing smaller stable NPs will require more attention to the safety and handling of those due to their higher biological or chemical activity. Engineered nanoparticles can be more toxic than larger agglomerated particles because they can diffuse through skin, be inhaled or ingested easier and move more freely than bulkier molecules. Although humans have been exposed to airborne NPs over many years, the growing use of engineered NPs is becoming another source of pollution. Several researchers show that nanoparticles generally are more toxic when introduced into the human body than larger particles of the same materials [158-160]. On the other side, there are some works that limits the adverse interaction of NPs within the human body to very small sizes. For example, Auffan et al. [161] demonstrated, according to their literature study, NPs larger than 30 nm (30–100 nm) show merely the same behavior as bulk materials, while smaller NPs than that show different interactions, as a result of having unique properties, that require specific attentions. This demand developing new protocols in handling and potential hazards of NPs.